Computational models for research in Medicine and Desalination

by

Andrew Philip Freiburger
A.S., Grand Rapids Community College, 2016
B.S., Grand Valley State University, 2019

A Thesis Submitted in Partial Fulfillment of the
Requirements for the Degree of

MASTER OF APPLIED SCIENCE

in the Department of Civil Engineering

Computational models for research in Medicine and Desalination

by

Andrew Philip Freiburger
A.S., Grand Rapids Community College, 2016
B.S., Grand Valley State University, 2019

Supervisory Committee

Dr. Heather L. Buckley, Supervisor
(Department of Civil Engineering)

Dr. Irina Paci, Outside Member
(Department of Chemistry)

ABSTRACT

The development of sustainable and practical technologies is essential for the continuation of civilization. Two problems that are particularly imperative for society to resolve are 1) water insecurity and 2) antimicrobial resistance. Water insecurity may be alleviated with desalination technologies, however, desalination is prone to a membrane fouling that hinders its practicality for low-resource contexts. The two primary types of membrane fouling are scaling – mineral precipitation and deposition upon the membrane – and biofouling – microbial colonization of the polymeric filtration membrane. The treatment of biofouling with antibiotics is intertwined with the antimicrobial resistance (AMR) crisis, where AMR infections are projected to exceed cancer in annual deaths by the mid-21st century. The AMR crisis may be mitigated through photodynamic inactivation (PDI), which uses reactive oxygen species (ROSs) to non-selectively oxidize and kill pathogens sufficiently fast to avoid adaptive mechanisms that result in AMR. The innumerable possible combinations of control and experimental variables in studies of membrane fouling and PDI are unlikely to be completely explored experimentally, where resource limitations restrain experimentation. This Thesis, therefore, developed models and Python application programming interfaces (APIs) that can 1) explore continuums of parameter values and 2) predict the efficacy of desalination or PDI systems. These open-source Python modules may expedite the development of practical technologies that resolve water insecurity and stymie antibiotic resistant epidemics, thereby improving the likelihood of a long-lived civilization far into the future.

Contents

List of Tables

List of Figures

ACKNOWLEDGEMENTS

I am grateful to:

My family for providing conversation, advise, and a weekly supply of organic *Brassica* that kept me focused during my research.

Ethan Sean Chan for being my partner in crime and for patiently teaching computer science to a curious chemist.

Heather L. Buckley for the opportunities, freedom, and guidance that enriched my research; and for the funding that made it all possible.

WISDOM

All models are wrong; some models are useful.

George E. Box

It is not the strongest nor the most intelligent of the species that survives.
It is the one that is most adaptable to change.

Charles Darwin

The credit belongs to the man who is actually in the arena, whose face is marred by dust and sweat and blood; who strives valiantly; who errs, who comes short again and again, because there is no effort without error and shortcoming; but who does actually strive to do the deeds; who knows great enthusiasms, the great devotions; who spends himself in a worthy cause; who at the best knows in the end the triumph of high achievement, and who at the worst, if he fails, at least fails while daring greatly, so that his place shall never be with those cold and timid souls who neither know victory nor defeat.

Theodore Roosevelt

Chapter 1

Introduction

1.1 Motivation

This Thesis sought to develop practical tools that can cultivate a sustainable society. The two specific problems that are addressed herein are 1) water insecurity and 2) antimicrobial resistance (AMR), which converge in desalination technologies. The research of this Thesis produced application programming interfaces (APIs) as computational tools that can facilitate technological development towards resolving these growing problems in society.

1.2 Water security

Fresh water resources are diminishing [1, 2], despite that water is one of the most abundant chemicals on Earth [3]. This is a consequence of global warming [4, 5] and climate change [6] that disrupt the water cycle, and pollution [7, 8, 9] and over-consumption [10, 11] that contaminate and deplete water reserves, respectively. One of the many consequences of less available freshwater is that billions of people [12], who disproportionately reside in developing nations, experience water insecurity each year [13]. This disparity in access to potable water is recognized as a top global priority in the 6th UN Sustainable Development Goal [14].

Desalination is a promising technology that may resolve water insecurities. Desalination enables municipalities to generate potable freshwater from diverse feed sources, especially oceans [15, 16] that are both within $100km$ for $\approx \frac{1}{2}$ of the human population [17] and are practically inexhaustible relative to the magnitude of human consumption. The most common desalination method is the spiral-wound reverse osmosis (RO) design, since it optimizes the filtration surface area per unit volume. A cross-sectional schema of RO is represented in Figure 1.1. These membranes, when operational, selectively permit the diffusion of water across the membrane while impurities are retained in the feed channel. The accumulation of ionic, chemical, and microbial impurities in the feed channel during desalination compromises filtration via membrane fouling [18], of which scaling – mineral precipitation and deposition

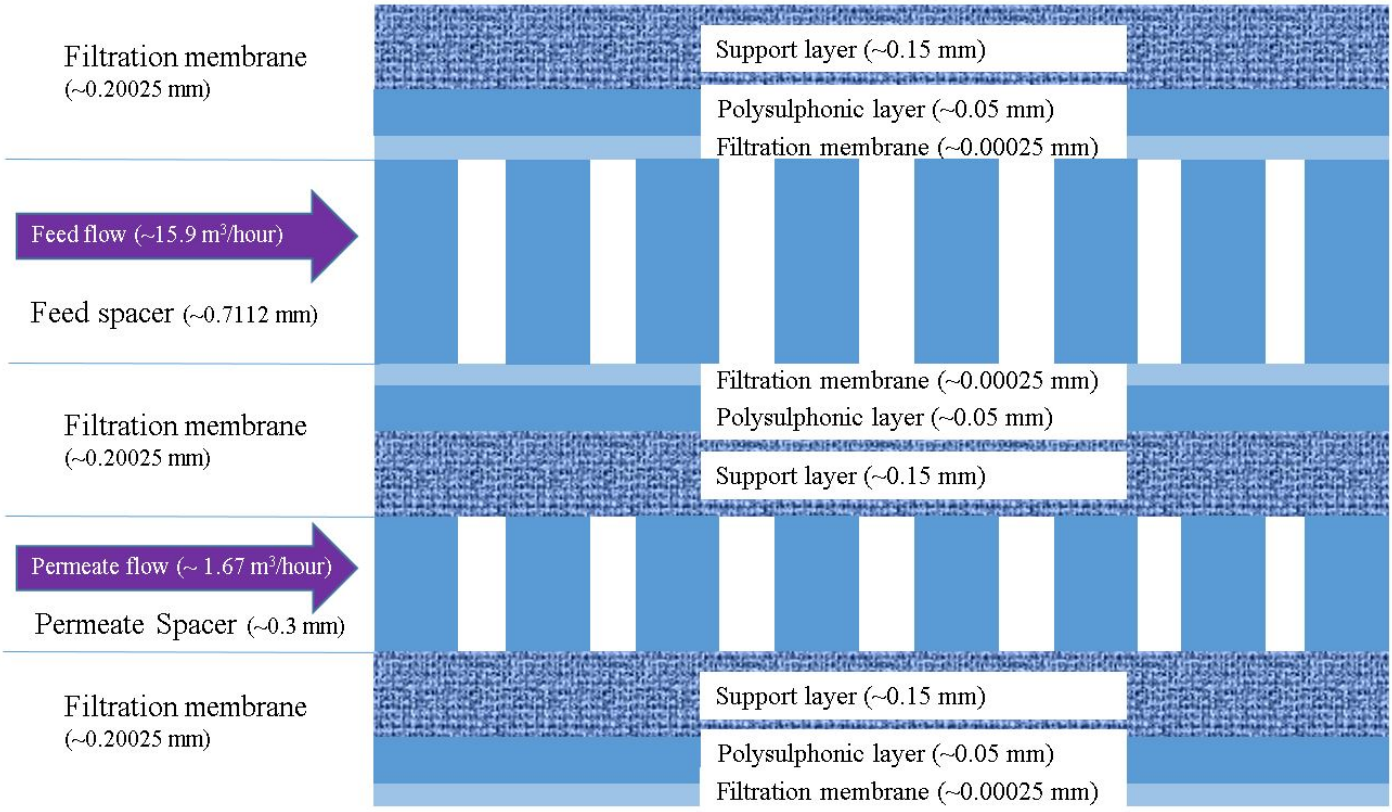

Figure 1.1: A cross-section of the RO polyamide filtration membrane [35]. The quantitative specifications are representative of the default values for our RO model, which are primarily based upon the DOW FILMTEC BW30-400 module.

upon the membrane surface [19, 20, 21, 22] – and biofouling [23, 24, 25, 26, 27, 28, 29, 30, 31, 32] – microbial colonization of the polymeric filtration membrane [33, 34] – are the primary types.

1.2.1 Scaling

Scaling in Figure 1.2 is a geochemical phenomena that can occlude and tear the filtration membrane. The geochemical equilibria that result in scaling are difficult to experimentally study; hence, computational software that predict scaling have been developed [35]. These software, however, are expensive and/or not accessible via an API, which limits its accessibility and its ability to guide investigators through experimental design. We therefore developed a one-dimensional reactive transport model of desalination, which is sufficiently simple to be numerically encoded in PHREEQC. This PHREEQC expression of our model is the basis of our software, ROSSpy (Reverse Osmosis Scaling Software in Python), which is an intuitive and open-source API that meets identified needs of the RO community to predict brine and scaling from desalination systems. This project is detailed with validation and use cases in Chapter 2.

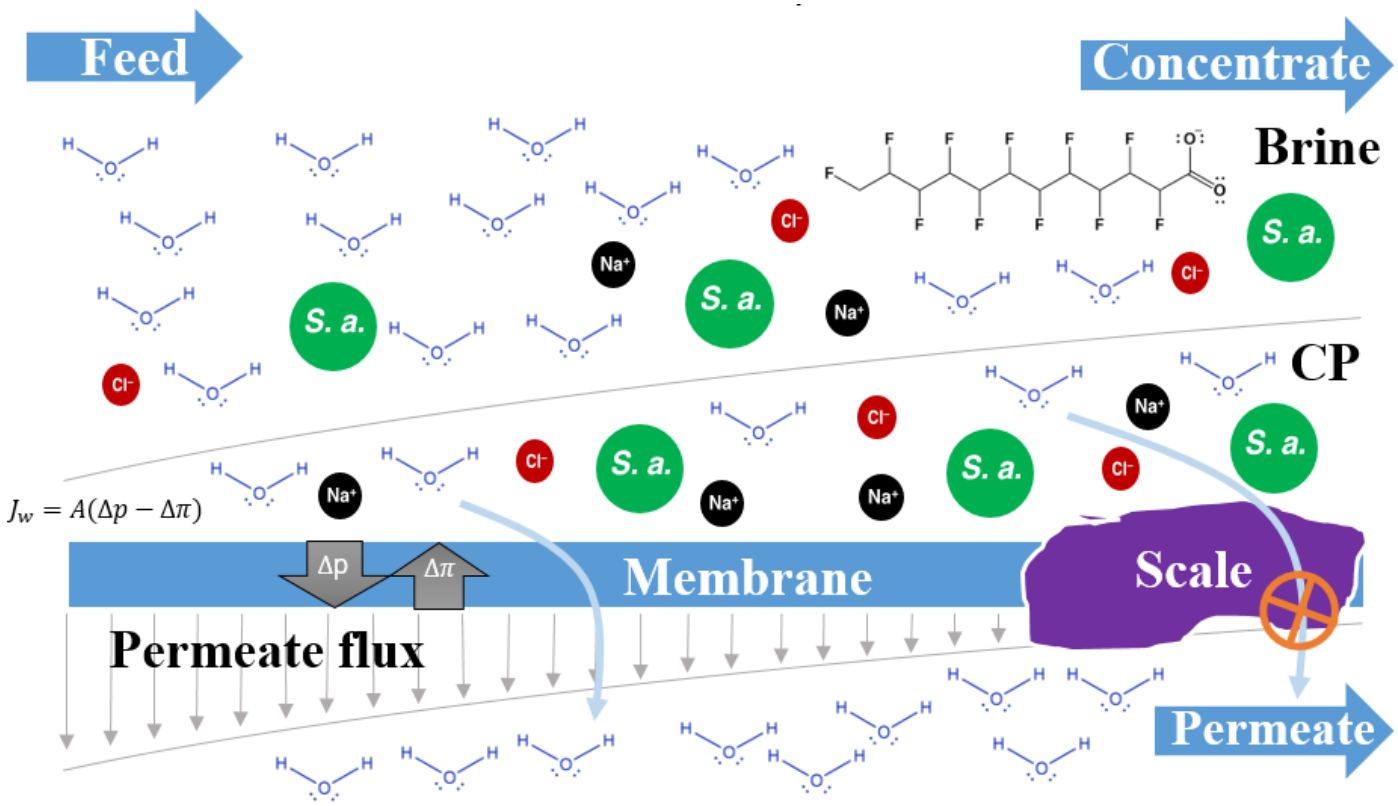

Figure 1.2: A cross-section of RO desalination, which depicts the geochemical environment and the physical hindrance of scaling upon the membrane surface. Membrane flux decreases over the module distance as a function of the pressure difference between the applied pressure of the feed and the osmotic pressure between the filtered (permeate) water and brine (concentrate) solution.

1.2.2 Biofouling

Biofouling is a microbial phenomena, where a surface is colonized and eventually biodegraded. Biocidal treatments can limit biofouling [36], however, these treatments have substantial collateral effects of chemically degrading the filtration membrane [37] and possibly exhibiting off-target effects in the environment [38, 39]. The design of benign anti-biofoulants [40] is therefore essential to improve the efficacy and sustainability of RO desalination. Innovation here [41] can be accelerated by computational tools that allow investigators to predict the effect of different chemical agents and biofilm conditions. We therefore developed the WCMpy (Whole Cell Model in Python) suite of packages to foster the development of such computational tools, which is detailed in Chapter 3.

1.3 Antimicrobial resistance

The treatment of RO biofouling with antibiotics is intertwined with the AMR crisis, where AMR infections are projected to exceed cancer in annual deaths, and globally cost 10^{13} USD in lost economic production, by the mid-21^{st} century [42]. The AMR crisis may be mitigated through the use of reactive oxygen species (ROSs), which non-selectively oxidize and kill pathogens while avoiding the mechanisms that result in AMR. ROSs, primarily singlet oxygen ($^1\Delta_g$), can be wielded on demand through photodynamic inactivation (PDI) by simply exposing a photosensitizer (PS) catalyst to incident light of the porper wavelength, which is illustrated in Figure 1.3. The innumerable possible combinations of PSs and undesirable microbial targets are unlikely to be completely explored with experiments before mid-century, since resource limitations restrain experimentation. We therefore developed the PDIpy module (Photodynamic Inactivation in Python) to rapidly predict PDI efficacy over a continuum of variable values, which can elucidate effective systems within the space of possible PDI technologies. This project is detailed in Chapter 4.

1.4 Thesis work

All of the figures and tables in this Thesis are original. The Python modules that have been published in the PyPI (Python Package Index) repository, at least partially for the completion of this Thesis, are listed in Table 1.1 with their respective quantity of PyPI downloads.

1.5 Future

The future aspirations for these projects are detailed in Chapter 5. The most notable far-term aspirations include the following: (1) amalgamate the WCMpy suite into a single module that simulates the biochemical effects of an anti-biofilm treatment; and (2) couple the mature module from (1) with the brine predictions from ROSSpy to comprehensively represent the effects of scaling and biofouling, and

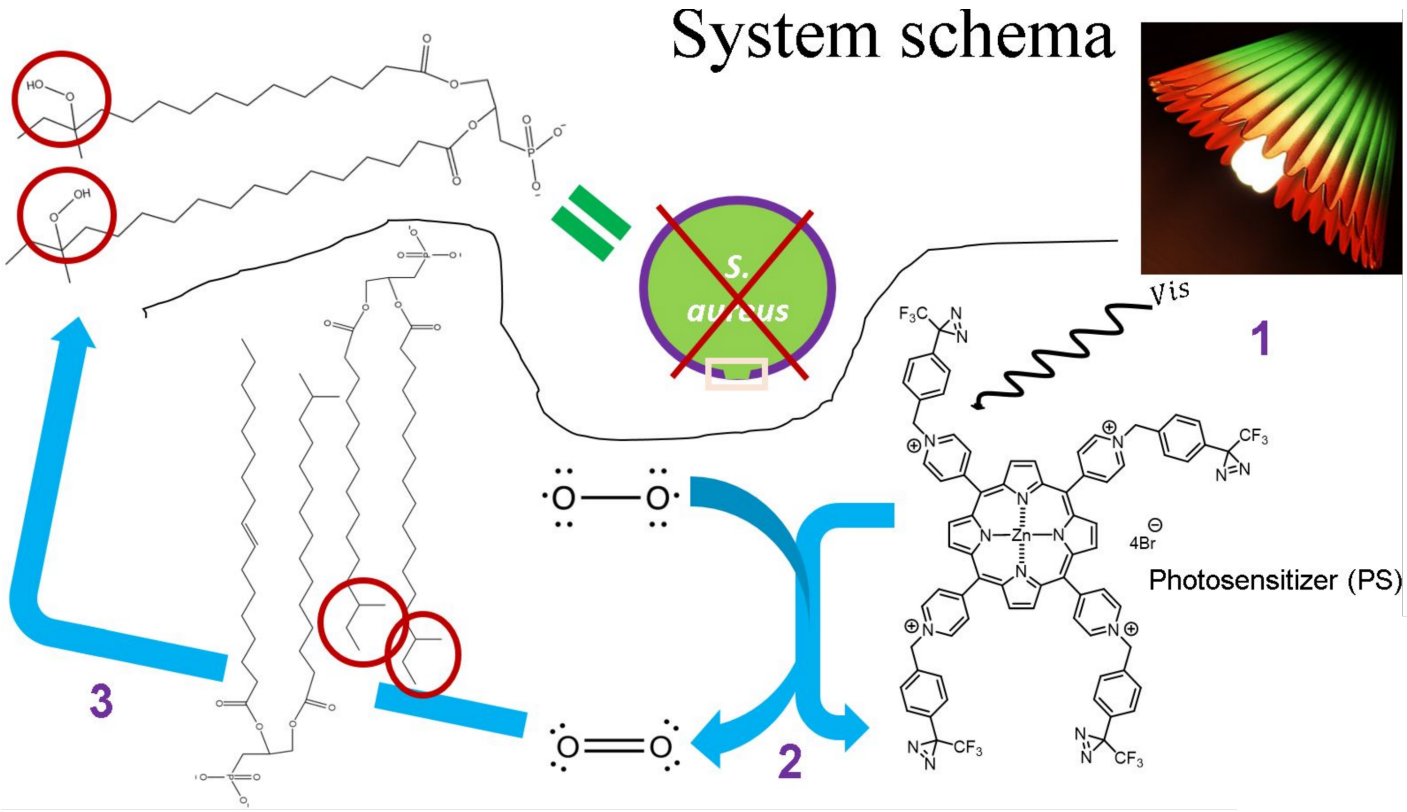

Figure 1.3: A conceptualization of the PDI process: 1) incident light first strikes and excites a PS; 2) the excited PS catalyzes the generation of $^1O_2$ from a ground-state oxygen; and 3) the $^3O_2$ oxidizes a biological target to the point of cellular death.

Project	**Module**	**PyPI downloads**	**Total**
ROSSpy	ROSSpy	10,013	21,956
	ChemW	11,943	
WCMpy	Codons	4,316	5,662
	BiGG_SABIO	511	
	dFBApy	835	
PDIpy	PDIpy	2,013	2,013
Total			**29,631**

Table 1.1: The cumulative PyPI downloads according to PePy (`https://pepy.tech/`) – per March 23th, 2022 – for each of the modules and projects of this Thesis. The GitHub repositories for each module are hyperlinked with the respective module name.

their interdependence [43, 44], from RO desalination. This may include the assessment of halophilic bacteria [45] that could thrive in RO brine.

Chapter 2

A one-dimensional model of scaling in Reverse Osmosis: ROSSpy

2.1 Introduction

Desalination technologies, most notably reverse osmosis (RO) [46], are imperative for meeting the 6th UN Sustainable Development Goal [14] of universalizing potable freshwater. Arid Middle-Eastern countries, who are both relatively affluent and geographically prone to water scarcity, are embracing RO desalination to satisfy domestic water needs; Israel, for example, supplies $\frac{3}{4}$ of its domestic water from desalination [47] and Saudi Arabia is responsible for $\approx 22\%$ of global water desalination [48]. RO is the most economical desalination technology [49, 50], however, it remains insufficiently efficient and economical for the low-resource communities. RO efficiency can be improved [51, 52] a) with energy recovery devices [17], that allow RO to approach the thermodynamic limit of desalinating seawater [53], and b) by mitigating membrane fouling such as scaling [19, 20, 21, 22], where minerals deposit upon the membrane surface and decrease membrane permeability such that greater applied pressures and energy usage are required to maintain a permeate flux over time. Scaling occurs mechanistically either through homogeneous precipitation from the highly concentrated brine byproduct of RO [54, 55] – which is itself hazardous [56, 57, 58, 59] but can be processed into useful salts [60, 61] in zero-liquid waste management systems [62, 63] or used in mixing-entropy batteries [64] – or through heterogeneous deposition upon nucleation sites on the membrane surface [65, 66]. The heterogeneous mechanism specifically occurs in a hyper-concentrated layer adjacent to the membrane called the concentration polarization (CP) [67, 68, 69, 70, 71, 72], which is achieved as a consequence of the no-slip boundary condition – analogous to the capillary effect – that prevents the CP from mixing with the bulk solution since the velocity gradient of the fluid reaches zero adjacent to the stationary filtration membrane [73].

Scaling, unfortunately, is experimentally elusive [74, 75, 76]. Computational programs [77, 78] may supplement experimental procedures [79, 80] as a means to investigate scaling and optimize RO efficiency; however, current programs are either unspecific to RO [81] or focus upon other aspects of RO: e.g. plant

operation [82, 83, 84, 85], permeate flux [86, 87], brine geochemistry [88], or fluid dynamics of the CP [89]. Mathematical programs [43, 90] and some with a user interface [91, 35] have been developed that simulate RO scaling, however, these lack an application programming interfaces (APIs), which is essential for the broad analyses, over a continuum of variables, that could accelerate geochemical scaling research.

We therefore developed a unique one-dimensional model that captures both the geochemistry of scaling equilibria and the reactive transport of desalination, in contrast to existing one-dimensional RO models that utilize the steady-state approximation and the solution-diffusion model [35]. This one-dimensional RO model – similar only to the WaterTap model [92] – is critically amenable with PHREEQC [93, 94], which provides a rigorous and open-source numerical implementation of our model, similar to previous studies of scaling [95, 66] and RO [96, 97, 98, 99]. We exemplify our model through replicating experimental literature and conducting numerous sensitivity analyses across continuums of parameter values. We further developed the only, to our knowledge, open-source API of RO reactive transport (ROSSpy: RO Scaling Software in Python) based upon our model, which fulfills identified needs of a scaling software for RO research [100], where users can create, execute, process, visualize, and export simulations with predicted scale mass per membrane filtration area ($\frac{g\ scale}{filtration\ m^2}$) and ionic brine concentrations. Developers are encouraged to contribute to ROSSpy, which we believe is an important stride towards satisfying research needs in scaling and ultimately reducing water insecurity, especially in low-resource contexts.

2.2 Methods

2.2.1 Conceptual

Our model represents RO desalination as a one-dimensional reactive transport process along the membrane-solution interface. The feed is represented by the single-domain model in Figure S4, where the bulk and CP solutions are aggregated into a single solution, as opposed to the more resolved dual-domain model, where the bulk and CP solutions are distinguished (Figure S5) [101, 102, 103, 104]. The dual-domain remains elusive within the confines of PHREEQC code (Section 6 of the Supporting Information) and moreover we demonstrate that the single-domain model is sufficient to recapitulate experimental results. Our model represents feed at the RO inlet with the Dirichlet boundary condition [105, 106] – a mathematical description of constant conditions at a model boundary – where the influent feed is assumed to be an infinite reservoir and thus its concentration is immutable. Our model represents the RO outlet with the Cauchy boundary condition [107] – a mathematical description of dynamic conditions at a model boundary – where the effluent concentrations dynamically depend upon desalination. A glossary of parameters and variables for the equations and calculations are provided in Table S1.

2.2.2 Numerical

The geochemistry and reactive transport components of our RO model are numerically detailed in the following sub-sections.

Permeate Flux

The permeate flux in our model is assumed to be 100% water, similar to other RO models [108], and it is calculated as the change in moles ($\Delta\Phi_e$) of feed solution in any examined cell e. Permeate flux is proportional to the difference between feed pressure P and osmotic pressure π [54, 109, 110]

$$\Delta\Phi_e \ \alpha \ (P - \pi), \tag{2.1}$$

however, these pressures are not readily measured or reported; hence, we calculate the permeate flux via two comparable methods that are elaborated in the following sub-sections.

Method 1: Linear permeate flux One method assumes that permeate flux decreases linearly along the RO module. This causes the concentration – which is represented by the concentration factor (CF) [111, 98, 112, 99, 113]

$$CF = \frac{initial}{final} \ , \tag{2.2}$$

as the quotient of initial to final ionic concentrations (influent vs. effluent), solution masses, or permeate moles [98, 99] – to increase exponentially along the RO module. The negative slope of permeate flux is calculated between the first cell 1 and the last cell n

$$slope = \frac{(\Delta\Phi_n - \Delta\Phi_1)}{n} \ , \tag{2.3}$$

where the simulated membrane-solution interface is discretized into n equal fractions (cells) of the total module length l_{module}. The permeate fluxes in these border cells, $\Delta\Phi_1$ and $\Delta\Phi_n$, are calculated through a system of equations. One of these equations

$$\overline{\Delta\Phi}_e = \frac{\Delta\Phi_{module}}{n} = \frac{\Delta\Phi_n + \Delta\Phi_1}{2} \tag{2.4}$$

equates two definitions of the average permeate flux per cell e: 1) $\overline{\Delta\Phi}_e = \frac{\Delta\Phi_{module}}{n}$ from the total permeate flux over the module $\Delta\Phi_{module}$, and 2) $\frac{\Delta\Phi_n + \Delta\Phi_1}{2}$, as the average between the border cells. The other equation is the definition of relative pressure loss over the RO module [114, 115] ($HL; 0 \leq HL \leq 1$) per eq. (2.1),

$$\Delta\Phi_n = \Delta\Phi_1 * (1 - HL), \tag{2.5}$$

which is $\approx 10\%$ [116, 113, 117]. The substitution of eq. (2.5) into eq. (2.4) – given HL, $\Delta\Phi_{module}$, and n – permits calculating $\Delta\Phi_1$ and $\Delta\Phi_n$, the flux slope of eq. (2.3), and subsequently $\Delta\Phi_e$ from a linear

expression of permeate flux per module cell

$$\Delta\Phi_e = (slope * e + \Delta\Phi_1). \tag{2.6}$$

The calculation sequence for this permeate flux method is summarized:

1. Define HL, $\Delta\Phi_{module}$, and n
2. Calculate the permeate flux slope [eqs. (2.3) to (2.5)]
3. Calculate the permeate flux in each cell e [eq. (2.6)]

Method 2: Linear Concentration Factor The second method of calculating the permeate flux assumes that the CF increases linearly, which causes the permeate flux to decrease non-linearly, along the RO module. The CF slope is calculated analogously to eq. (2.3):

$$slope_{CF} = \frac{CF_n - CF_1}{n}. \tag{2.7}$$

The effluent CF_n is the average CF of all effluent ion concentrations

$$CF_n = \frac{\sum_{i=1}^{j}(C_{i,brine})}{\sum_{i=1}^{j}(C_{i,feed})}, \tag{2.8}$$

where $C_{i,brine}$ is the effluent concentration and $C_{i,feed}$ is the influent concentration of ion i, for all j ions. Defining CF from eq. (2.2) in terms of moles of feed solution (Φ, which is assumed to be 100% water) reveals an equation

$$CF_e = \frac{\Phi_0}{\Phi_e} = \frac{\Phi_0}{\Phi_0 - \Delta\Phi_{(1,e)}} \tag{2.9}$$

that can calculate the moles of feed at the end of an arbitrary cell e (Φ_e), where $\Delta\Phi_e = \Phi_0 - \Delta\Phi_{(1,e)}$ and $\Delta\Phi_{(1,e)}$, as the sum of permeate flux that occurred between cell 1 and the end of cell e, is separately the sum

$$\Delta\Phi_{(1,e)} = \Delta\Phi_e + \Delta\Phi_{(1,e-1)} \tag{2.10}$$

of permeate flux before the start of cell e ($\Delta\Phi_{(1,e-1)} = \sum_{j=1}^{e-1}(\Delta\Phi_j)$) and the permeate flux over cell e ($\Delta\Phi_e$). The initial moles of feed Φ_0 is calculated

$$\Phi_0 = V_{feed} * MW_{H_2O} * \rho_{H_2O}, \tag{2.11}$$

from the volume of the feed channel V_{feed}, which is the product of the module length l_{module} and the cross-sectional area of the feed channel A_{feed}

$$A_{feed} = (A_{module} - A_{permeate}) * \frac{th_{feed}}{th_{unit}}\ , \tag{2.12}$$

where A_{module} and $A_{permeate}$ are the cross-sectional areas of the whole module and the permeate tube, respectively, and th_{feed} and th_{unit} are the thicknesses of the feed channel and the repeating membrane unit in Figure S1, respectively. The linear expression for CF_e

$$CF_e = (slope_{CF}) * e + CF_0 \ , \tag{2.13}$$

is then substituted into eq. (2.9), with the slope from eq. (2.7), to yield an expression for the permeate flux (a negative change in feed moles) at the end of each examined cell e

$$-\Delta\Phi_{(1,e)} = \frac{\Phi_0}{((\frac{CF_n - CF_0}{n}) * e + CF_0)} - \Phi_0 \ , \tag{2.14}$$

which can be substituted into eq. (2.10) with the sum of previous permeate fluxes ($\Delta\Phi_{(1,e-1)}$) to yield the permeate flux over any examined cell e ($\Delta\Phi_e$), analogously to eq. (2.6). Note that $\Delta\Phi_{(1,e-1)} = 0$ when $e = 1$, since there are no previous cells.

The calculation sequence for this permeate flux method is summarized:

1. Define the effluent CF
2. Calculate the feed capacity of the module [eqs. (2.11) and (2.12)]
3. Calculate the CF slope [eq. (2.7)]
4. Calculate the permeate flux in each cell [eqs. (2.9), (2.10), (2.13) and (2.14)]

Comparison of permeate flux methods Scaling predictions from these two permeate flux methods are juxtaposed in Figure 2.1. The most significant difference is observed at the mid-point of the simulated module ($0.47m$), where the linear CF method predicts $0.99\frac{gram}{m^2}$ of Gypsum scale while the linear permeate flux method predicts $0.0196\frac{gram}{m^2}$ of Gypsum scale. The linear CF method subsequently predicts subtly less scale than the linear permeate method. These different distributions are explained by the dependency of scale upon the solution CF – where the exponential increase in CF through the linear permeate flux method causes initially less, and then eventually more, scaling than the linear CF method – however, the scale distribution ultimately equates between these two permeate flux methods to 3 significant digits: $38.7\frac{gram}{m^2}$. These methods are therefore believed to only subtly affect the distribution, and not the total quantity, of scale within a module. Experimental literature is not known that can verify which method better reflects physical systems.

Geochemistry

The geochemistry of RO scaling in our model is predicated upon the kinetic rate laws and thermodynamic equilibria that define each mineral dissolution and precipitation. These chemical processes are encapsulated in the PHREEQC databases that offer different a) geochemical models, b) permissible

ranges of conditions, and c) sets of potential minerals to best represent a given system. These databases are complemented with the ChemW Python package that rigorously calculates the molecular mass of each mineral (see the ChemW PyPI documentation) to permit scaling predictions in the conventional units of $\frac{g\ scale}{m^2\ membrane}$.

Transport

The physical transport of feed through the module is simulated in each timestep by 1) migrating the contents of each cell e to the next cell e+1; 2) repopulating cell 1 as new feed solution enters the simulated module; and 3) deleting cell n as brine exits the simulated module. The feed velocity $v_{feed} = \frac{Q_{max\ feed}}{A_{feed}}$ is calculated from the maximum feed flowrate $Q_{max\ feed}$ ($\frac{m^3}{s}$) and the feed area from eq. (2.12) of the RO module. Default module parameters in Table S1 are sourced from the DOW FILMTEC BW30-400 RO module, similar to other RO models [108], and supplement user-defined module parameters. The maximum simulation timestep $\Delta t = \frac{l_{cell}}{v_{feed}}$ is calculated according to the Courant Condition [118] ($C_{max} = 1 \geq \frac{v_{feed} * t_{max}}{l_{cell}}$) to maintain accurate resolution of the feed flow.

2.3 Use cases

The following sub-sections evince features of our model and its alignment with reported measurements. These studies were conducted through ROSSpy and are available as Python Notebooks in the ROSSpy GitHub repository.

2.3.1 CF and Brine formation

The predicted CF and ionic concentrations of the effluent were verified through comparison with the following three experimental studies, where the reported feed geochemistry and module specifications were parameterized into the model.

Zaman et al.[119] This study examines RO brine, from a full-scale water treatment facility in Australia, to understand which minerals are likely to form as scale. The predicted concentrations in Figure 2.2a were $< 6\% - error$ for all but one of the feed ions.

Ahmed et al.[120] This study examines RO brine from 10 small desalination plants in Oman and 8 plants in the United Arab Emirates (UAE) for the purpose of understanding ideal brine disposal methods. We selected the UAE Qidfa I desalination plant from these 18 plants to replicate, since it provided the most comprehensive details. The predicted concentrations in Figure 2.2b were $< 10\% - error$ for all but one of the feed ions. The CF, in the far-right column of Figure 2.2b, furthermore exhibits a $< 1\% - error$, which supports that the reactive transport processes, notably the permeate flux calculations, are accurate.

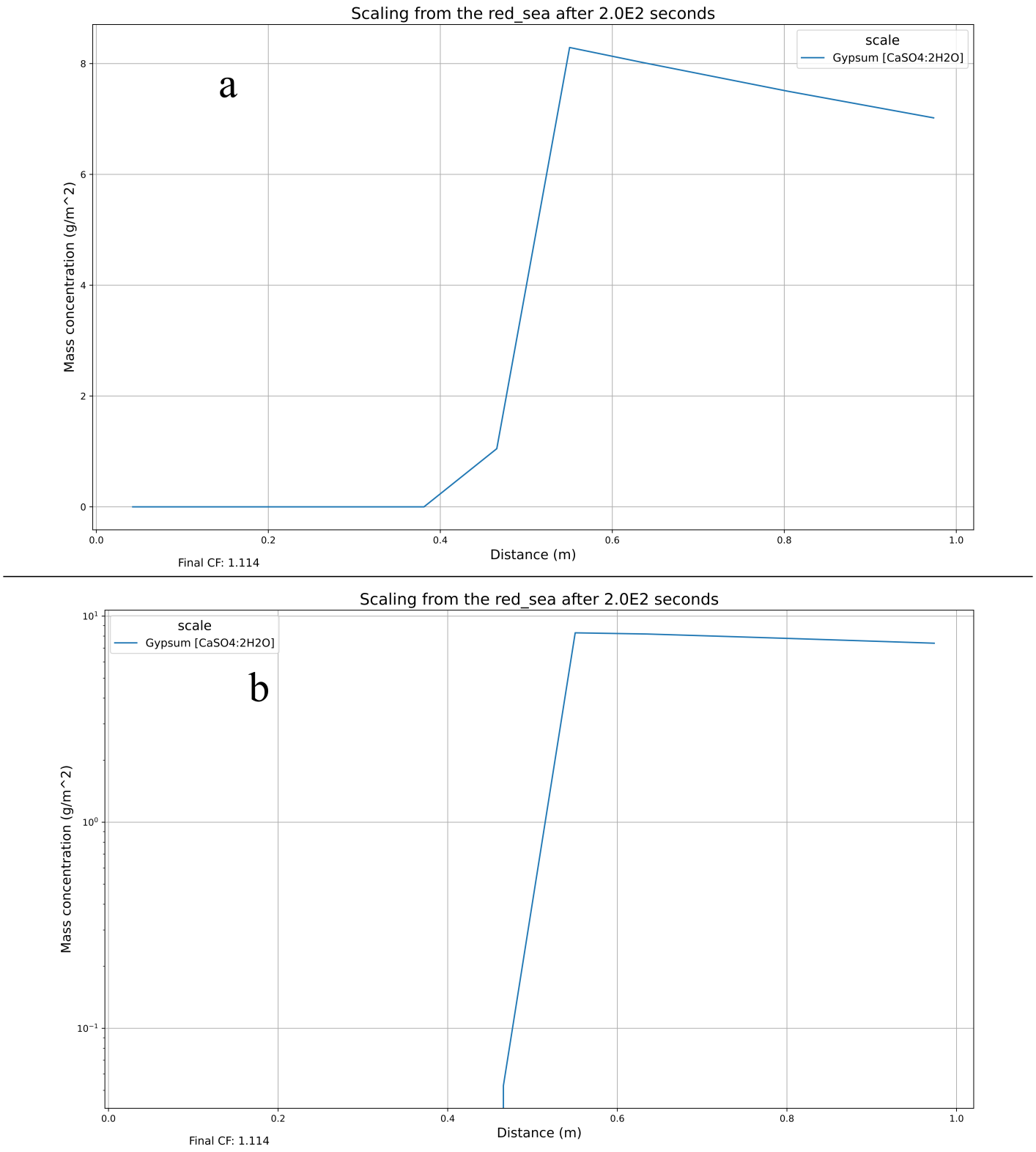

Figure 2.1: Predicted scaling of the Red Sea at $CF_{effluent} = 1.114$ via the a) linear CF and b) linear permeate flux methods. The linear increase in CF of a) slightly homogenizes the distribution of scaling, while the exponential increase in CF of b) skews the distribution of scaling to lesser initially and eventually greater, relative to the linear method of a). These subtle differences in scaling distribution neutralize as the total scaling through both methods are equivalent.

Hajbi et al.[121] This study evaluates the recovery of commodity salts from RO brine at a plant in Tunisia. The authors detail specifications of line D – a polyamide filtration membrane – in the plant system, in addition to the feed geochemistry, which were all parameterized into our model. The predicted concentrations in Figure 2.2c were less aligned than the aforementioned two studies, with two ions exceeding $25\% - error$. This is attributed to 40% fewer feed ions being defined by this study, where the incomplete geochemical representation of the feed skews the geochemical calculations of PHREEQC. This is corroborated by the accuracy of the CF prediction in Figure 2.2c, despite inaccurate concentration predictions, which suggests that the error resides with the geochemical processes and not the reactive transport system.

2.3.2 Scaling

The scaling predictions were verified qualitatively from experimental literature and quantitatively from theoretical calculations, since experimental literature that quantified scalants with feed geochemistry was not discovered.

Quantitative

The quantitative verification consisted of two simple cases of Gypsum precipitation. 1) The first case in Table 2.1 consists of a solution with only Ca^{2+} and SO_4^{2-}, where the ionic concentrations decreased by 0.01859 moles while 0.01961 moles of Gypsum precipitated. This 5% discrepancy in mass balance is attributed to the printed PHREEQC values in this calculation neglecting diffusion within the feed solution, yet diffusion is considered in the final output of PHREEQC. 2) The second case in Table S1 evaluates Gypsum precipitation from desalinating the solution from the first case with that from the Red Sea, which only precipitates Gypsum in our model. The simple solution precipitated 0.181 moles of Gypsum, while the Red Sea precipitated 0.194 moles. This +7%-error is attributed to ionic interactions within the Red Sea feed that are not present by the simple solution of only Ca^{2+} and SO_4^{2-}. These subtle $[5, 7]\%$ deviations, even without considering the coarse assumptions in these simple examples, are relatively minor in the context of other sources of error, such as feed measurements, and still elicit quantitative consistency in scaling predictions.

Qualitative

The scaling predictions were qualitatively verified through three experimental studies.

Karabelas et al., 2020 [100] This study inspired features of ROSSpy by reviewing the state-of-the-art, and future directions, for predictive scaling software. The study also, importantly, describes in its Supporting Information scalants that were observed after desalination with defined conditions. Scaling predictions from these conditions in Figure 2.3a, over a few PHREEQC databases, match the reported scalants ("Calcite but not Gypsum" and a "few other salts, such as Barite and Dolomite, could also

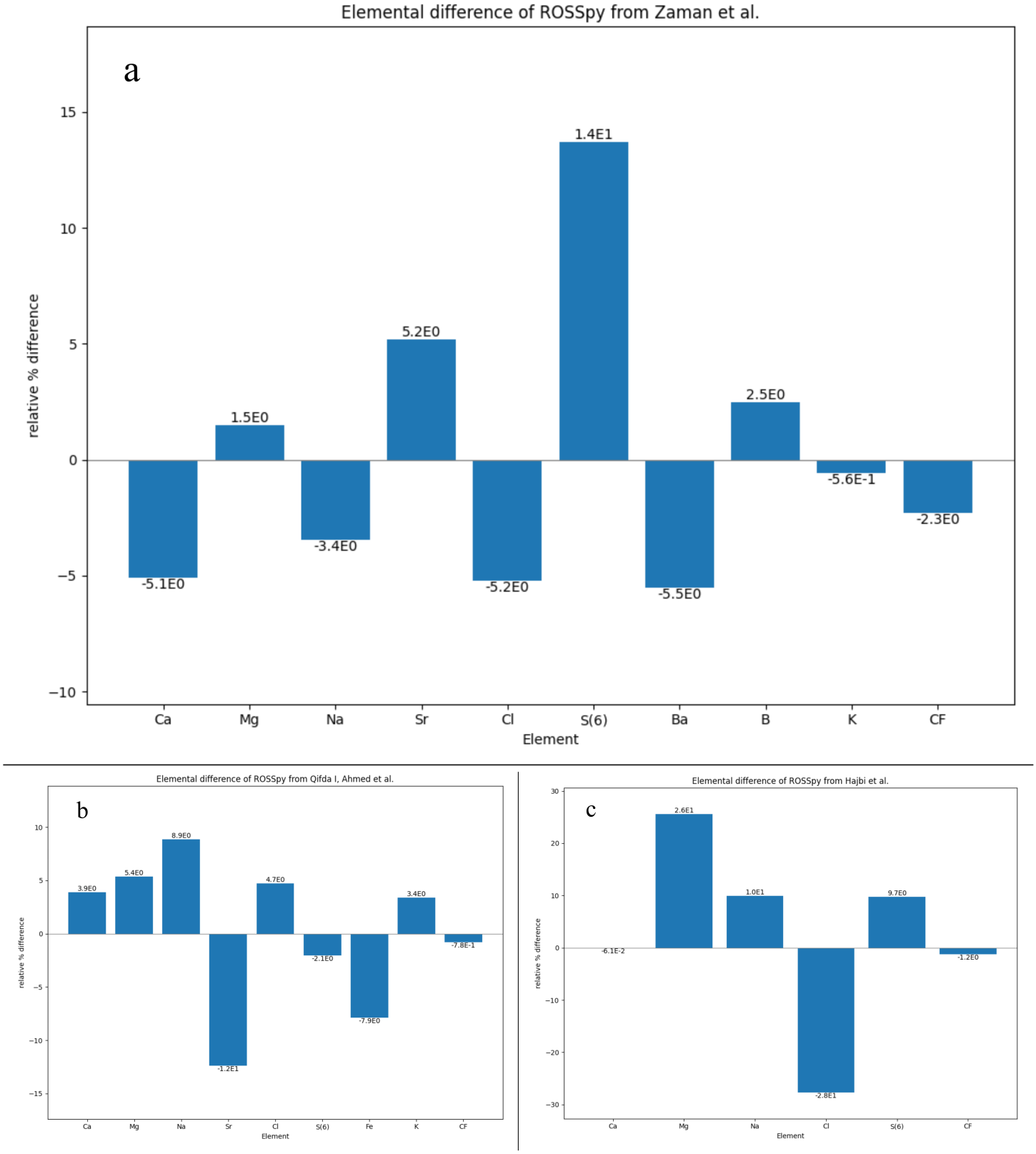

Figure 2.2: The %-error between predicted and experimental brine concentrations from RO plants. Panels a-c) correspond to comparisons with the Zaman et al. [119], Ahmed et al. [120], and Hajbi et al. [121] studies, respectively, and each possess different y-axis scales to best resolve the bars in each graph. The trend is that prediction accuracy is proportional to the quantity of parameterized ions.

	Ca^{2+}	+	SO_4^{2-}	$\leftrightharpoons$	$CaSO_4$
I	0.3545		1.816		0
C	-0.01859		-0.01859		$+0.01961$
F	0.3360		1.797		0.01961

Table 2.1: Gypsum precipitation according to the ICE (Initial, Change, Equilibrium) framework, except that "Equilibrium" (E) is replaced with "Final" (F) since the system does not completely reach equilibrium within the RO module. The $5\% - error$ in row C, between the changes in ionic and Gypsum moles, suggests a subtle discrepancy in mass balance of PHREEQC; however, this is attributed to PHREEQC printing values before diffusion is incorporated in the calculations, per David Parkhurst.

deposit at downstream...") in numerous aspects: 1) Calcite was the primary scalant; 2) Gypsum was not observed; 3) a few other salts precipitated, including Dolomite and Barite, depending upon the PHREEQC database; and 4) these other salts precipitated primarily in the downstream portion of the module.

Karabelas et al., 2014 [65] This study elucidates the mechanisms of incipient scaling from RO desalination – with Gypsum as the archetypal scalant [122]. The ID 28SC trial, which was the most thoroughly described trial, was simulated and Gypsum was the only predicted scalant in Figure 2.3b, just as the reported scalant.

Lee et al., 2009 [123] This study evaluates the use of a membrane bioreactor – a hollow-fiber membrane module design that is mechanistically similar to RO and thus can be represented by our model – to treat wastewater. The wastewater filtration system was simulated, and the only predicted scalant was Calcite in Figure 2.3c, just as the reported scalant.

2.4 Sensitivity analyses

A few sensitivity analyses were conducted with major variables in the following subsections. Additional sensitivity analyses of lesser parameters are presented in the Supporting Information.

2.4.1 Database section

The PHREEQC databases crucially 1) determines the set of minerals that can be simulated; 2) contains all of the kinetic, thermodynamic, and stoichiometric information of each mineral; and 3) employs a chemical activity model: e.g. Pitzer, Debye-Hückel, and Davies in Section 7 of the Supporting Information. The Pitzer model [124, 125], which is implemented in the pitzer PHREEQC database, is touted as being supremely accurate in the concentration range of desalination [126, 127, 128]; however, the narrow breadth of accepted ions and minerals may justify using other databases, such as wateq4, for complex or uncommon feed sources. Each of the 13 databases were simulated in desalinating the Red Sea, where the *Amm*, *Core*10, *LLNL*, and *Minteq.v*4 databases failed to numerically converge while the scaling predictions from the other $\frac{9}{13}$ databases are summarized in Figure 2.4. The database selection evidently alters scaling predictions; thus, the database must be carefully selected for a given system after reviewing the PHREEQC User Manual or inquirying to the PHREEQC user forum `PHREEQCusers.org`.

2.4.2 Feed geochemistry

The default feed waters were constructed from experimental geochemical literature into parameter files that are provided with ROSSpy. Users of ROSSpy are encouraged to simulate their own feed water while emulating the syntax of the default parameter files. We propose experimental data of numerous

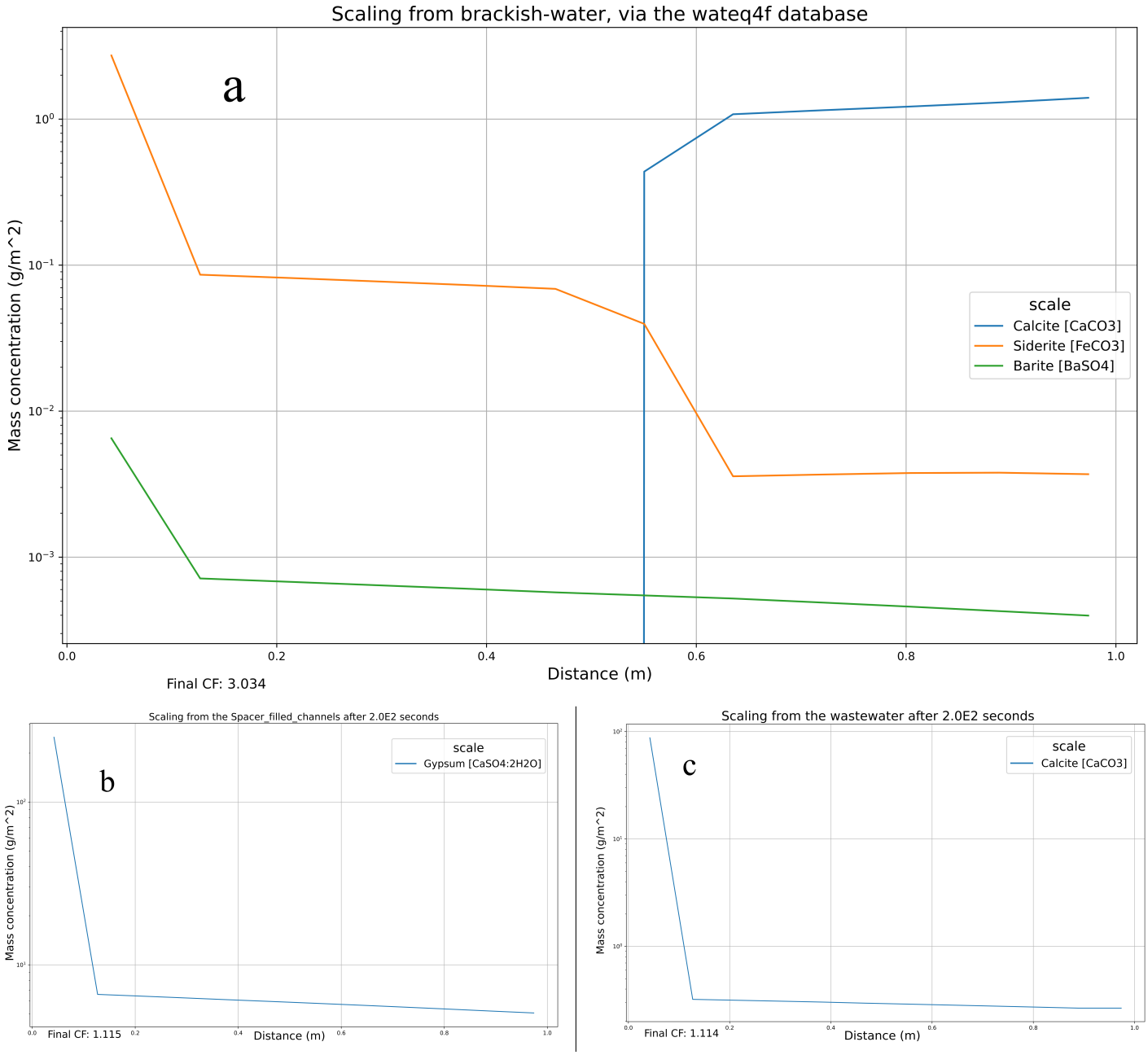

Figure 2.3: The qualitative validation of scaling for a) multiple minerals from the Karabelas et al., 2020 study; b) Gypsum in the Karabelas et al., 2014 study; and c) Calcite in the Lee et al. study.

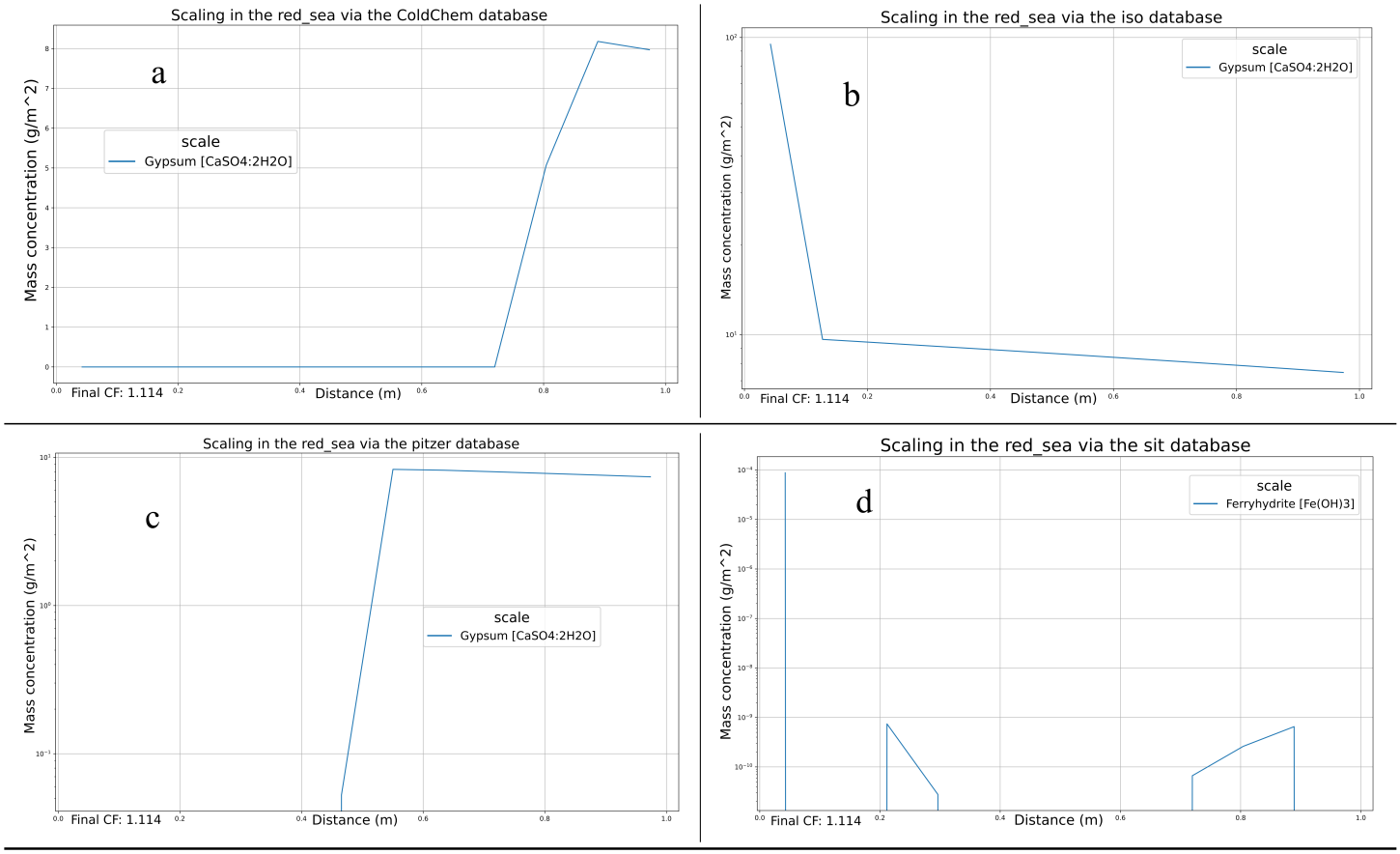

Figure 2.4: Scaling predictions from the a) ColdChem, b) Iso, c) Pitzer, and d) Sit databases, with otherwise identical simulation parameters. These subfigures represent the spectrum of similar yet distinct predictions of scaling during the database sensitivity analysis, and exemplify that the PHREEQC database should be deliberately selected after reviewing the PHREEQC documentation to discern which database is most appropriate for the feed geochemistry.

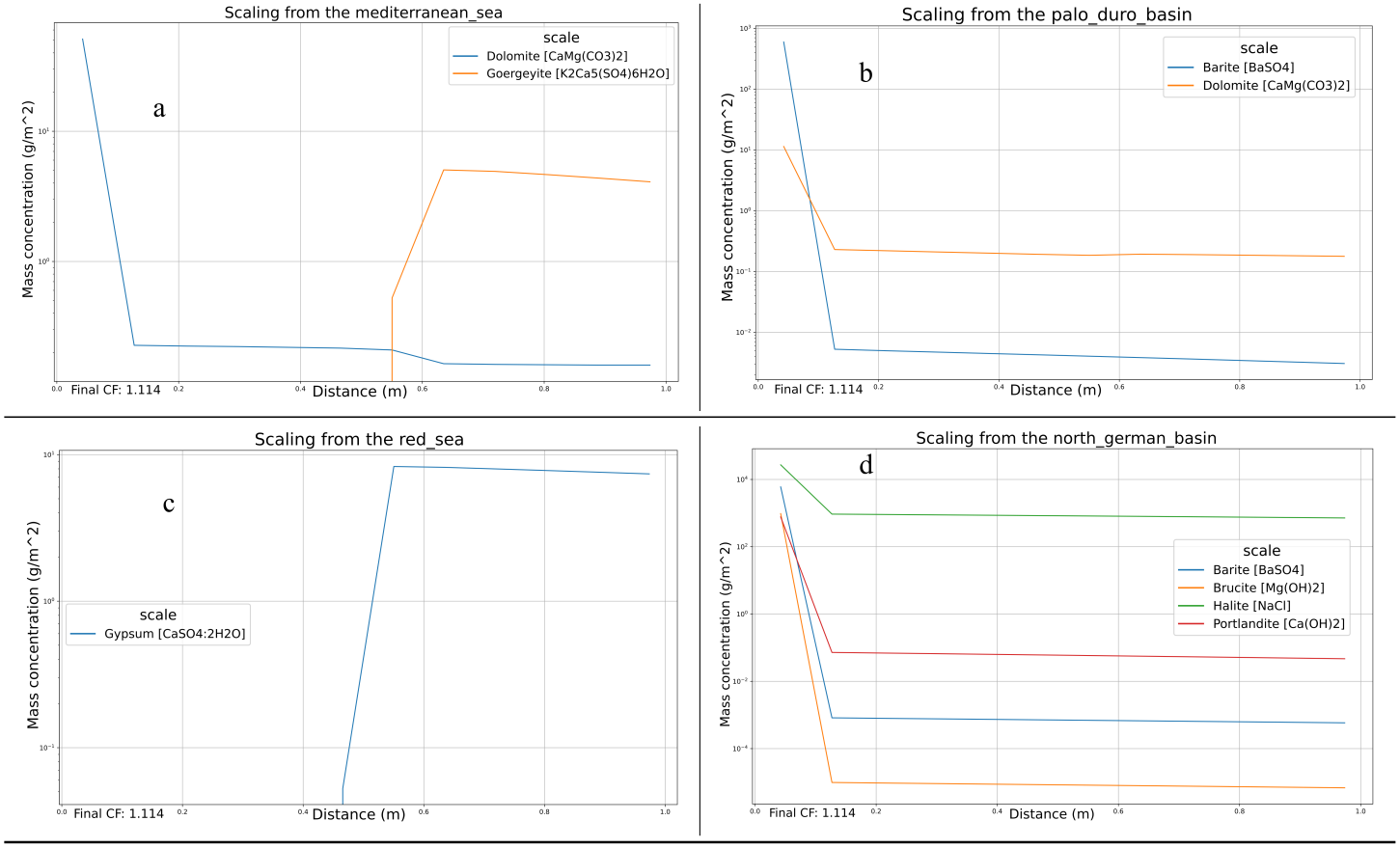

Figure 2.5: Scaling predictions of a) the Mediterranean Sea, b) produced waters from the Palo Duro oil basin, c) the Red Sea, d) produced waters from the North German oil basin, with otherwise identical simulation parameters. These subfigures represent the spectrum of scaling predictions from the variety of different feed sources, which exhibits a high sensitivity of scale predictions to the feed geochemistry.

other water sources in Section 5 of the Supporting Information that can predicate feed water files; although, direct measurement of the simulated feed water is preferable to avoid significant influences of anthropogenic pollution [129] and seasonality [130] in reported measurements. Thee default water sources, which include both natural seas and produced waters from oil wells, were contrasted in Figure 2.5, where the scaling and brine predictions differed significantly amongst these feed water sources.

2.5 Software

ROSSpy, which is conceptualized by Figure 2.6, combines our one-dimensional RO model with post-processing operations that facilitate interpretation of the simulation results. The software a) translates parameters into a PHREEQ input file; b) executes that input file via PHREEQpy; c) processes the simulation results into figures and data tables via Matplotlib [131] and Pandas [132] Python packages, respectively; and d) exports all of the simulation content – e.g. the PHREEQ input file, SVG data figures, and CSV files of parameters, variables, data, and brine predictions – into a specified folder and directory.

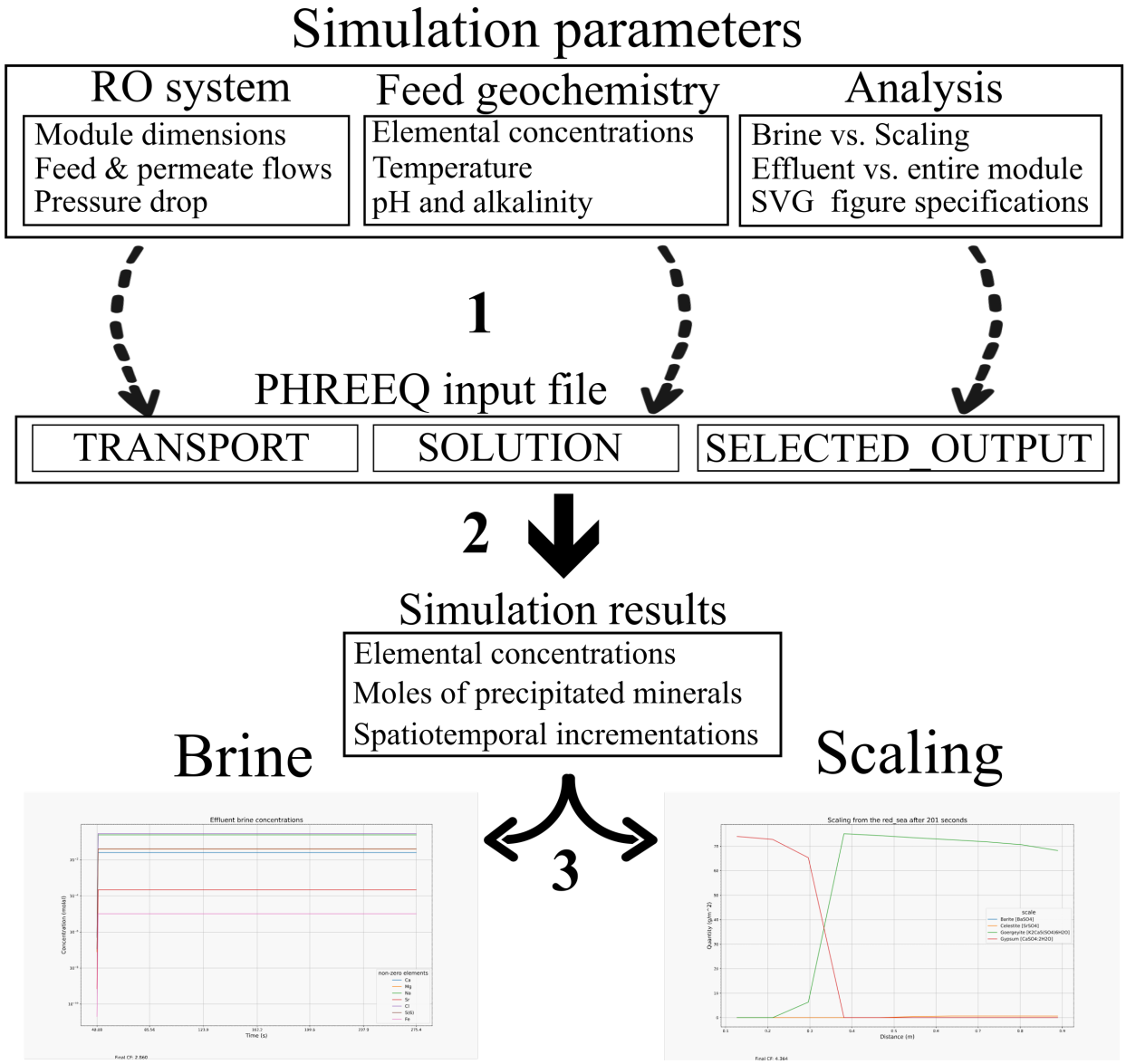

Figure 2.6: The ROSSpy workflow. Step 1 describes the translation of parameters – i.e. module specifications, feed geochemistry, and simulation analysis – into the corresponding code blocks of a PHREEQ input file. Step 2 describes executing the PHREEQ input file via either PHREEQpy in ROSSpy, or via the PHREEQC batch software in the interactive version of ROSSpy (iROSSpy) that is under development. Step 3 describes processing the predictions of brine concentrations or scaling quantities into representative figures and datatables, which are ultimately exported.

The simulation data may be sliced into one-dimensional sets of distance or time that can be plotted against either scaling density or brine concentrations (Figures S2-S3) (see ROSSpy documentation).

2.6 Conclusion

A one-dimensional approximation of RO reactive transport geochemistry, executed in PHREEQC, is a practical and accurate representation of mineral scaling during desalination. The simulation predictions

of this model were quantitatively and qualitatively verified for a few use cases, with both theoretical expectations and experimental data where it was available. The API implementation of this model (ROSSpy) furthermore meets identified needs of the community – e.g. rapidly designing, executing, processing, and exporting simulations of RO scaling – while maintaining accessibility through its lightweight design and its open-source code. We expect that this one-dimensional model and the unique attributes of ROSSpy will facilitate scaling research and ultimately improve the efficiency of RO desalination towards alleviating chronic water insecurities in the world.

2.7 Funding

This work was prepared in partial fulfillment of the requirements of the Berkeley Lab Undergraduate Research (BLUR) Program, managed by Workforce Development & Education at the Berkeley Lab. The project was also partly funded by NSERC Discovery, MITACS Accelerate, CEWIL, and Canada Summer Jobs.

2.8 Acknowledgement

The authors thank Ethan Sean Chan for his technical assistance in developing a graphical interface of ROSSpy (iROSSpy) that will be released in a future version.

2.9 Supporting Information

2.9.1 ROSSpy

The variables and terms that comprise our model are defined in Table S1.

Table S1: Glossary of ROSSpy variables.

variable	name	description
l	length	longitudinal dimension of the module or module cell
n	number of module cells	quantity of discretizations of the module
Φ_e	moles	the $moles_{H_2O}$ that exist in cell e
$\Delta\Phi_e$	permeate flux	the $moles_{H_2O}$ that are removed in cell e
HL	head loss	reduction of pressure over the module distance
PE	permeate efficiecy	attenuation of permeate flux from pre-existing inefficiencies
CF	concentration factor	solution concentration of cell e normalized to the influent concentration
X	mass	water mass in the maximally filled feed channel
V	velocity	feed velocity through the feed channel
A	area	cross-sectional area of the RO module
th	thickness	thickness of a module dimension
Q	volumetric flow	feed flow through a maximally filled feed channel
Δt	time	timestep of the simulation that adheres to the Courant condition
C_{max}	Courant constant	maximal value of the Courant constant to meet the Courant condition
ϕ	total concentration	total ionic concentrations in the simulation
C	specie concentration	concentration of an individual specie
v	stoichiometry coefficient	coefficient for the respective compound in the balanced equilibrium reaction

continuation of Table S1

variable	name	description
N	number of reactions	quantity of reactions that contain a respective compound
R	reaction flux	$\frac{mmol}{hour}$ flux of an equilibrium reaction
Ω	thermodynamic displacement	logarithm of the $\frac{Q_{dissolution}}{K_{sp}}$
k_m	rate constant	dissolution and precipitation rate constant
a	activity	chemical activity of the respective compound
η & p	parameter	experimentally determined parameter
ΔG	Gibbs free energy	Gibbs free energy of the dissolution and precipitation reactions
K	equilibrium constant	thermodynamic equilibrium of the respective reaction
M	number of minerals	quantity of minerals in the studied system
γ	activity coefficient	coefficient of metabolite activity in a respective system
z	charge	compound charge of the respective metabolite
μ	ionic strength	charge-weighted concentration of a solution
A & B	parameter	experimentally determined parameter
a_j & b_j	fitted parameter	geochemical parameter that is fit to the system
W_{aq}	water mass	mass of water in the system

The distinctions between slicing the simulation data through time or module distance is exhibited with brine in Figure S1 and scaling in Figure S2, respectively.

A cross-section of an RO module, which highlights boundaries of the single- and dual-domain solution models, is depicted in Figures S5.

2.9.2 PHREEQC consistency

ICE table calculations

The expected precipitation in the presented ICE table of Table S2 was determined as x in the following derivation:

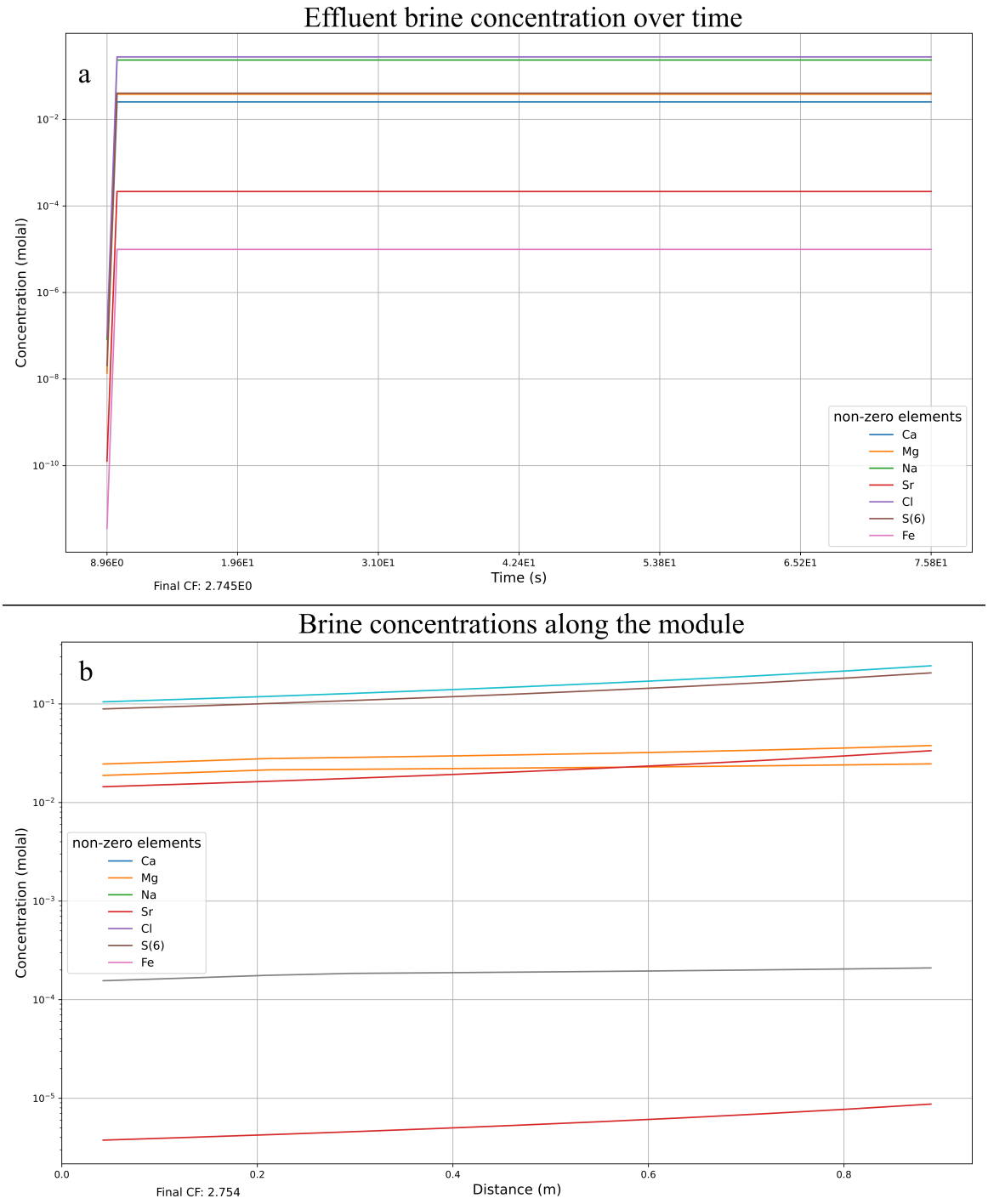

Figure S1: Brine formation while slicing through either a) time at the final cell or b) distance at the final time. The end concentrations slightly differ between these two simulation perspectives, where the all_time perspective calculates the true end of the last cell while the all_distance perspective calculates the mid-point of the last cell and thus has a slightly lower concentration. The brine represents desalination of the Red Sea through the BW30-400 module.

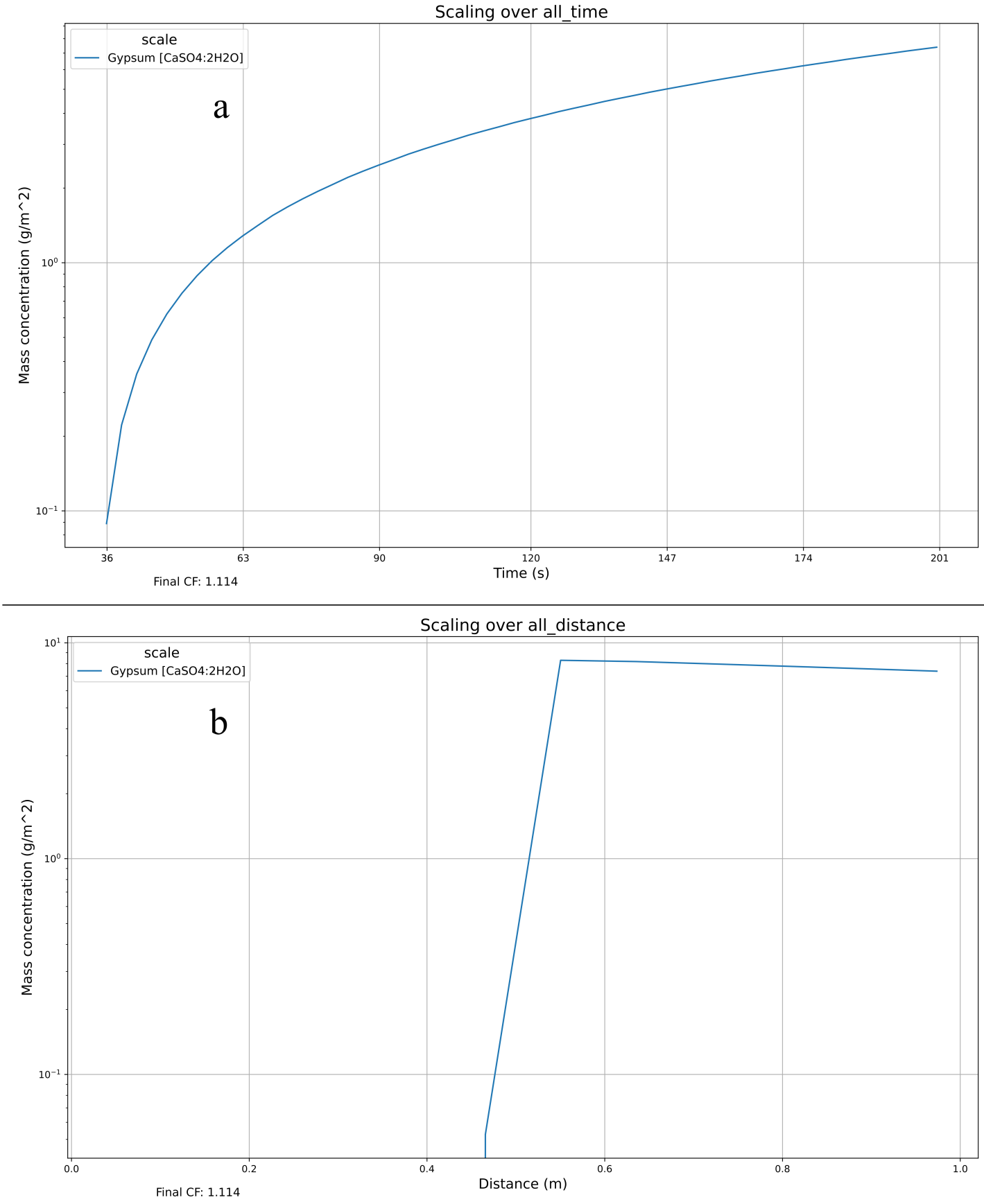

Figure S2: Scaling while either slicing through a) time at the final cell or b) distance at the final time. The underlying simulation was of the Red Sea through the BW30-400 module.

$$
\begin{aligned}
K_{sp} &= [a_{Ca^{2+}} - x]^1 * [a_{SO_4^{2-}} - x]^1 \\
K_{sp} &= (\gamma * [Ca^{2+}] - x) * (\gamma * [SO_4^{2-}] - x) \\
10^{-4.58} &= ((0.19 * 0.020594) - x) * ((0.06 * 0.105462) - x) \\
10^{-4.58} &= (0.003913 - x) * (0.00633 - x) \\
10^{-4.58} &= 2.477E-5 - 0.01024 + X^2 \\
0 &= -1.54E-6 - 0.01022x + x^2 \\
\therefore \quad x &= 0.0104\ molal = \frac{\boxed{0.181\ \text{moles}}}{17.67\ kg\ water} \quad .
\end{aligned}
\tag{S1}
$$

The activity coefficients (γ) for Ca^{2+} and SO_4^{2-} were sourced from PHREEQC for this specific solution system. The 17.67 kg mass of water corresponds to the mass maximum capacity of the simulated BW30-400 module.

The predicted precipitation in the presented ICE table of Table 1b (*gypsum_pore_volume*) are similarly derived:

$$
\begin{aligned}
gypsum\_pore\_volume &= gypsum\_all\_shifts * \frac{cells\_per\_module}{total\_simulation\_shifts} \\
&= \sum_{i=1}^{n} (Gypsum_i) * \frac{12}{51} \\
&= 0.823 * \frac{12}{51} \\
&= 0.194\ moles \quad .
\end{aligned}
\tag{S2}
$$

The $\frac{12}{51}$ is the fraction of simulation shifts that correspond to a single module or pore volume, where the simulated module was discritized into 12 cells. This isolates scaling from a single module, instead of the accumulation of scaling from multiple pore volumes, which renders the quantity directly comparable with the expected quantity.

	Ca^{2+}	$+$	SO_4^{2-}	$\leftrightharpoons$	$CaSO_4$
I	0.003913		0.00633		0
C	$-x$		$-x$		$+x$
F	$0.003913 - x$		$0.00633 - x$		x

Table S2: Gypsum precipitation according to the ICE (Initial, Change, Equilibrium) framework, except that "Equilibrium" (E) is replaced with "Final" (F) since the system does not reach equilibrium while within the module. The estimated Gypsum precipitation from a solution of Ca^{2+} & SO_4^{2-} – based upon the K_{sp} of Gypsum and the activity coefficients of this solution from iPHREEQC – is derived in S1 for the system in this table.

Evaporation versus transport desalination

The mechanism of concentrating a solution, either via evaporation or desalination, should not alter scaling predictions, ceterius paribus. Figure S3 contrasts scaling predictions from evaporation and desalination of the Red Sea, where the two mechanisms are approximately equivalent. Differences are postulated to originate from the consideration of advection in the latter but not the former.

2.9.3 In-series RO arrangements

In-series arrangements of multiple RO modules are represented by compounding individual modules. We determined that this approach is preferential to a few other methods: e.g. amplifying the characteristics of a single RO module, such as those in Table S3, by a scalar $r = \frac{\Phi_{\Delta multi-module}}{\Phi_{\Delta module}}$, where the $\Delta\Phi_{multi-module}$ is the total permeate flux of the multi-module system that can be parameterized or approximated through eq. (8). The substitution of CF_{multi} for CF_e and $\Delta\Phi_{multi-module}$ for Φ_e into eq. (9) permits calculating the $\Delta\Phi_{multi-module}$.

2.9.4 Water bodies

Additional feed parameter files can be composed by emulating the structure of the default feed parameter files. Literature sources that may foster the development of such feed parameter files for numerous potential feed sources are provided in Table S4 with the respective citations of the experimental geochemical data.

2.9.5 Dual domain

Our model represents the feed solution with the single-domain model, despite that the dual-domain model in the module cross-section of Figure S5 is more fundamentally accurate, since our attempts to encode the latter in PHREEQC have been unsuccessful. We represent the mobile phase (bulk solution) as one set of membrane cells – $[1, n]$ $n \in W$ – and the immobile phase (CP layer) as a separate set of cells – $[n + 2, m]$ $m \in W > n + 2$. These cell sets exchange solvent at a parameterized rate – the Exchange Factor $\frac{1}{s}$ (EF) – which in Figure S4 is very influential upon the simulation predictions; however, the brine concentrations dilute in both solution compartments during desalination simulation. The scaling predictions are equally non-sensible. Our model therefore uses the single-domain model, which appears to be an acceptable approximation per our validations. The developer of PHREEQC – David Parkhurst – is uncertain whether the dual-domain model is compatible with the PHREEQ code, which assures us that the single domain model may be the best approximation of desalination reactive transport that is accessible to our open-source framework.

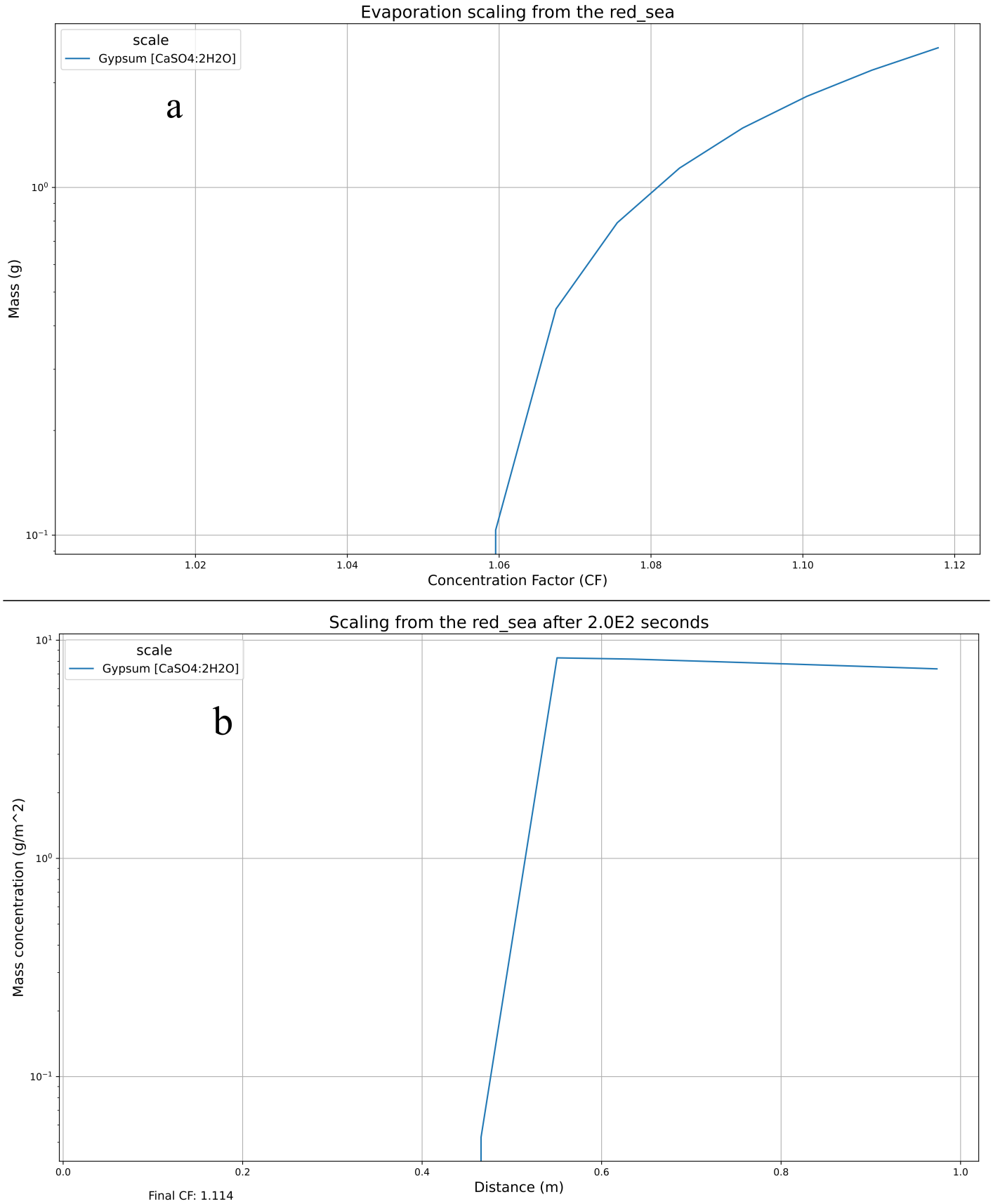

Figure S3: Scaling while a) evaporating and b) desalinating the Red Sea. The two scaling predictions are qualitatively similar, however, even after accounting for the accumulation amongst different pore volumes, the evaporation predictions ($3.36g$) are less than those of the reaction transport simulation ($5.27g$). The difference may be the absence of advection in the evaporation analysis.

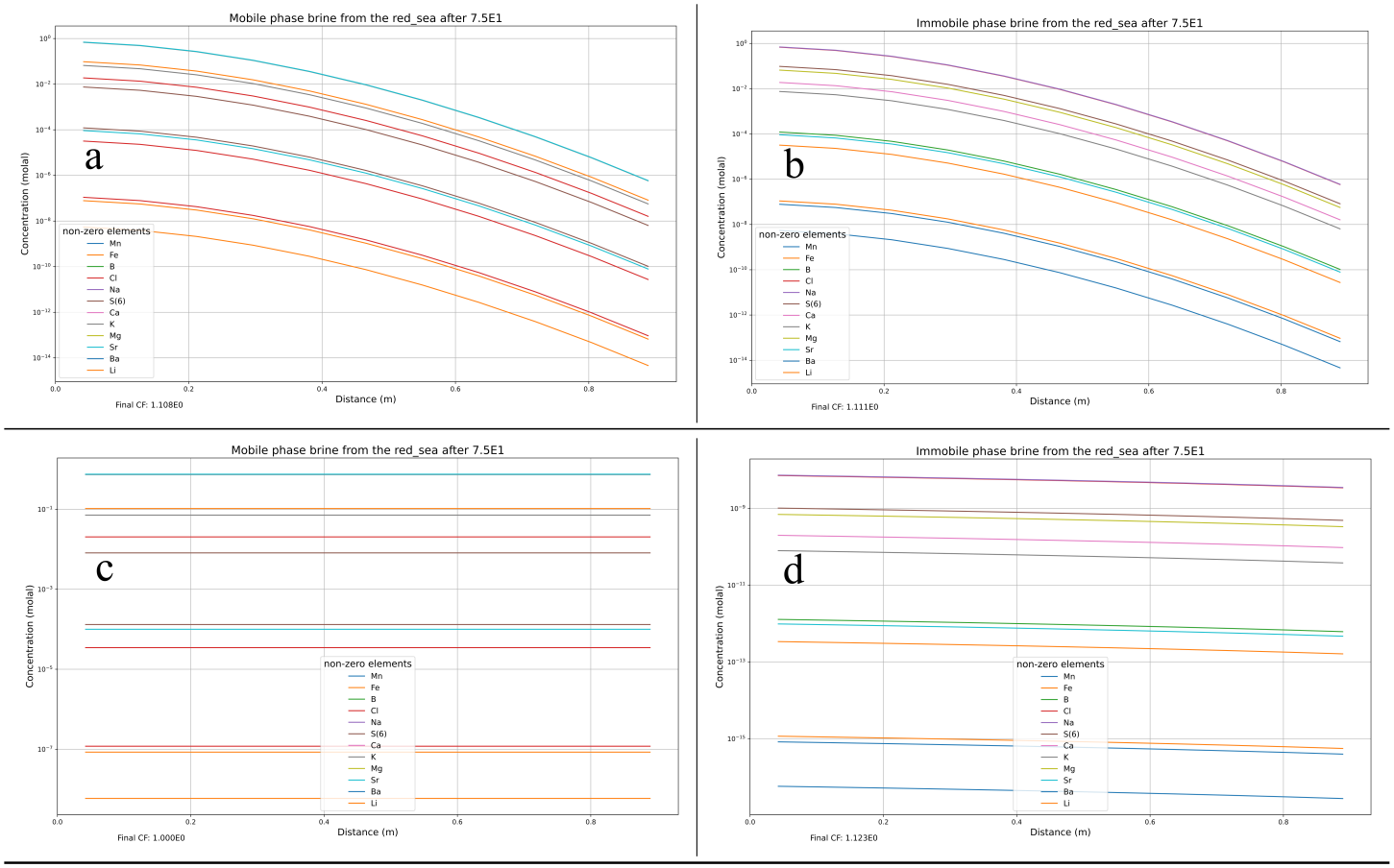

Figure S4: Counter-intuitive brine predictions from dual domain simulations with different exchange factor (EF) values, which is the $\frac{1}{s}$ rate constant of solvent exchange between the mobile and immobile solution phases. Panels a) and b) depict the mobile (bulk) and immobile (CP) phases when $EF = 1E10$, while panels c) and d) depict the mobile and immobile phases when $EF = 1E-10$, respectively. These non-sensible results motivated our use of the single-domain model to represent RO feed flow.

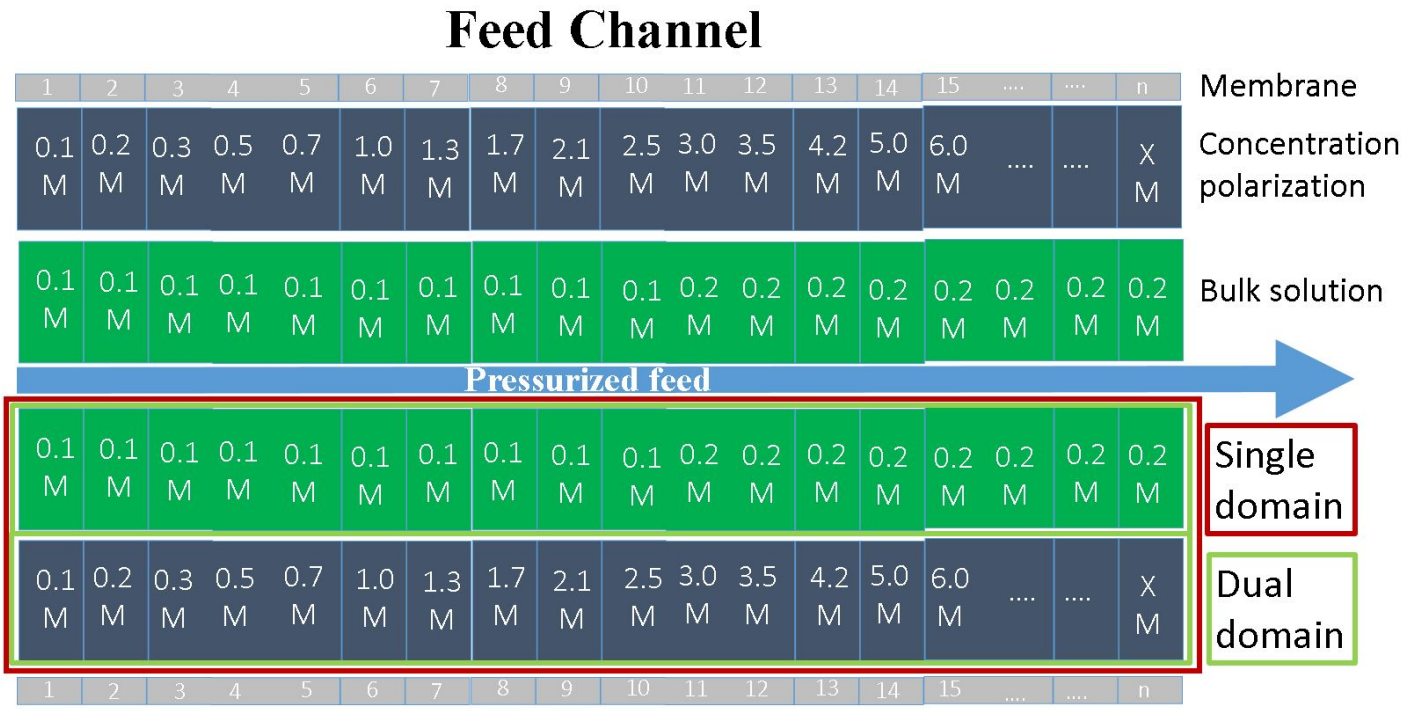

Figure S5: A conceptual cross-section of the RO module. The membrane layers on top and bottom of the figure are discretized into an arbitrary n cells. The figure illustrates the reactive transport phenomena, where the feed solution progressively becomes more concentrated as it transports through the module. The CP layer becomes much more concentrated than the bulk solution as a consequence of the no-slip boundary condition, where the velocity gradient reaches zero at the membrane surface and thus does not diffuse. These bulk and CP solutions are resolved in the dual-domain model (green boxed regions) and are granulated into a single solution by the single-domain model (red boxed regions). The latter was implemented in our model by necessity of PHREEQC.

Parameter	Value	Source
Module (m)		
length	1.016	BW30-400 [133]
diameter	0.201	BW30-400 [133]
permeate tube diameter	0.029	BW30-400 [133]
Membrane (mm)		
filtration layer	0.00025	[134, 135]
Feed spacer	0.8636	BW30-400 [133] & [136]
Permeate spacer	0.3	
Polysulphonic layer	0.05	
Support layer	0.15	
Windings $\left(\frac{th_{total}}{th_{membrane}}\right)$	86	BW30-400 [133]
Membrane cross-section (m^2)		
Module	0.0317	BW30-400 [133]
Permeate tube	0.000661	BW30-400 [133]
Filtration section	0.0311	BW30-400 [133]
Feed channel	0.0157	BW30-400 [133]
Feed channel capacity		
Volume (m^3)	0.0159	BW30-400 [133]
Mass (kg)	15.86	BW30-400 [133]
Fluid flow ($\frac{m^3}{second}$)		
Permeate	0.000463	BW30-400 [133]
Max Feed	0.00442	BW30-400 [133]

Table S3: Default dimensions of an RO module, with corresponding citations, that are primarily based upon the DOW FILMTEC BW30-400 RO module, following precedence from other software [108].

2.9.6 PHREEQ

The most pertinent calculations of PHREEQC for our model are summarized in the following sub-section, while the version 3 PHREEQC User's manual provides a rigorous description of all PHREEQC operations.

PHREEQ calculations

The total concentration Ψ_i of ionic species i is calculated in each timestep,

$$\Psi_i = C_i + \sum_{j=1}^{J} (v_{ij} * C_j), \tag{S3}$$

Water body	Geochemical measurements
Indian Ocean	[137, 138, 139, 140, 141, 142, 143, 144]
Sargasso Sea	[145, 146]
South China Sea	[147, 148, 149, 150, 151]
Greek Coast	[152, 153, 154]
Toyko Bay	[155]
California Coast	[156, 157, 158]
North Atlantic	[159, 160, 161, 162, 163, 164, 165, 166, 167]
Baltic Sea	[168, 169]
North Pacific	[170, 171]
South Pacific	[172, 173]
General natural waters	[174, 175, 176, 177, 178, 179, 180]
Mississippi Salt Dome Basin	[181]

Table S4: Proposed literature of potential feed water that can be adapted into parameter files for simulation in our model, or specifically ROSSpy.

where C_i is the molal concentration of dissolved i; J is the set of compounds that contain i; C_j is the molal concentration of compound j that contains i; and v_{ij} is the stoichiometric coefficient for the moles of i per mole of compound j. The mineral precipitation equilibria over the simulation time t is calculated through a similar equation,

$$\frac{\partial \Psi_i}{\partial t} = \sum_{m=1}^{N_m} (v_{mj} * R_m), \tag{S4}$$

where N_m is the set of reactions that include specie i; v_{mj} is the stoichiometric coefficient for the moles of i per mole of mineral m; and R_m is the reaction flux of dissolution or precipitation for $(+)$ and $(-)$, respectively,

$$R_m = sgn[\Omega] * A_m * k_m * (\Pi(a^n))|e^{\frac{\eta * \Delta G}{RT}} - 1|^p, \tag{S5}$$

where $\Omega = log\left(\frac{Q_{dissolution}}{K_{sp}}\right)$ and, for the simulated mineral m, A_m is the reacting surface area; k_m is the rate constant of dissolution or precipitation; Q_m is the ion activity product constant; and η and p are experimentally determined parameters. The $|e^{\frac{\eta * \Delta G}{RT}} - 1|^p$ term simplifies to 1 for irreversible precipitation or dissolution. The set of eqs. (S3) and (S4) necessitates that any perturbations to ionic concentrations $\frac{\partial \Psi_i}{\partial t}$ manifest from complexation equilibria. The molal concentration C_j of compound j is discerned,

$$C_j = \frac{\Pi_{j=1}^{N_c} (\gamma_j * K_j)^{v_{ij}}}{\gamma_j * K_j}, \tag{S6}$$

where N_c is the set of linearly independent chemical reactions; γ_j is the activity coefficient of compound j; and K_j is the equilibrium constant

$$K_j = a_j \Pi_m^{M_{aq}} (a_m)^{-v_{m,j}}, \tag{S7}$$

where M_{aq} is the number of minerals in the aqueous system; $v_{m,i}$ is the stoichiometric coefficient of compound j per mole of mineral m; and a_j and a_m are the activity coefficients of compound j and mineral m, respectively. The activity coefficient γ_j is calculated through either the Debye-Hückel model [182],

$$log(\gamma_j) = -A * z_j^2 \sqrt{\mu}, \tag{S8}$$

the WATEQ Debye-Hückel model [182],

$$log(\gamma_j) = \frac{-A * z_j^2 * \sqrt{\mu}}{1 + B * a_j^0 * \sqrt{\mu}} + b_j \mu, \tag{S9}$$

the Davies model [183],

$$log(\gamma_j) = -A * z_j^2 (\frac{\sqrt{\mu}}{1 + \sqrt{\mu}} - 0.2\mu), \tag{S10}$$

or the empirical Pitzer model [124], where A and B are experimentally determined parameters; a_j^0 and b_j are fitted parameters; z_j is the charge of compound j; and μ is the ionic strength of the solution

$$\mu = \frac{1}{2} \sum_{j=1}^{N_{aq}} z_j^2 \frac{n_j}{W_{aq}}, \tag{S11}$$

where W_{aq} is the simulated water mass and n_j

$$n_j = C_j * W_{aq} = \frac{K_i * W_{aq}}{\gamma_j * (\Pi_m^{M_{aq}} (a_m)^{v_{m,j}}} \tag{S12}$$

is the moles of compound j. These calculations and geochemical models are more thoroughly described in the PHREEQC manual and in the cited literature.

Chapter 3

A suite of packages for scalable Whole Cell Models: WCMpy

3.1 Introduction

The development of whole-cell models (WCMs) [184] is purported to be a defining challenge of the 21st century [185]. WCMs amalgamate specialized models of cellular systems – e.g. the metabolome and its kinetics rate laws; the genome and its translational units; and the proteome and its functional proteins – into a single model that represents the entirety of a cell. This endeavor offers the unique opportunity to assess the completeness of cellular theory [186, 187] and to answer research questions in medicine [188, 189] and synthetic biology [190]. WCMs are rooted in the Newtonian perspective that a complete model of both cellular biochemistry and environmental conditions can reproducibly recreate the phenotypes and diversity that are observed experimentally. An atomic-resolution molecular dynamics (MD) simulation of an entire cell (all $1E9$ molecules [191, approximated from cellular mass]) may be the ultimate tool to answer these audacious biological questions; however, since the state-of-the-art of MD is currently at the level of proteins [192], membranes [193, 194, 195], or small cells [196] for microseconds, WCMs are the state-of-the-art for simulating cellular chemistry [197] at biological timescales (hours to days).

The first WCMs [198] were rudimentary systems of ordinary differential equations that often incorporated simplified assumptions of growth [199], such as the Monod kinetics model [200] which assumes that growth is solely contingent upon the glucose concentration. The advent of genome sequencing at the turn of the 21st-century [201, 202] facilitated the development of genome-scale metabolic models (GEMs) [203, 204], which resolved genome-protein-reaction relationships [205] in metabolic systems and thereby improved the biochemical resolution of these WCMs from the original mathematical frameworks [206, 207].

GEMs are executed with the flux balance analysis (FBA) algorithm [208, 209], which distills metabolic systems into a matrix of reaction stoichiometry (S) and a vector (v) of variable reaction fluxes $\left(\frac{mmol}{g_{DW} * hour}\right)$. The S matrix consists of a row for each chemical, a column for each reaction, and the corresponding

stoichiometry of a chemical in a reaction (negative for reactants, and 0 for chemicals that are not in the reaction) as each matrix element. The S matrix for this example three reaction system

$$\begin{aligned} aA + bB &\xrightarrow{v_1} cC + dD \\ aA + dD &\xleftrightarrow{v_2} yY + zZ \\ cC + zZ &\xrightarrow{v_3} growth\ , \end{aligned} \tag{3.1}$$

would be $\begin{bmatrix} -a & -a & 0 \\ -b & 0 & 0 \\ c & 0 & -c \\ d & -d & 0 \\ 0 & y & 0 \\ 0 & z & -z \end{bmatrix}$. The v vector, e.g. $\begin{bmatrix} v_1 \\ v_2 \\ v_3 \end{bmatrix}$ for the reactions of eq. (3.1), contains the combination of reaction fluxes that corresponds with an optimum value of a metabolic objective, which is conventionally cellular growth (*growth* in eq. (3.1)). Multiple different v vectors can correspond to the same optimized objective value, which defines a linear space of objectively equivalent flux vectors [210] that is explored through a variation of FBA called flux variability analysis (FVA) [211, 212]. The FBA algorithm uses matrix algebra and a chemical steady-state for each metabolic concentration $\frac{dC}{dt} = S \cdot v = 0$, where the biological objective of FBA is presumed to be $> 10^{15}$ times slower than metabolic reactions per se [213], to efficiently determine optimal v vectors. This feature allows FBA to execute without kinetic rate laws, which is essential since many metabolic reactions have not been kinetically described; however, FBA is consequently independent of time and is therefore not directly applicable in biological workflows such as WCMs that attempt to simulate biology over time.

The dynamic FBA (dFBA) method introduces time dependency to the FBA algorithm through kinetic flux constraints. Mathematical constraints are boundaries – e.g. 1 and 5 in this expression $1 < x < 5$ – that in the context of FBA tighten the vector space, i.e. reduce the set of v vectors that yield the same optimization value [214], to improve the accuracy and precision of flux predictions. Standard flux constraints are $[0, 1000]$ for irreversible reactions and $[-1000, 1000]$ for reversible reactions. These constraints, which coarsely represent metabolic limitations of substrate diffusion and thermodynamic favorability [215], approximately capture experimental systems [205, 216]; nevertheless, constraints for other chemical influences [217], such as the following few examples, improve the precision of FBA predictions [218]:

1. **Physicochemical** - constraints that directly reflect physical laws of mass and energy conservation, and the thermodynamic favorability or free energy of a reaction [219]

2. **Topological** - constraints that reflect compartmentalization and chemical gradients within a cell [220]

3. **Environmental** - constraints that reflect nutritional limitations in the extracellular space

4. **Regulatory** - constraints that reflect feedback mechanisms which govern enzymatic activity [221]

The kinetic constraints of dFBA constrain a reaction flux to known rate law for a reaction in the model [222, 223, 224, 225] – e.g. $12.2 \leq v_1 \leq 12.2$ for a calculated reaction flux of 12.2. The dFBA method entails a few steps: 1) known rate laws, e.g.

$$\begin{aligned} \frac{d[C]}{c * dt} = \frac{d[D]}{d * dt} = v_1 = \frac{V_{max1} * [A] * [B]}{K_{M_1} * [A] + K_{M_2} * [B]} \\ \frac{d[growth]}{dt} = v_3 = \frac{V_{max3} * [C] * [Z]}{K_{M_5} * [C] + K_{M_6} * [Z]} \end{aligned} \tag{3.2}$$

for the system of eq. (3.1), calculate reaction fluxes based upon the chemical concentrations of the previous timestep ($[A]_{t-1}$, $[B]_{t-1}$, $[C]_{t-1}$, $[D]_{t-1}$, and $[Z]_{t-1}$), or the initial concentrations for the first timestep; 2) the FBA algorithm determines fluxes for reactions without a kinetic constraint; and 3) the present chemical concentrations ($[A]_t$, $[B]_t$, $[C]_t$, $[D]_t$, and $[Z]_t$) are updated with the sum of products of the chemical stoichiometry and the predicted fluxes of each reaction

$$\begin{aligned} [A]_t &= [A]_{t-1} + (-v_1 * a - v_2 * a) \\ [B]_t &= [B]_{t-1} + (-v_1 * b) \\ [C]_t &= [C]_{t-1} + (v_1 * c - v_3 * c) \\ [D]_t &= [D]_{t-1} + (v_1 * d - v_2 * d) \\ [Z]_t &= [Z]_{t-1} + (v_2 * z - v_3 * z) \end{aligned} \quad . \tag{3.3}$$

These steps repeat with each timestep.

The ability to tailor constraints for a variety of chemical phenomena allows the FBA algorithm to studying numerous perturbations of metabolism. A few noteworthy applications of FBA include: e.g. medicine, through a) understanding diseases [226], b) studying bacterial growth rate [216], c) predicting the lethality of gene knockouts [214], d) assessing the efficacy of antimicrobial agents [209], and e) investigating microbial communities [227, 228] such as the human microbiome [229, 230]; bioengineering, through rationally designing a) cultured-meats [231], b) nutritious crops [232, 233, 234, 235], and c) biofuel-producing microorganisms [236]; and bioremediation, through elucidating the involvement of microbes [237].

Other sub-cellular systems, besides the metabolome, are included in WCMs: notably, the genome and the proteome. The genome, for example, begets the proteome, which in turn contributes $\frac{1}{3}$ of cellular mass [238] and governs the metabolome through enzymatic catalysis. The transcription and translation processes between the genome and proteome are collectively termed the Central Dogma of biology

$$\text{DNA} \xrightarrow{\text{transcription}} \text{RNA} \xrightarrow{\text{translation}} \text{proteins} \; . \tag{3.4}$$

The Central Dogma can be specified in simple models to occur at experimentally-determined rates,

while more intricate models of epigenetics, for example, may require more complex representations of the Central Dogma to ensure that homeostasis is maintained during a simulation [239].

3.1.1 Biofilm models

A novel and aspirational application of WCMs is to simulate entire colonies of bacteria. Bacterial colonies (biofilms) [240, 241] are an interesting subject of study since they cause persistent infections [242, 243, 244, 245, 246, 247, 248, 249, 250, 251], and degrade industrial surfaces [27, 252, 253], such as boat hulls [254, 255, 256, 257]. Biofilms are additionally resistant to antimicrobial agents [258] as the consequence of a) inter-species cohabitation [259], which diversifies cellular vulnerabilities; b) limited diffusion through the polymeric biofilm matrix [260, 261, 262, 263, 264], which hinders liquid-state antibiotic treatments; and c) lower metabolic activity [265, 266, 267], which limits antibiotic absorption.

Models of biofilm systems are empirical approximations of the underlying biochemical processes processes[268, 269, 270, 271, 272]. The Rittmann model [273], for example, simplified biofilm growth to one-dimension, ignored extracellular polymeric substances, and, like many early biological models [274, 275], employed Monod kinetics to represent cytosolic chemistry. Improvements upon these early models [276, 277] has manifested in more sophisticated algorithms for representing biofilm systems. Two prominent examples are the cellular-automaton (CA) algorithm, which simulates a spatial lattice and uses deterministic rules of biochemistry, and the individual-based growth model (IbM), which represents biofilms as ecosystems of individual cells in a contiguous space [278] and uses stochastic rules of biochemistry. Contemporary biofilm models [279, 280] – e.g. the digital biofilm model [281] and the Unified Multiple-Component Cellular Automaton model [282], amongst others [283, 284] – iteratively approach a mechanistic framework of biofilm biochemistry, which remains the frontier of biofilm models [285].

The amalgamation of WCMs with models of extracellular processes [286, 287, 288, 289, 290] would provide a mechanistic biofilm model with unparalleled biochemical resolution. This synergy would elucidate details – e.g. effects of antibiotics [273] or reactive oxygen species [291] – that can accelerate experimental research to combat problematic biofilms. The remaining challenges to realize this conceptual synergy are two-fold: 1) the computational expense of simultaneously simulating $\approx 1E3$ complete WCMs, one for each simulated cell in the biofilm, is untenable for personal computers; and 2) the quantity of experimental data that is needed to thoroughly parameterize each variable of each process in each cellular and intercellular system is a formidable bioinformatics bottleneck, which requires assembling and organizing bulk amounts of experimental data and which is unfortunately exacerbated by limited programmatic access to biochemical databases.

3.1.2 WCMpy suite

We, therefore, developed a suite of Python modules – inspired by the modularity of the Edinburgh Genome Foundry suite of packages [292] for synthetic biology – that address each of the aforementioned

challenges that impede applying WCMs in a biofilm model. 1) The first challenge of computational expense is addressed by condensing the WCM into its essence – being the metabolome and the Central Dogma – with lightweight Python modules: dFBApy and Codons, respectively. The Codons module is distinguished from the only Python module of the Central Dogma ("Dogma") by i) providing extended functionality – e.g. generating and searching FASTA files in BLAST (Basic Local Alignment Search Tool), similar to other packages [293] – and ii) providing more documentation and a more intuitive application programming interface (API) that facilitate its usage. The dFBApy module is distinguished from the only other dFBA module for Python ("dFBA") by being i) amenable with Windows OS, which greatly expands its accessibility [294]; ii) lightweight for large-scale simulations; and iii) compatible with the other modules within our ecosystem. 2) The second challenge of bioinformatics processing is addressed through the BiGG_SABIO module, which we developed to bootstrap programmatic access with the SABIO reaction kinetics (SABIO-RK) database [295] – the most curated source of biochemical kinetics data, versus alternatives like the BRENDA database [296] – and then to refine the assembled data into a form that is directly amenable with the dFBApy package.

The aforementioned scripts – Codons, dFBApy, and BiGG_SABIO – are designed to be amalgamated into a Python WCM package, e.g. WCMpy, which would be to our knowledge the first attempt i) to assemble a WCM in Python (the most popular programming language [297]) and ii) to simplify the WCM framework for community-level simulations, notwithstanding prior work in assessing biofilm antimicrobial efficacy via FBA [298]. We believe that these lightweight and open-source packages offer unique resources for developers to crowd-source simpler and more accessible WCMs that can scale to multicellular studies, which is complementary to increasingly fundamental WCMs [299] elsewhere in the WCM community [300, 301].

3.2 Methods

The logic and calculations for each of the aforementioned packages are separately detailed in the following sections.

3.2.1 BiGG_SABIO

The BiGG_SABIO Python module first loads a (JSON) GEM model with the syntax of the BiGG models repository (the standard repository for GEMs) [302]. The module is organized into two distinct processes and functions. The first function `scrape_bigg_xls` a) parses the loaded model to determine all of its reactions and their database annotations; b) systematically searches each database annotation of each reaction, in addition to the reaction/enzyme name, in the SABIO-RK database via a Selenium Firefox webdriver [303, 304] that navigates the webpage and retrieves data from iframes; c) downloads all of the search results in a local folder in the directory of the parameterized BiGG model; d) concatenates the complete set of XLS files, after the downloading has concluded, into a single CSV file; and e) scrapes

and downloads the names and values for each rate law variable of the CSV file into a JSON file. These processes require an extensive amount of time; hence, this first function tracks its progress and can be stopped and resumed at any point. The second function of BiGG_SABIO `to_fba` processes and refines the downloaded CSV and JSON content into a single JSON file that is amenable with dFBApy, which contains both the essential rate law information and the related provenance to ensure transparency and reproducibility of simulation parameters.

3.2.2 dFBApy

The dFBApy package simulates dFBA of a BiGG-formatted GEM, as an API wrapper for the COBRApy (Constraint-Based Reaction Algorithm in Python) FBA module [305, 306]. The dFBApy module operates through a series of steps. 1) Simulation details are parameterized – e.g. the total simulation time, the timestep value, a (XML) GEM, and a JSON file of kinetic data – which can be sourced from BiGG_SABIO or customized elsewhere. 2) The parsed parameters are substituted into the available rate laws. 3) The `simulate` function cycles through eqs. (3.2) and (3.3) of the chemical system and updates a Pandas DataFrame [132] of all chemical concentrations after each timestep. The conversion of fluxes into concentration changes necessitates the cellular dry mass and the cellular volume of the simulated organism, which we estimate to be $0.2pg$ [307] and $1fL$ [191] for bacteria, respectively, although these can be parameterized by the user. 4) Concentration changes are graphically visualized via MatPlotLib [131], and data of the fluxes and concentrations can be exported with the figure to a local folder.

3.2.3 Codons

The Codons Python module conducts simple manipulations and analyses of a genetic sequence and its corresponding proteins: notably transcription and translation of the Central Dogma. The modular functions of Codons first accept a genetic sequence as either a string or a FASTA-formatted file [308] (the standard format for genetic and protein sequences, where a sequence is preceded by a description line: e.g.

```
>Protein_-_35_residues_-_4796.5_amu
```

that is denoted by a leading ">"). The `transcribe` function conducts transcription with a regular expression [309] that simply exchanges all thymines (T's) with uracils (U's), or visa versa. The `translate` function conducts translation according to the investigator's specifications, which optionally includes translating a) all possibly proteins, b) the complementary sense strand, and c) all three possible reading frames. The function operates by 1) determining the location of start codons, which can be tailored by the investigator; 2) grouping nucleotides into sets of three (codons); 3) translating the codons into corresponding amino acids per the Standard Codons Table, which can be tailored by the investigator to accommodate species variability; and 4) terminate the protein when a stop codon

is reached. The Codons module further supports searching genetic and protein sequences through the NCBI BLAST database [310, 311] via the "BioPython" module [312], which acquires and downloads information about the parameterized sequence, or its proteins, and therefore assists in identifying homologues, functionality, and pertinent literature. The Codons module can finally create and export FASTA files from any parameterized genetic or protein sequence into a local folder.

3.2.4 WCMpy

The aforementioned Python modules, or their core logic, may be aggregated into a single module (WCMpy) that follows the workflow of Figure 3.1. The Central Dogma would be conducted via Codons and can be parameterized to occur at fixed rates of $70\frac{nucleotides}{second}$ [313, 314] and $\left(\frac{5\frac{amino\ acids}{second}}{1.31\frac{doublings}{hour}}\right)$ [315], respectively, where the latter rate is a function of the doubling time of the simulated bacteria. Protein degradation can be calculated with half-life probabilities ($\%\ remaining = 100 * \left(\frac{1}{2}\right)^{\frac{\text{time}}{\text{halflife}}}$) where protein half-lives are determined by the N-end rule [316] in which the N-terminus residue of a protein dictates its degradation rate as being either 2 *minutes* or $>$ 10 *hours*. Translation and transcription in WCMpy would furthermore be limited by the cytoplasmic concentrations of amino acids and nucleotides, which connects to the metabolic activity that would be calculated via dFBApy (an alternative approach of simulating metabolism, based in thermodynamics, is proposed in the Supporting Information). The input file of kinetics rate laws for dFBApy in this workflow would ideally be sourced from BiGG_SABIO. The extracellular concentrations, e.g. Lysogeny broth (LB) [317] that is approximated as degraded casein protein [318] and yeast extract [319], may be user-specified in addition to the presence of antibiotics. The cellular mass, volumetric growth, and ultimately binary fission [320] (which we would presume to occur at a fixed rate like other WCMs [239]) would be dependent upon the cytoplasmic concentrations at the end of a timestep, after the biochemical processes have occurred. The high-dimensional simulation results may finally be best communicated through visualizations of the cell or biofilm that complement the molecular-level data from the underlying dFBApy and Codons packages.

3.3 Case studies

We separately exemplify core functionality of the WCMpy workflow – being the BiGG_SABIO, dFBApy, and Codons modules – in the following sections, which are available as Python Notebooks in the respective GitHub repositories.

3.3.1 BiGG_SABIO & dFBApy

The BiGG *E. coli* core model consists only of the 95 essential metabolic reactions for *E. coli*. This model was first loaded into the BiGG_SABIO module, where the `parse_data` function systematically

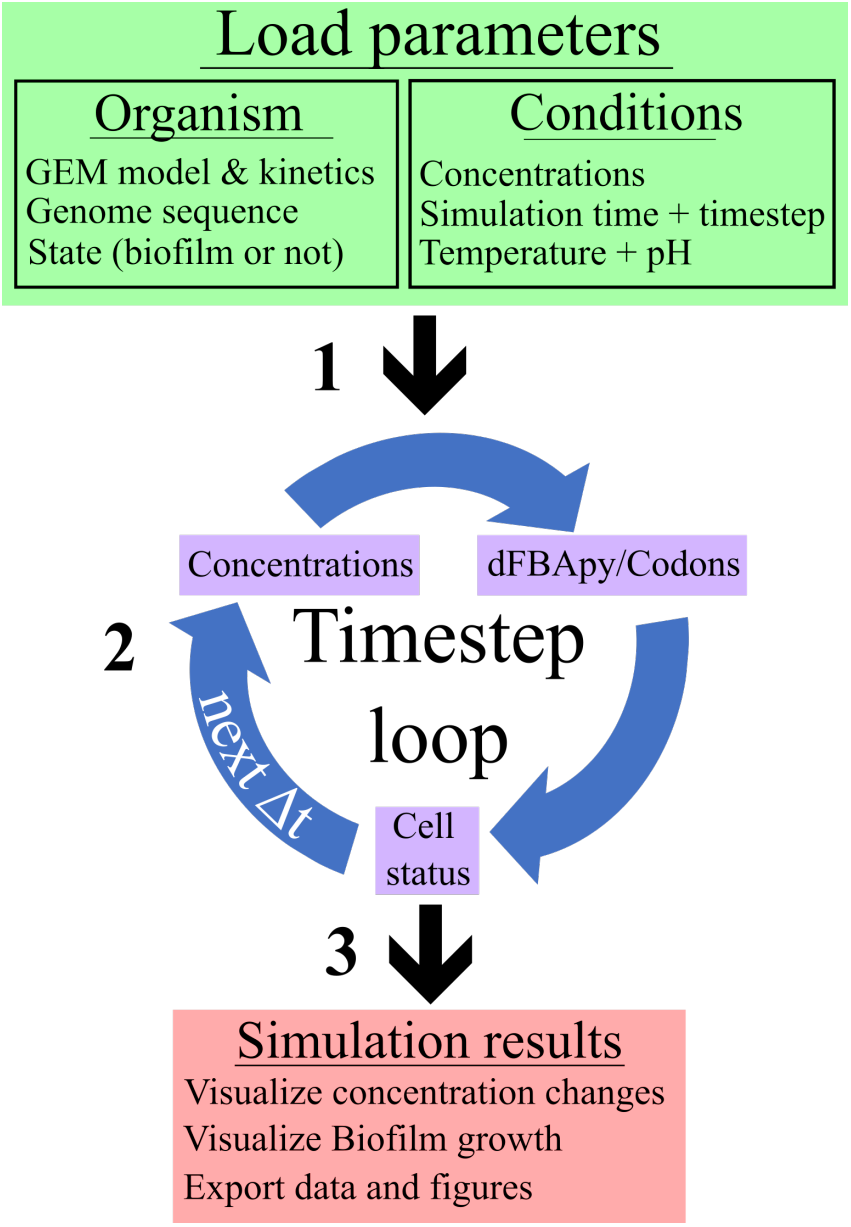

Figure 3.1: The stepwise workflow of WCMpy. **Step 1** describes parameterizing the WCMpy simulation with information about the organism (e.g. the representative GEM and corresponding kinetics rate laws, the genome sequence, and the organismal state as either planktonic or sessile) and the simulation conditions (e.g. initial concentrations of the cytoplasm, the simulated time and timestep, and environmental conditions of the system). **Step 2** describes the loop that occurs with each timestep: a) dFBA and the Central Dogma are conducted based upon previous concentrations; b) the statuses of each cell and biofilm component are calculated; and c) the concentrations are updated by the reaction flux for the next timestep. **Step 3** describes processing, visualizing, and exporting the simulation results.

acquired all of the data ($\approx 185MB$) that describes the reactions of this model. The `to_fba` function then refined the raw data into a manageable file of kinetics data that was then directly parameterized into dFBApy and executed for an arbitrary amount of time. The results of this simulation are illustrated in Figure 3.2a, where the metabolic system re-establishes an equilibrium after the metabolism is perturbed by initial concentrations and rate law fluxes. The plotted concentrations for chemicals with defined initial concentrations are absolute concentrations, while those for chemicals without initial concentrations are only relative concentrations to the unknown initial concentration and are tagged with "(rel)" in the legend. The ability to alternatively parameterize kinetics data as an argument to the `simulate` dFBApy function was demonstrated in Figure 3.2b by specifying only Acetate Kinase kinetic information from the full kinetic file of Figure 3.2a.

3.3.2 Codons

The Central Dogma of the WC082 strain of Vancomycin-resistant *S. aureus* [321], sourced from the National Center of Biotechnology Information [322], was simulated through Codons. Between $[25, 32]\%$ of the reported proteins, and $[65, 83]\%$ of the reported peptide sequences, were perfectly translated from the 3 Mb genome – depending upon which start codons were selected, how many open reading frames (ORFs) were translated, and whether the sense strand was translated. The translation of every possible protein, which accounts for overprinted genes, improved the accuracy to matching 41% of proteins and 99.5% of peptide sequences. Discrepancy between matches of entire proteins yet near 100% matches of all peptide sequences supports that many bacterial proteins may be assembled from numerous peptides. Improvements in accuracy consequently increase a) the run time, from $1min$ to $28min$, and b) the proportion of false predictions, from 87% to 97%, for one ORF with no sense strand and for every possible protein on both strands, respectively.

The aforementioned example with *S. aureus* were contrasted with an example of the MERS (Middle-Eastern Respiratory Syndrome, $\approx 29kb$) virus [323]. Slightly more of the reported proteins $\left(\frac{20}{30}\right)$ perfectly matched the translated proteins when considering all three ORFs, and 100% of the reported proteins were perfectly translated when accounting for overprinted genes that are more common in viruses [207], which suggests that viruses infrequently engage in peptide assembly into proteins. The sequences of the genome and the set of translated proteins were searched in the BLAST database through Codons, which were identified with 100% certainty except for the small, ambiguous, peptides that are difficult to identify.

3.4 Discussion

The developed suite of Python packages contributes modular tools that we postulate will foster the development of a mechanistic biofilm model, based upon a scalable WCM: WCMpy. The open-source Python community encourages collaboration, which may be particularly valuable for comprehensive

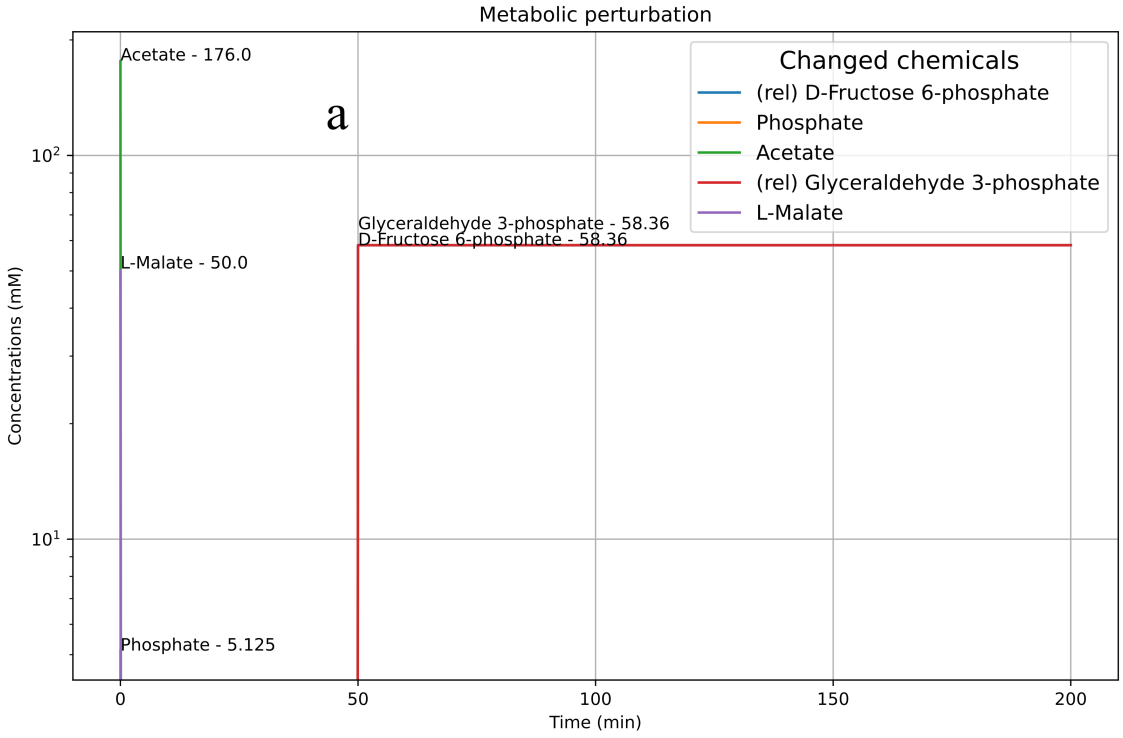

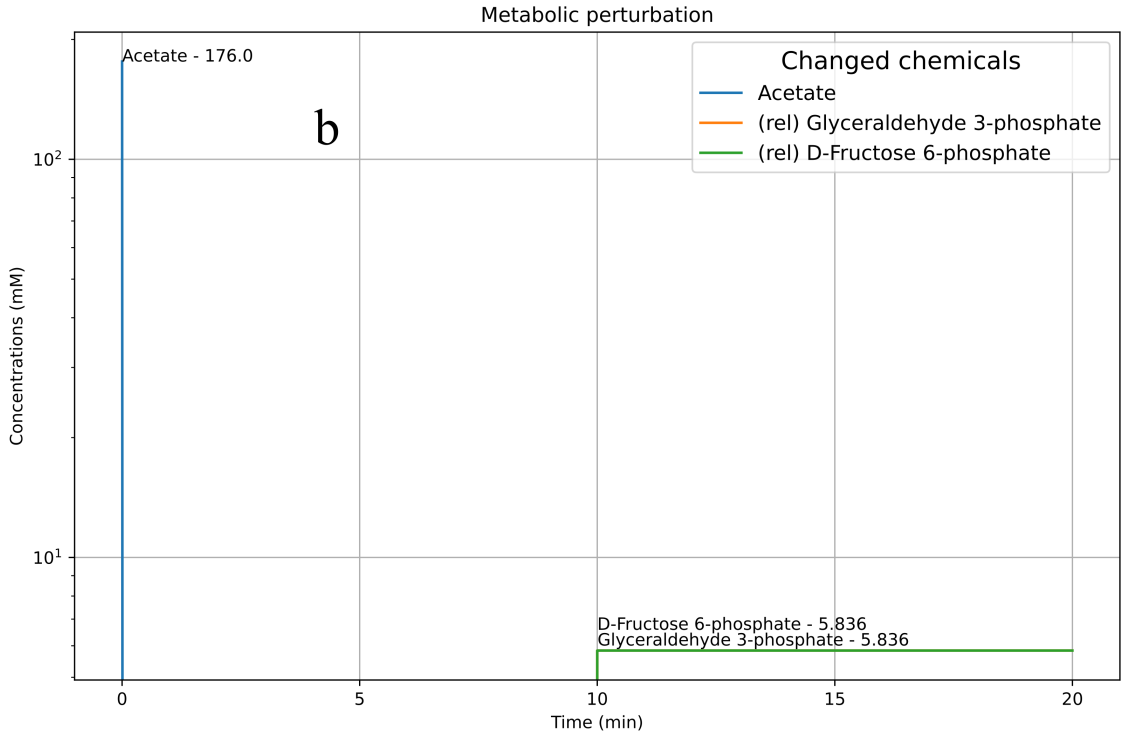

Figure 3.2: Notable concentration changes from simulating the *E. coli* core BiGG model via dFBApy with a) full SABIO-RK kinetics data via the BiGG_SABIO module and b) a single entry from the kinetics data that was passed as a function argument. Chemicals with defined initial concentrations are depicted at $t = 0$, while other chemicals are labeled as relative changes "(rel)" since their initial concentrations are unknown. The metabolic consequences of these concentrations and calculated fluxes are observed over the first timestep, where equilibrium is re-established by generating D-Xylulose 5-phosphate and Alpha-D-Ribose 5 phosphate. The discrete establishment of equilibrium is the consequence of a "stiff" FBA algorithm.

projects such as WCMpy. The metabolome modules – BiGG_SABIO and dFBApy – provide a conduit between a kinetics database and dFBA metabolic simulations for any organism whose metabolism is encapsulated in a BiGG-formatted GEM. These metabolic packages may individually useful to the DataNator [324] and ModelSEED [325] WCM projects that are developing an improved bioinformatics resource and modelling tools, respectively. The dFBApy simulations are quantitatively consistent between the metabolic production in Figures 3.2a-b and the relative carbon input, which encourages their continued use by the community. The Codons module offers a rapid, intuitive, and practical tool for simulating the Central Dogma and investigating the genome and proteome of any organism with a known genetic sequence. These three packages advance available techniques to alleviate the noted bottlenecks – scalable code and bioinformatics logistics – that hinder developing mechanistic biofilm models with fundamental WCMs, which could expedite research in understanding and managing biofilms.

3.5 Author Contributions

1. **APF** - Writing and research
2. **ESC** - Writing and research
3. **HLB** - Writing, guidance, and funding

3.6 Acknowledgments

The authors thank Jonathan R. Karr for his pioneering work in developing WCMs, and for providing guidance through our journey in systems biology.

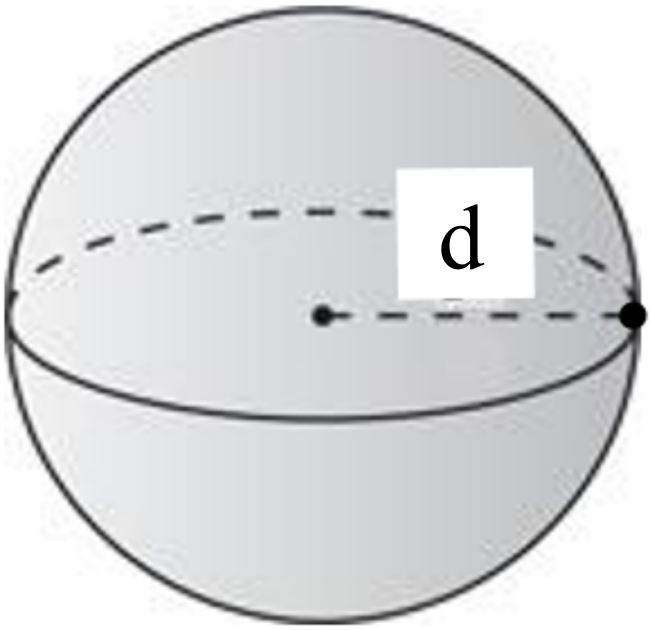

Figure S1: A sphere where the surface area represents the location of a chemical after a timestep, which begins at the origin of the sphere, while possessing the average root-mean-squared velocity of extracellular chemicals.

3.7 Supporting Information

3.7.1 "dFBA" module

We attempted to repurpose the "dFBA" module into a scalable and more accessible module for Windows OS. This was inhibited by the "dfba_utils.so" file, and our attempt to replace this file with a dynamic linked library (DLL) analogue was thwarted by incompatibilities between C code in the library dependencies such as NVectors, SUNDIALS, and dlfcn and the C++ code of the DLL file. A further complication was that a few of these libraries, such as SUNDIALS, dynamically created the header files depending upon the user's operating system; thus, a distinct DLL file would be required for each possible user architecture, which is not practical. The dFBApy module was therefore developed.

3.7.2 Thermodynamic metabolism

We considered conducting metabolism for WCMpy via thermodynamic gradients, rather than conventional dFBA kinetics. This proposed logic is incomplete, since we migrated to the kinetic models during its development; however, the preliminary logic and calculations of the following sub-sections may still inspire the development of a thermodynamic metabolic approach.

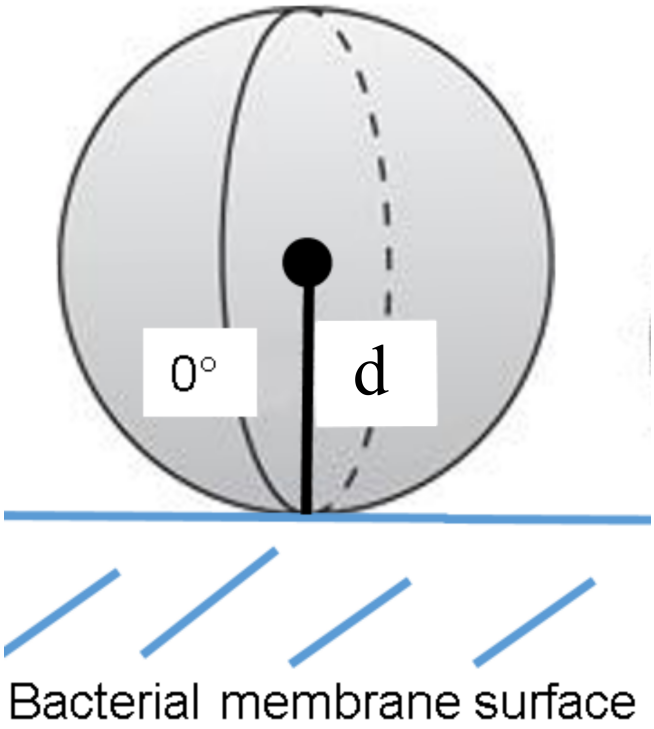

(a) The maximal distance (d) from the bacterial membrane where a chemical can still contact the membrane with a timestep. This distance defines the thickness of the volume shell around the bacterial membrane within which chemicals may potentially be absorbed in a timestep.

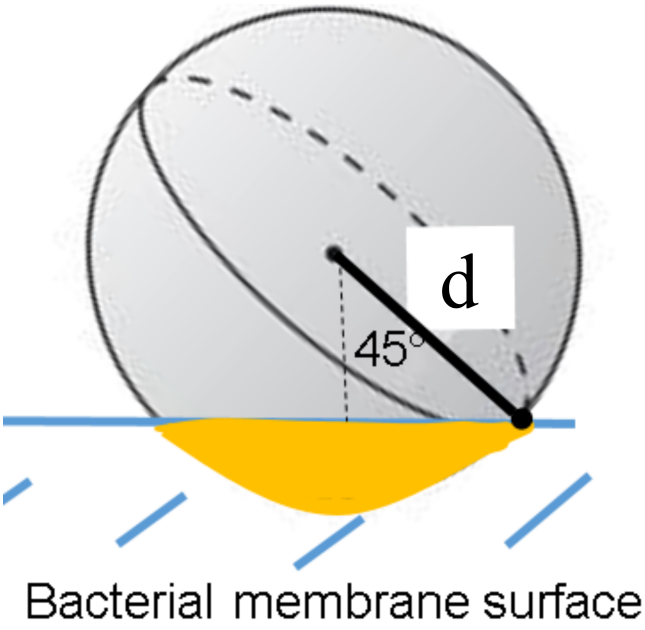

(b) The average distance ($d * cos(45°)$) from the bacterial membrane where a chemical can still contact the membrane with a timestep. The proportion of the orange surface area and the total surface area in eq. (S5) represents the probability of that a chemical within the volume shell around bacterial membrane strikes the membrane in a timestep.

Figure S2: Distances from the bacterial membrane where an extracellular chemical can still contact the membrane within the timestep, given a known velocity.

Membrane absorption

Cellular absorption is determined by the cellular dimensions, which are calculated with each timestep. The bacterial shape is assumed to be spherical, which facilitates calculating cellular volume and surface area as a function of cellular mass m, via a constant density, with each timestep Δt. The quantity of absorbed chemicals is calculated as a fraction of the chemicals that exist within a distance d from the bacterial membrane,

$$d = \vec{V}_{rms} * \Delta t \ . \tag{S1}$$

This is the distance that a chemical, with the average root-mean-squared velocity of an extracellular chemical

$$\vec{V}_{rms} = \sqrt{\frac{3 * k_B * T}{m_{ave}}} \ , \tag{S2}$$

travels in Δt, where k_B is the Boltzmann constant; T is the extracellular temperature in kelvins; and m_{ave} is the average mass of the extracellular chemicals. The distribution of potential locations for a chemical after Δt is conceptually represented as a sphere in Figure S1, where the origin is the initial location of the chemical and the sphere surface, a d distance from its origin, represents the set of possible final locations. The volumetric shell of d thickness around the bacterial membrane is the volume wherein chemicals could potentially collide with the membrane and be absorbed, which is calculated

$$V_{shell} = \frac{4\pi}{3} * ((r_{cell} + d)^3 - r_{cell}^3) \tag{S3}$$

where r_{cell} is the cellular radius at the start of Δt. The product of V_{shell} and the extracellular chemical concentration C_i of chemical i

$$n_{shell,i} = C_i * V_{shell} \tag{S4}$$

yields the $n_{shell,i}$ quantity of chemical i that may be potentially absorbed. The proportion P of $n_{shell,i}$ that will contact the membrane is calculated as the proportion of spherical surface area in Figure S2b that overlaps with the membrane

$$P = \frac{SA_{membrane\ collisions}}{SA_{sphere\ of\ possibilities}} = \frac{2 * \pi * r_{distance\ traveled} * (r_{distance\ traveled} * cos(contact\_angle))}{4 * \pi * r^2_{distance\ traveled}} = \frac{(cos(45°))}{2} = 14.6\% \tag{S5}$$

The numerator is mathematically represented as the surface area of a conic sector of the chemical location sphere. The *contact_angle* of 45°, between the extracellular chemical and the bacterial membrane, is the average between the maximal angle of 90° for the infinitesimally close chemical to the membrane and the minimal angle of 0° for the farthest possible chemical, which is illustrated in Figure S2a. The P value of eq. (S5) is importantly independent and constant.

The fraction of incident P chemicals that are absorbed is approximated by the thermodynamic gradient of each chemical i, which we propose represents the metabolic need E_i of that chemical. The thermodynamic gradient is determined as the current displacement $\Pi_{R=1}^{x}(\frac{Q_R}{K_{eq,R}})$ – for the x number of

R reactions in which chemical i is a reactant – from the optimum displacement

$$\left(\frac{Q}{K_{eq}}\right)_{optimum,i} = e^{\frac{\eta * n_{e^-,i} * F * E_{potential}}{R * T_{incubation}}} \tag{S6}$$

where η is the total quantity of reactions in the bacterial membrane; $n_{e^-,i}$ is the average quantity of exchanged electrons in reactions where chemical i is a reactant; F is Faraday's constant of electrical charge; $E_{potential}$ is the electrical potential of the bacterial membrane; R is the gas constant; and $T_{incubation}$ is the incubation temperature of the simulated organism, which we presume to be indicative of the optimal thermodynamic displacement for the organism's biochemistry. The metabolic need

$$E_i = \begin{cases} 0, & \text{if } \left(\frac{Q}{K_{eq}}\right)_{optimum,i} < \Pi_{R=1}^{x}\left(\frac{Q_R}{K_{eq,R}}\right) \\ \left(\frac{Q}{K_{eq}}\right)_{optimum,i} - \Pi_{R=1}^{x}\left(\frac{Q_R}{K_{eq,R}}\right), & \text{else} \end{cases} \tag{S7}$$

is constrained to be positive, which assumes that excessive chemicals are not jettison. The absorbed quantity of chemical i

$$n_{absorbed,i} = E_i * n_i * P * B_i \ , \tag{S8}$$

is finally the product of its metabolic need (E_i from eq. (S7)), its quantity within the volume shell (n_i from eqs. (S3) and (S4)), the probability of it striking the membrane (P from eq. (S5)), and finally absorption hindrances that are encapsulated in B_i to abstractly represent transport phenomena at the membrane that may discriminately treat different chemicals. The contribution of absorption to mass growth of the cell is calculated

$$\frac{\Delta m}{\Delta t} = \sum_{i=1}^{b}(n_{absorbed,i} * MW_i - n_{ejected\ waste,i} * MW_i) \tag{S9}$$

as the sum-product of the quantity of all absorbed or disposed b chemicals in the metabolism and their respective molecular weights. The aggregate change in the cellular mass $\frac{\Delta m}{\Delta t}$ from eq. (S9) begets cellular dimensions

$$r_{cell} = \left(\frac{3 * \frac{m}{\delta_{cell}}}{4 * \pi}\right)^{\frac{1}{3}} \ , \tag{S10}$$

assuming a constant density (δ_{cell}).

Chemical reactions

Metabolic reactions are partitioned between the cytoplasm (c), the membrane (m), and the extracellular environment (e). The maximal possible quantity of chemical reactions that can proceed in the forward or backward directions is calculated $R_{max} = \left|\frac{C_i}{s}\right|$, where C_i is the concentration of chemical i and s

is the stoichiometry of chemical i in reaction R. The maximal R_{max} reaction progressions in a Δt is attenuated $R_{actual} = R_{max} * \zeta$ by a scalar ζ that represents unreactive collisions and diffusion limitations [326]. The R_{actual} is further limited $R_{actual} = \begin{cases} R_{actual}, & if\ R_{actual} < e \\ e, & else \end{cases}$ by the quantity of enzymes that can catalyze the reaction e. The direction of the R_{actual} reactions is determined $NF = K_{eq} - Q$ by the relative difference between the current Q and optimal K_{eq} thermodynamic values, where $NF > 0$ denotes forward reactions and $NF < 0$ denotes backward reactions. The concentration change C_i – in each separate compartment – over the timestep for chemical i is calculated $\frac{dC_i}{dt} = R_{actual} * s$ as the product of the quantity of reaction progressions and the respective stoichiometry of the chemical in the reaction. The new C_i is crucially used in eq. (S7) to determine the metabolic need of the chemical in the system.

Chapter 4

A kinetic model of Photodynamic Inactivation: PDIpy

4.1 Introduction

Antibiotic resistant infections are projected to exceed cancer in annual deaths, and cost 10^{13} USD per year globally by mid-21st century [42]. Methicillin-resistant *Staphylococcus aureus* (MRSA) [327, 328, 329] and fluoroquinolone-resistant *Salmonella* [330] are two worrisome examples of virulent pathogens that are developing resistance to the antibiotics that subdued them half of a century ago. Antimicrobial resistance (AMR) evolution can be slowed by reducing excessive and incomplete use of antibiotics for human illness and animal agriculture (which is globally the primary consumer of antibiotics [331, 332]); however, AMR is the inevitable consequence of specific mechanisms of action with conventional antibiotics: e.g. β-lactam antibiotics selectively target the Penicillin binding protein [333]. Highly selective antibiotics are advantageous for mitigating off-target effects, yet, this strategy applies a strong evolutionary pressure on the pathogen to fortify the targeted vulnerability and thus circumvent the treatment mechanism. The perpetual arms race of medicinal chemists against microbial evolution, which ensues from this antibioic strategy of specific treatment mechanisms, must be replaced with a more sustainable strategy.

4.1.1 Photodynamic inactivation

Photodynamic inactivation (PDI) offers an effective medical technique for killing pathogens: e.g. bacteria [334] and viruses [335, 336]. PDI is a photochemical process that generates singlet state oxygen ($^1\Delta_g$) [337, 338, 339, 340, 341] – a reactive oxygen species (ROS) [342, 343] – which non-selectively oxidizes biological substrates [344, 345] to the point of death. This mechanism enables PDI to a) avoid resistance evolution [346, 347, 348], because oxidation from $^1\Delta_g$ is too intense and rapid for adaptation of survivors; b) treat recalcitrant biofilms [349], where, unlike conventional antibiotics, the extracellular polymeric substances (EPS) of the protective biofilm matrix is oxidized concomitantly with the targeted

cells [350] and thus the mechanism of action is not diffusion-limited; and c) minimize off-target effects, since $^1\Delta_g$ has high spatiotemporal localization [351, 352, 353]. The last quality enables the use of PDI in cancer treatment [354], open systems such as wastewater [355, 356, 357], hospital surfaces [358], industrial polymers [359], and directly on agricultural products [360, 361], where $^1\Delta_g$ won't leach into the environment [39, 362, 41] or human consumables.

The excited singlet state $^1\Delta_g$ oxygen is distinguished from the ground triplet state ($^3\Sigma_g^-$) oxygen [363] by its quantum numbers. The molecular singlet state contains only paired electrons – i.e. one up spin electron for each down spin electron – and is named after its multiplicity (m) [364] of 1: from

$$m = 2(S) + 1 \tag{4.1}$$

when $S = 0$. S is the total angular momentum of the molecule – the sum of electron spins, where up is $+\frac{1}{2}$ and down is $-\frac{1}{2}$ – which, for a singlet molecule, is 0 since complete pairing necessitates equal quantities of up and down electrons (Figure S1). The molecular triplet state, in contrast, contains two unpaired electrons that result in a multiplicity of 3 from $S = 1$ in eq. (4.1). These unpaired electrons in $^3\Sigma_g^-$ increase shielding of the nuclear charges [365] and consequently stabilize $^3\Sigma_g^-$ by 0.98 eV [366] relative to $^1\Delta_g$ that lacks this shielding. The latin symbols for these molecular states derive from the $^m\Lambda_{g/u}^{+/-}$ template of molecular information, where g/u – gerade (non-invertable) & ungerade (invertable) – denotes the invertability of the molecule with respect to an inversion center and $+/-$ denotes symmetry or anti-symmetry of the molecule, respectively. The base Λ term describes the orbital angular momentum of the molecule, which is distinct from the total angular momentum S by differentially weighting sub-orbitals, while following Hund's 2nd rule of distributing electrons amongst degenerate sub-orbitals to maximize the orbital angular momentum.

PDI consists of a few steps. First, the ground singlet state photosensitizer (PS) catalyst (^1PS) photonically excites $^1\text{PS} \xrightarrow{h\nu} {}^1\text{PS}^*$ following the formal selection rules of electronic excitation [367], where it likely excitations preserve the electronic spin state: e.g. singlet to singlet. Second, the excited $^1\text{PS}^*$ then relaxes through intersystem crossing, instead of fluorescing [368], to a more stable triplet state (^3PS),

$$^1\text{PS} \underset{\text{fluorescence}}{\overset{\text{excitation}}{\rightleftharpoons}} {}^1\text{PS}^* \xrightarrow{\text{intersystem-crossing}} {}^3\text{PS} \tag{4.2}$$

that transfers energy to $^3\Sigma_g^-$, instead of phosphorescence [369], to generate $^1\Delta_g$ while regenerating the ground-state ^{1}PS catalyst,

$$^1\,\text{PS} \xleftarrow{\text{phosphorescence}} {}^3\,\text{PS} \xrightarrow{^3\Sigma_g{}^-} {}^1\,\text{PS} + {}^1\Delta_g\ . \tag{4.3}$$

The ^{3}PS and $^1\Delta_g$ excited states engage in energy transfers instead of $^1\text{PS}^*$ and $^3\Sigma_u{}^+$ since the former have longer lifetimes as a consequence of fluorescence being more favorable than phosphorescence. Finally, the $^1\Delta_g$ from eq. (4.3) oxidizes biological substrates through Type II oxidation mechanisms, which are concerted Schenck [370] or ene [371] reactions that produce organic peroxides [372], rather than Type I

mechanisms [373, 374, 375] that only affect radical substrates [376]. The Type II mechanism importantly oxidizes both saturated and unsaturated fatty acid chains, which comprise membrane phospholipids [377].

Photosensitizer

The PS is the essential component of PDI. The PS advantageously a) introduces control in the timing, magnitude, and location of $^1\Delta_g$ generation, as a counter-balance to the non-selective mechanism of action; and b) generates antimicrobial concentrations of $^1\Delta_g$ that would not occur by direct excitation of ambient oxygen from a photon ($h\nu$) $^3\Sigma_g{}^- \xrightarrow{\text{hv}} {}^1\Delta_g$ [378], since this excitation is spin forbidden. Indirect photonic excitation can generate $^1\Delta_g$ $\left({}^3\Sigma_g{}^- \xrightarrow{\text{hv}} {}^3\Sigma_u{}^+ \xrightarrow{\text{intersystem crossing}} {}^1\Delta_g + \text{energy}\right)$ [379], nevertheless, the PS catalyst accelerates and augments $^3\Delta_g^-$ generation [380, 381, 366]. The efficiency of a PS is defined by its quantum yield ($0 \leq \Phi_\Delta \leq 1$; $\frac{^1\Delta_g \ molecules \ produced}{photon \ absorbed}$), which encapsulates the probably of eqs. (4.2) and (4.3) [382]. The Φ_Δ is inversely proportional with the likelihood of fluorescence and phosphorescence relaxations, in Figure S3, and photobleaching, where photons and/or $^1\Delta_g$ irreversibly compromise molecular absorptivity [383, 384]

The chemical structure of PS, in addition to the environmental conditions [385, 386], is a primary influence on Φ_Δ. The molecular functionality and charge, for example, can a) optimize its association with the targeted cells [387, 388], which optimizes efficacy while minimizing off-target oxidation [389] and host toxicities [390]; and b) possibly be amenable to permanent surface attachment [391] while retaining material properties [358] in material applications of PDI [392, 393]. The PS molecular properties further determine which biological substrates are oxidized. PSs that are impermeable to the cytoplasmic membrane, or are bound to a material surface, generally oxidize the cytoplasmic membrane [394, 395] in Figure S4 instead of cytoplasmic contents [396], which causes lysis [397, 398] and generally affects gram-positive bacteria more than gram-negative bacteria [347, 399] since the latter possess a superficial lipopolysaccharide layer that protects the cytoplasmic membrane. Permeable PSs, by contrast, can generate $^1\Delta_g$ within the cytoplasm and thus cytoplasmic chemicals [400] such as guanine nucleotides [401, 402] are fatally oxidized, which is more effective with prokaryotes than eukaryotes [390] since the latter have a nuclear membrane that protects DNA, particularly guanine, from oxidation [403].

The most efficacious PS in nature is chlorophyll [404], which is an organometallic porphyrinoid (Figure S2) that evolution has tuned for low rates of photobleaching and absorption of visible light – specifically blue-violet [405] via the Soret absorption band [406, 407, 408, 409, 410, 411, 412] and green-orange [413] via the Q absorption band [414, 415, 416, 417]. Chlorophyll, however, has not evolved molecular functionality that optimizes its efficacy in PDI systems; therefore, synthetic porphyrins [418, 350, 419] that emulate the efficient conjugated structure [420] of chlorophyll, yet introduce other metal centers [421] and functional handles [422, 423, 424] (e.g. Figure S2) that improve its utility for PDI [425, 426, 427] – such as enabling surface attachment, possessing a desirable charge or permeability, or perhaps being tuned for a specific wavelength – are an appealing direction for PDI research.

4.1.2 PDI modeling

Mechanistic models of PDI systems – that capture the chemistry and physiology of PDI – are unfortunately scarce and insufficiently comprehensive. The most prevalent form of PDI models is the logistic survival curve [428, 429, 430, 431, 432]

$$log\left(\frac{N(t)}{N_0}\right) = N_r\left(1 - \frac{1}{1 + \left(\frac{t}{\tau}\right)^P}\right) \tag{4.4}$$

where N_0 and N are the number of organisms at times zero and t, respectively; N_r is the number of resistant organisms to the treatment method; P is the length of the shoulder curve in the sigmoidal plot; and τ is the suddenness at which inactivation occurs. Brasel et al. [433] applied eq. (4.4) – with third-order polynomials that describe N_r, τ, and P as a functions of irradiation intensity $\frac{mW}{cm^2}$ and exposure time – however, the few variable conditions of this logistic model do not permit the investigator to explore the space of possible PDI systems: e.g. variability in the emission spectra of the light source [434], the biochemical profile of the targeted organism, or the efficacy of the simulated PS. Santos et al. [435] offered a response surface model of empirical second-order polynomials to determine inactivation as a function of PS concentration and irradiation time; however, the calibration of this model for a single PS (Eosin Y) and LED light source hinders its applicability to the numerous other combinations in effective PDI systems.

We therefore developed a holistic PDI model that can guide biologists and chemists through the design of optimal systems and PSs, respectively. This model captures the processes of Figure 4.1 through a series of reactions that represent a) the photoexcitation of the photosensitizer; b) the relay of excitation energy to ambient oxygen to form $^1\Delta_g$; c) the oxidation of biological material until lysis; and d) continuous growth of the simulated species. Notable variables in our model include: chemical constituency of the cytoplasmic membrane; concentration and absorptivity of the photosensitizer; emission spectra and intensity of the light source; and dimensions of the simulated space. This model constructs a kinetic rate law, from literature measurements, for each of these processes and parameterizes the aforementioned variables. The model yields predictions of membrane oxidation that are converted into predictions of inactivation through a calibrated parameter – which is the threshold of membrane oxidation that causes lysis – that derives from training our model with published PDI data. This model is moreover encapsulated into a Python API (PDIpy) in Figure 4.2, which allows investigators to explore a continuum of values for numerous simulation parameters and to graphically interpret the simulation results (see the PDIpy documentation). We exemplify the model through replicating experimental studies and conducting sensitivity analyses with PDIpy. We expect that this original model, and its implementation as an open-source API, will foster experimental progress towards developing practical PDI systems that combat the medical crisis of antibiotic resistance.

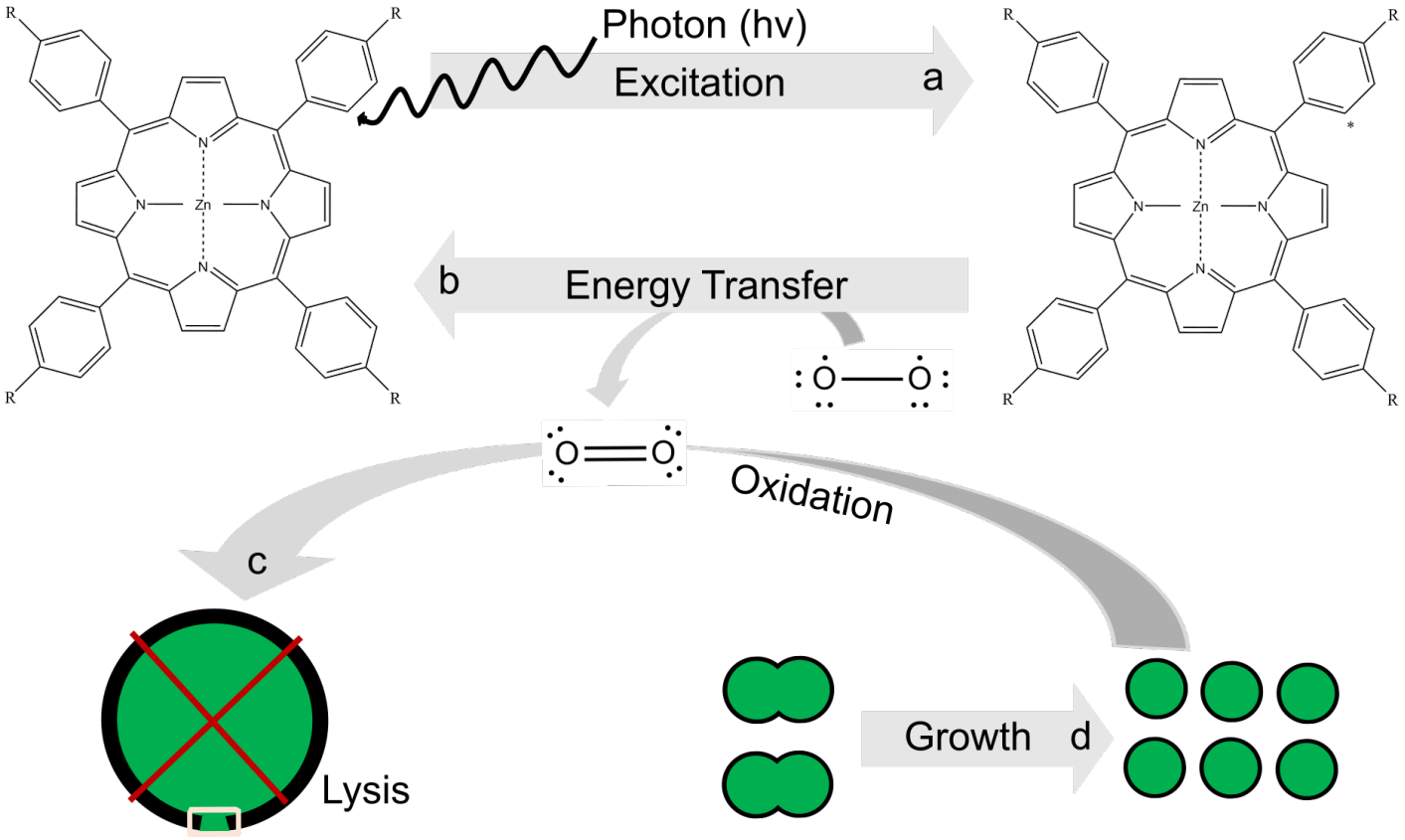

Figure 4.1: The conceptual model of PDI that is captured by our kinetic system. **Step a** is the excitation of a photosensitizer (PS) via incident light at the wavelength to which the PS is tuned. **Step b** is the transfer of excitation energy from the excited PS to ambient oxygen, which reforms the PS catalyst and generates singlet oxygen. **Step c** is the oxidation of membrane phospholipids via singlet oxygen, which rapidly causes membrane lysis and subsequently cell death. **Step d** is the continuous growth of surviving organisms. Each of these processes are represented by chemical reactions and rate laws in our kinetic model.

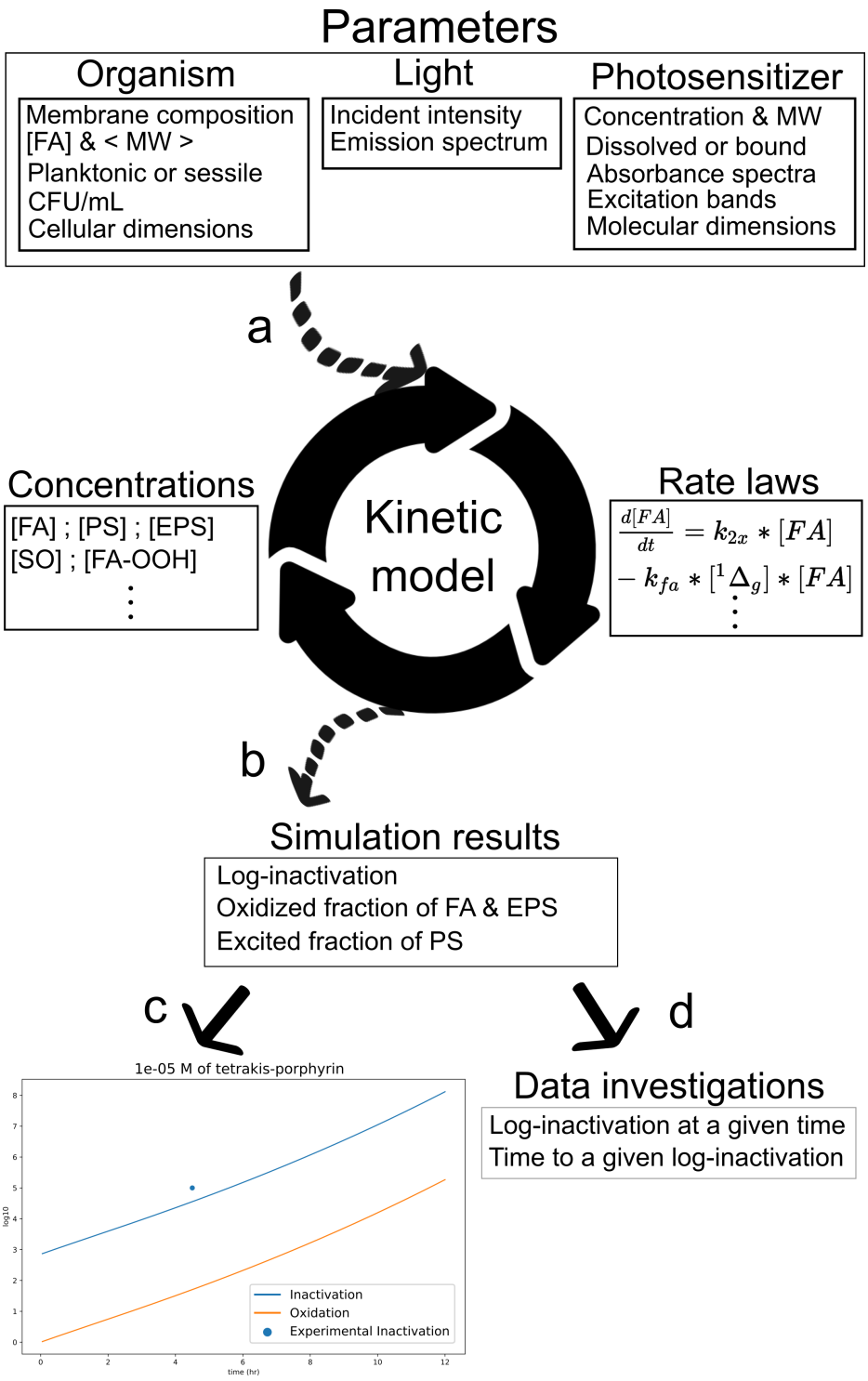

Figure 4.2: The programmatic workflow of PDIpy that implements our kinetic model. **Step a** describes the processing and substitution of simulation parameters – categorically pertaining to the organism, light, and photosensitizer – into the rate laws of our kinetic model. **Step b** executes the populated kinetic model through Tellurium, where concentration changes are calculated via rate laws and concentrations are updated with each timestep. The simulation yields predicted fractions of oxidized membrane fatty acids and excited PSs, which are converted into predictions of inactivation via a calibrated parameter. **Step c** graphically depicts the simulation results with the user-defined specifications. **Step d** investigates the two-dimensional data of predicted inactivation over time by slicing through either variable via a built-in function.

Name	Reaction	Rate laws
Photoexcitation	$^1\text{PS} \underset{k_f}{\overset{k_{ex}}{\rightleftharpoons}} {}^3\text{PS}$	$\frac{d[^3\text{PS}]}{dt} = k_{ex} * \frac{photons_{PS}}{photons_{total}} * \Phi_{ex} * [^1\text{PS}] - k_f * [^3\text{PS}]$
Energy transfer	$^3\text{PS} + {}^3\Sigma_g{}^- \longrightarrow {}^1\text{PS} + {}^1\Delta_g$	$\frac{d[^1\Delta_g]}{dt} = k_{transfer} * \Phi_{transfer} * [^3PS] * [^3\Sigma_g^-]$
Photobleaching	$^1\text{PS} + {}^1\Delta_g \longrightarrow {}^1\text{PS}_{\text{bleached}}$	$\frac{d[^1\text{PS}_{\text{bleached}}]}{dt} = k_{bleaching} * [^1\text{PS}] * [^1\Delta_g]$
Phosphorescence	$^1\Delta_g \longrightarrow {}^3\Sigma_g{}^-$	$\frac{d[^3\Sigma_g^-]}{dt} = k_{phosphorescence} * [^1\Delta_g]$
Membrane oxidation	$^1\Delta_g + \text{FA} \longrightarrow \text{FA}-\text{OOH}$	$\frac{d[FA-OOH]}{dt} = k_{fa} * [^1\Delta_g] * [FA]$
EPS oxidation	$^1\Delta_g + \text{EPS} \longrightarrow \text{EPS}-\text{OOH}$	$\frac{d[EPS-OOH]}{dt} = k_{EPS_{oxidation}} * [^1\Delta_g]$
Reproduction	$\longrightarrow \text{FA}$	$\frac{d[FA]}{dt} = k_{doubling} * [FA]$

Table 4.1: All chemical reactions of the PDI kinetic model. These reactions are individually detailed in the Methods Section 4.2.

4.2 Methods

Conceptual model

Our model represents an experimental PDI system with i) a porphyrin PS, ii) a coccus (spheroid) bacteria such as *S. aureus*, iii) a constant light source, and iv) an aqueous solution that contains a steady-state of dissolved oxygen. The bacteria are represented by fatty acid chains, which our model assumes is the cite of membrane oxidation and hence is the only pertinent bacterial aspect for extracellular PDI. Biofilms, for simulations of sessile systems, are represented as a combination of fatty acid chains (bacteria) and extracellular polymeric substances (EPS) in a predefined ratio for the simulated species, which our model assumes is the cite of oxidation in the biofilm matrix. The model calculates the interaction of $^1\Delta_g$ within the membrane volume or the volume of EPS, since this is the location of PDI inactivation.

Each aspect of this model is represented with a variable: i.e. the PS absorptivity (which can be approximated from molecular dimensions), and the $\frac{mol}{vol}$ or $\frac{mol}{area}$ concentration; the cellular state (planktonic or sessile), and the $\frac{CFU}{mL}$ for planktonic experiments; and kinetic constants for some PDI reactions. These variables are populated in 8 chemical reactions that can be categorized into 4 general processes: a) photoexcitation and photobleaching, $^1\text{PS} \xrightarrow{h\nu} {}^3\text{PS}$ in eq. (4.2); b) energy transfer, $^3\text{PS} \xrightarrow{\text{energy}} {}^3\Sigma_g{}^-$ in eq. (4.3); c) the oxidation of biological substrates; and d) growth of the pathogen. A complete description of these reactions and their respective rate laws is represented in Table 4.1. Each reaction is each detailed in the following sub-sections.

Photoelectric reactions

PS excitation PDI begins with the excitation of the PS via an incident photon. This occurs as the combined result of a photon i) entering the aqueous solution, ii) striking a PS, and then iii) exciting an

electron in that PS. This sequence is encapsulated by the kinetic expression

$$\frac{d[^3\mathrm{PS}]}{dt} = k_{ex} * \frac{photons_{PS}}{photons_{total}} * \Phi_{ex} * [^1\mathrm{PS}] - k_f * [^3\mathrm{PS}] \ . \tag{4.5}$$

The k_{ex} & k_f rate constants are estimated as the inverse of the rise and decay times for the selected PS, respectively. The rise time for a porphyrin PS is approximated as $50fs$ based upon estimates of $< 100fs$ [436] and $[60, 90]$ fs in ethanol solvent [437] that elongates the lifetime of excited molecules relative to water. The decay time, from the S2 fluorescence [438], and Φ_{ex} ($\frac{PSexcited}{photonabsorbed}$) are approximated for a porphyrin PS to be $1.5ns$ and ≈ 0.7 [378], respectively. The $\frac{photons_{PS}}{photons_{total}}$ [433], which is the proportion of photons in the solution that strike a photosensitizer [435], can derive from either emission and absorption spectra of the incident light and the PS [439], respectively, or the series of steps and approximations that are articulated in the Excitation Proportion section of the Supporting Information. The $[^1\mathrm{PS}]$ is finally provided in either molar or $\frac{mg}{area}$, where the latter unit for surface-bound PSs is converted into an effective molar of the PS in the volume within which the surface-bound PS resides immediately adjacent to the substratum surface.

Photobleaching A PS may lose its absorptivity either by experiencing an irreversible rearrangement after collision with a photon – which is described by an oxygen independent, first-order, reaction [414, 440] – or by being oxidized by $^1\Delta_g$ – which is described by an oxygen dependent, second-order, reaction

$$^3\mathrm{PS} + {}^1\Delta_g \xrightarrow{\mathrm{h}\nu} \mathrm{PS{-}OOH} \ . \tag{4.6}$$

We developed a rate law

$$\frac{d[^1\mathrm{PS_{bleached}}]}{dt} = k_{bleaching} * [^1\mathrm{PS}] * [^1\Delta_g] \ , \tag{4.7}$$

for our kinetic model that incorporates both the direct effects of $^1\Delta_g$ and the direct effects of light through $k_{bleaching} \approx 600\frac{cm^2}{J*M}$ [441] which is a function of light exposure $\frac{W}{cm^2}$.

Energy Transfer reactions

The energy transfer $^3\mathrm{PS} + {}^3\Sigma_g{}^- \longrightarrow {}^1\mathrm{PS} + {}^1\Delta_g$ in eq. (4.3) is described by the rate law

$$\frac{d[^1\Delta_g]}{dt} = k_{transfer} * \Phi_{transfer} * [^3PS] * [^3\Sigma_g^-]. \tag{4.8}$$

The rate constant $k_{transfer}$ is the inverse of the decay time of ^{3}PS, which for a porphyrin PS appears to be $100ns$ in aqueous after accounting for the reported value [442] in acetone solvent which significantly increases the lifetime of excited states [443]. The $^1\Delta_g$ phosphorescence side reaction, which often emits a specific infrared wavelength that can be measured to approximate the $[^1\Delta_g]$ [444], is kinetically

represented

$$\frac{d[^3\Sigma_g^-]}{dt} = k_{phosphorescence} * [^1\Delta_g] \tag{4.9}$$

where $k_{phosphorescence}$ is a function of $\frac{CFU}{mL}$, since the $^1\Delta_g$ lifetime is greater in biological material [445] than water [446].

Oxidation

The following oxidation reactions consume oxygen, yet, our model assumes a steady-state of oxygen where the headspace of the simulated system perfectly replenishes consumed oxygen molecules.

Cytoplasmic membrane The oxidation of cytoplasmic phospholipids, which we approximate as fatty acid (FA) chains, is represented as an irreversible reaction [447]

$$^1\Delta_g + \text{FA} \longrightarrow \text{FA}{-}\text{OOH} \tag{4.10}$$

and a second-order rate law

$$\frac{d[FA-OOH]}{dt} = k_{fa} * [^1\Delta_g] * [FA] \ . \tag{4.11}$$

The rate constant $k_{fa} \approx 240\frac{L}{g*s}$ [448] is reported with concentration in units of $\frac{g}{L}$, which we calculated from i) the weighted average MW of the fatty acid chains in the cytoplasmic membrane, ii) the volume of the cytoplasmic membrane, and iii) an assumption that the cytoplasmic membrane volume consists entirely of fatty acid chains.

Biofilm matrix The oxidation of EPS, which represents the biofilm matrix, is reported to be significant during PDI [350]. This process is represented through an irreversible reaction

$$^1\Delta_g + \text{EPS} \longrightarrow \text{EPS}{-}\text{OOH}, \tag{4.12}$$

and a first-order reaction

$$\frac{d[EPS-OOH]}{dt} = k_{EPS_{oxidation}} * [^1\Delta_g] \tag{4.13}$$

with an empirical rate constant of 37.75 $\frac{1}{s}$ for *S. aureus*, and an initial concentration of EPS that is $9x$ greater than the cellular mass [449]. This reaction competes with eq. (4.10) for $^1\Delta_g$ and thereby lessens the efficacy of PDI upon sessile organisms relative to planktonic organisms.

Microbial growth

Cellular reproduction is simulated continuously as simply the increase in [FA] – $\longrightarrow$ FA – since this is the only component of the cell that is pertinent to our model. The corresponding first-order rate law

$$\frac{d[FA]}{dt} = k_{2x} * [FA] \ , \tag{4.14}$$

considers that growth is proportional with the current population of living microbes (represented by the fatty acids concentration). The rate constant k_{2x} is the inverse of the doubling time of the simulated organism.

4.2.1 Inactivation fitting

Inactivation is deduced from oxidation in our kinetic model by presuming an oxidative threshold for lysis around 0.01% of the membrane fatty acids. This is implemented by geometrically translating the log10 predictions of oxidation, as a fraction of the total membrane fatty acids

$$ox_{proportion} = \frac{[FA-OOH]}{[FA-OOH]+[FA]} \ , \tag{4.15}$$

by $\approx$ 4-log: e.g. oxidation predictions of [3,4,5] become inactivation predictions of [7,8,9].

4.2.2 Implementation

The model was implemented in SBML [450] through the Antimony syntax of the Tellurium Python module [451]. This standard model format was combined with a SED-ML description of the model figure [452] into a COMBINE OMEX file [453], which is transparent and reproducible representation of each simulation.

Model calibration

The SBML model format may further enable the programmatic calibration of the lysis threshold parameter through training data and the COPASI software [454]. This lysis threshold is not reported in literature; hence, this threshold, which emerges from our model, is an original prediction and typifies the value of a mechanistic model that can elucidate opaque details.

Beirao et al. The Beirao et al. study [350], which examined the efficacy of a dissolved PS over a range of concentrations against both planktonic and sessile states of *S. aureus*, was used as a training data set. The training procedure included: a) recreating each reported trial through our model, and b) empirically adjusting the threshold parameter such that the total variance across all of the trials is

Bacterial state	[PS] (μM)	Inactivation (-log10)	Reported (min)	Predicted (min)	%-error
planktonic	5	7.6	51	87	60
	10	7.6	51	39	-23
	20	7.6	30	18	-40
sessile	5	3.6	270	247	-9
	10	5	270	337	25
	20	6.3	270	256	-5

Table 4.2: A quantitative comparison of inactivation data from Beirao et al. versus PDIpy predictions after its calibration.

minimized. The final %-errors between the calibrated predictions and the reported values from each trial are depicted in Table 4.2 and Figure 4.3.

Sensitivity analyses

Numerous sensitivity analyses were conducted to determine the significance of experimental variables for PDI efficacy, which can signal worthwhile variables for further experimentation. One of these analyses is highlighted in the following section, while the other analyses are detailed in the Supporting Information.

Light intensity The sensitivity of PDI inactivation to light intensities was explored across a 4-log range of Lux values. The trend over this range, which is represented by Figure 4.4, reveals that the proportion of excited PS plateaus beyond $\approx 13,000\ lux$. Direct inactivation from light, perhaps by exciting endogenous photosensitizers within cells [455, 456, 457], may still proportionally increase inactivation with light intensity beyond $\approx 13,000\ lux$, however, these processes are currently not captured by our model.

PDIpy

The kinetic model is defined as a Python API and is offered through the Python Package Index. Parameter files are also provided with default values for each category of the model variables, which provide an efficient and transparent means of parameterizing a simulation and which further supplement user-defined parameters. The complete list of accepted parameters and formats are detailed in the API documentation.

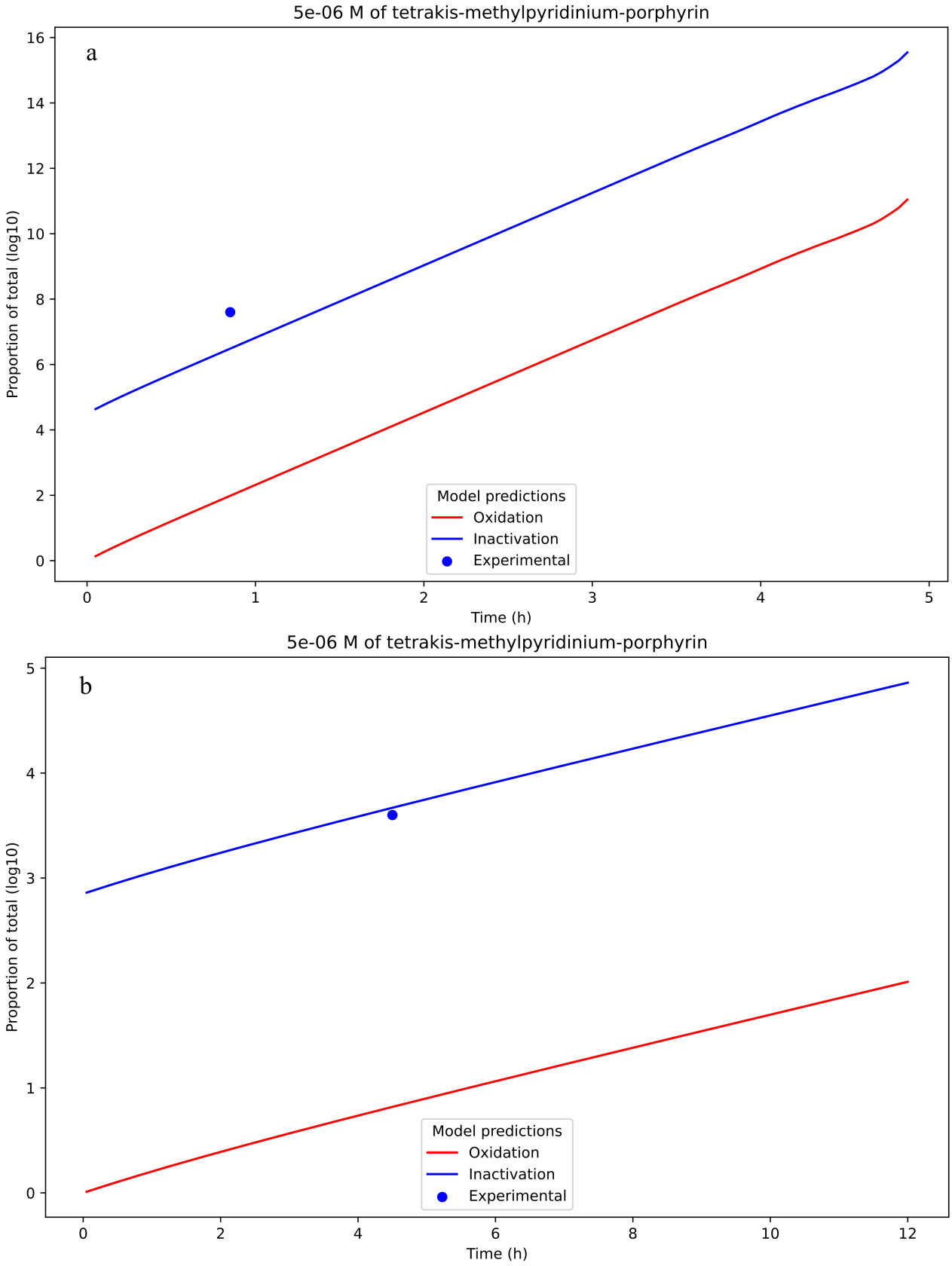

Figure 4.3: Model predictions of the Beirao et al. training data for a) planktonic and b) sessile states, where the dot signifies the reported datum from the trial experiment.

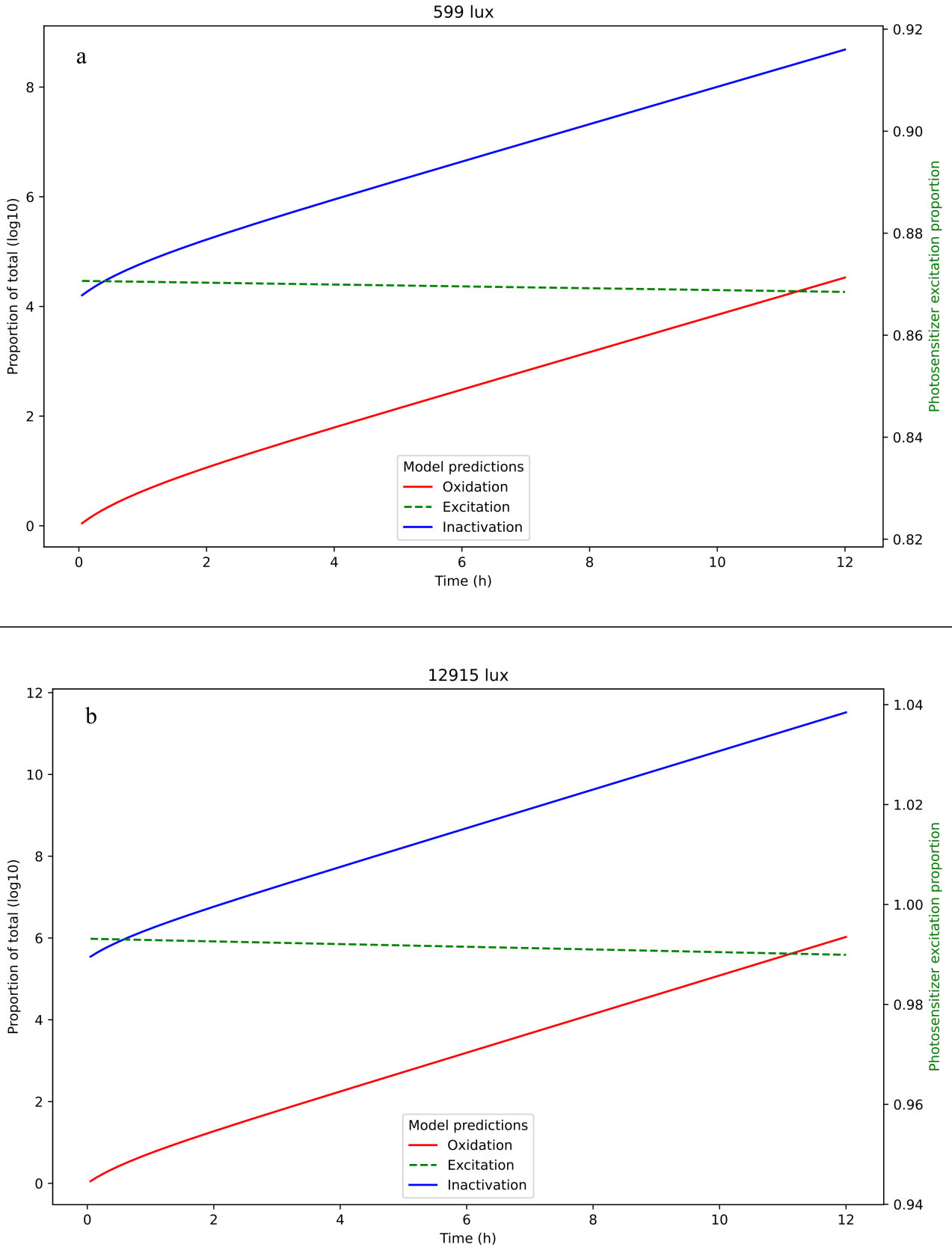

Figure 4.4: The proportion of excited PS, with the associated oxidation and inactivation predictions, at two contrasting light intensities: a) 599 *Lux*, which approximates ambient indoor light, and b) 12915 *Lux*, which approximates ambient daylight. The subtle negative slope that is proportion to the light intensity is the consequence of photobleaching, where incident photons can trigger irreversible rearrangements of the PS and thereby decrease the quantity of photoactive PSs over time.

Discussion

The alignment of model predictions and reported inactivations from our training set supports that the API and underlying kinetic model may guide the design of experimental PDI systems. The %-error between the PDIpy predictions and the training data was interestingly greater in simulations of planktonic bacteria relative to sessile bacteria, which suggests that complexities of the planktonic phase – e.g. PS permeability, which causes cytosolic oxidation – are currently not captured by our kinetic model.

The sensitivity analyses of the model variables illuminate its dynamic capacity to explore the space of PDI systems. This exhibits distinguishing features of this model, relative to other PDI models, to i) simulate diverse sets of experimental PDI conditions; ii) intuitively execute the kinetic model, and automatically visualize results, through the API interface; and iii) resolve the fundamental kinetics of PDI. We believe that this kinetic model and its open-source implementation as PDIpy will support developing PDI applications that can confront the looming crisis of AMR.

4.3 Author Contributions

APF Designed, executed, and codified the project.

JRK Guidance and manuscript edits.

HLB Guidance, manuscript edits, and funding.

4.4 Acknowledgments

The authors are grateful to Ethan Sean Chan for developing the framework of iPDIpy, which will be introduced in a future release of PDIpy. The authors thank the members of the Buckley and Wolff Groups at the University of Victoria for contributing ideas and data that were used to refine this PDI model.

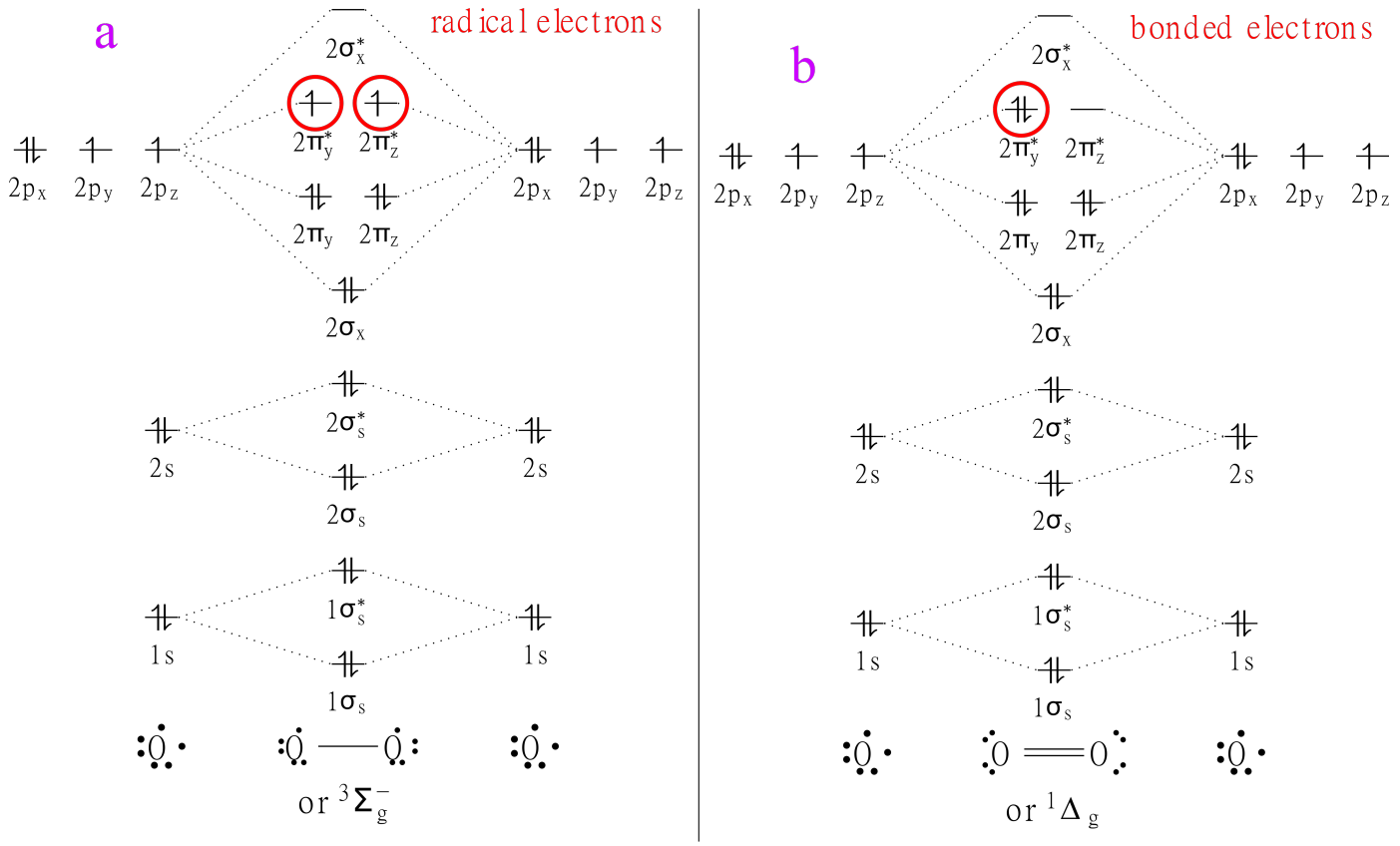

Figure 4.5: Qualitative orbital diagrams for a) $^3\Sigma_g^-$ and b) $^1\Delta_g$ configurations of diatomic oxygen. Each barbed arrow represents a single electron, and each platform represents the electronic sub-orbital of the respective label, where orbital energy increases vertically in the diagram. The distinction between a) and b) is highlighted by the red circled electrons and labels, where $^1\Delta_g$ possesses an anti-bonding π^*-bond in its HOMO that destabilizes it relative to $^3\Sigma_g^-$.

4.5 Supporting Information: PDIpy

4.5.1 Molecular properties and mechanisms

The electronic difference between $^1\Delta_g$ and $^3\Sigma_g^-$ is best depicted through their respective molecular orbital diagrams in Figure 4.5. The photochemical processes of $^1\Delta_g$ generation are depicted in Figure 4.6, while the subsequent oxidation reactions are sampled in Figure 4.7.

4.5.2 Excitation proportion

The steps for estimating the absorbed proportion of incident photons by photosensitizers, where absorbance or transmittance measurements are not available, are detailed through the following steps. a) The reported intensity of incident light from the respective light source – i.e. irradiance ($\frac{mW}{cm^2}$), lux ($\frac{lumen}{m^2}$), or lumens (lumens) – is converted into a quantity of incident watts $watts_{in}$ ($\frac{J}{s}$). b) This incident wattage is attenuated by the proportion of the emission spectra $spec_{em}$ that resides within the $spec_{ex}$ of

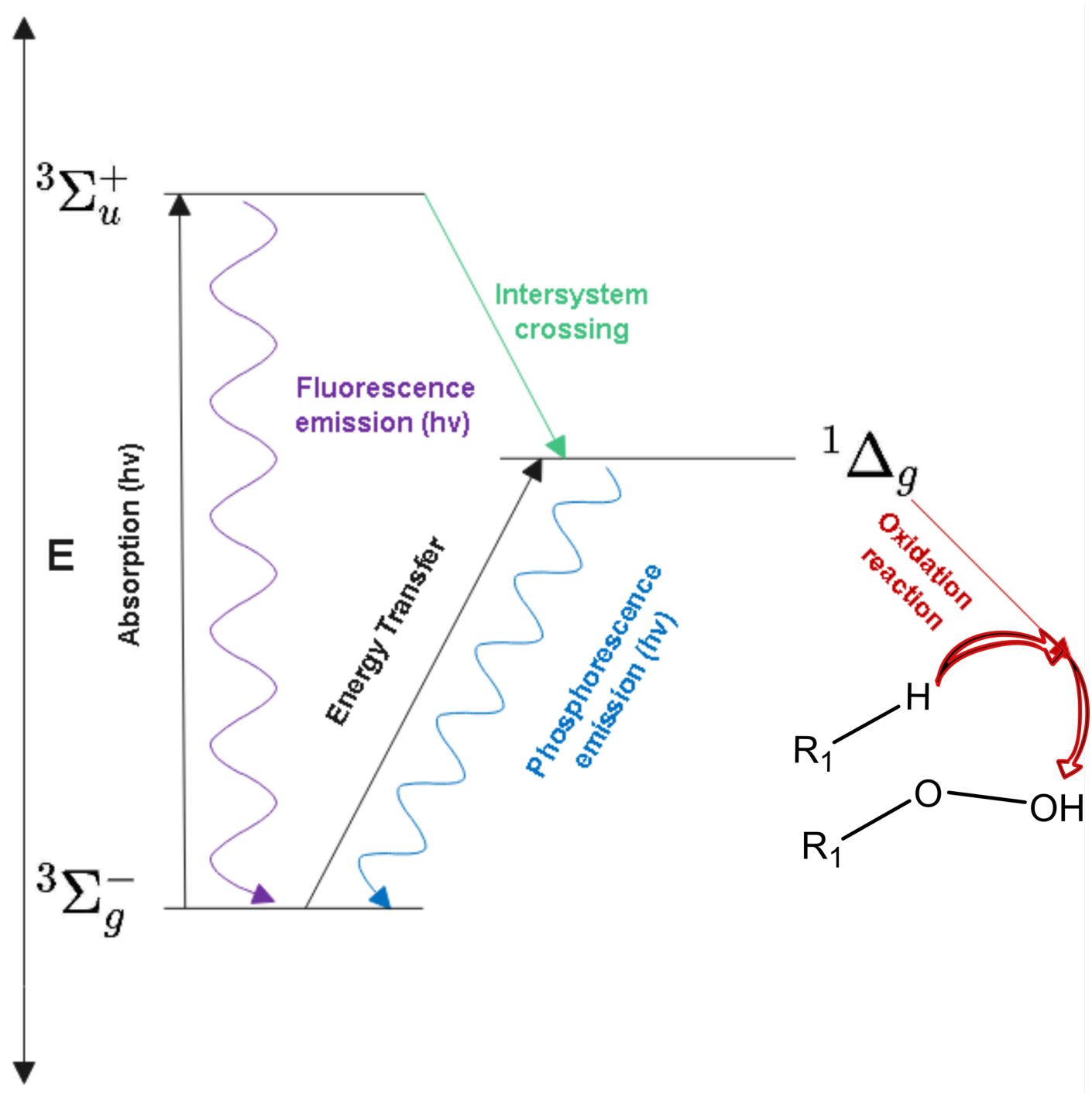

Figure 4.6: A qualitative Jablonski energy diagram of Steps b-c of PDI. The initial excitation in PDI occurs via an energy transfer $^3\Sigma_g{}^- \xrightarrow{\text{energy transfer}} {}^1\Delta_g$. The ROS then, while abstaining from phosphoresce, oxidizes a biological substrate to form a peroxide that gradually compounds to cause lysis.

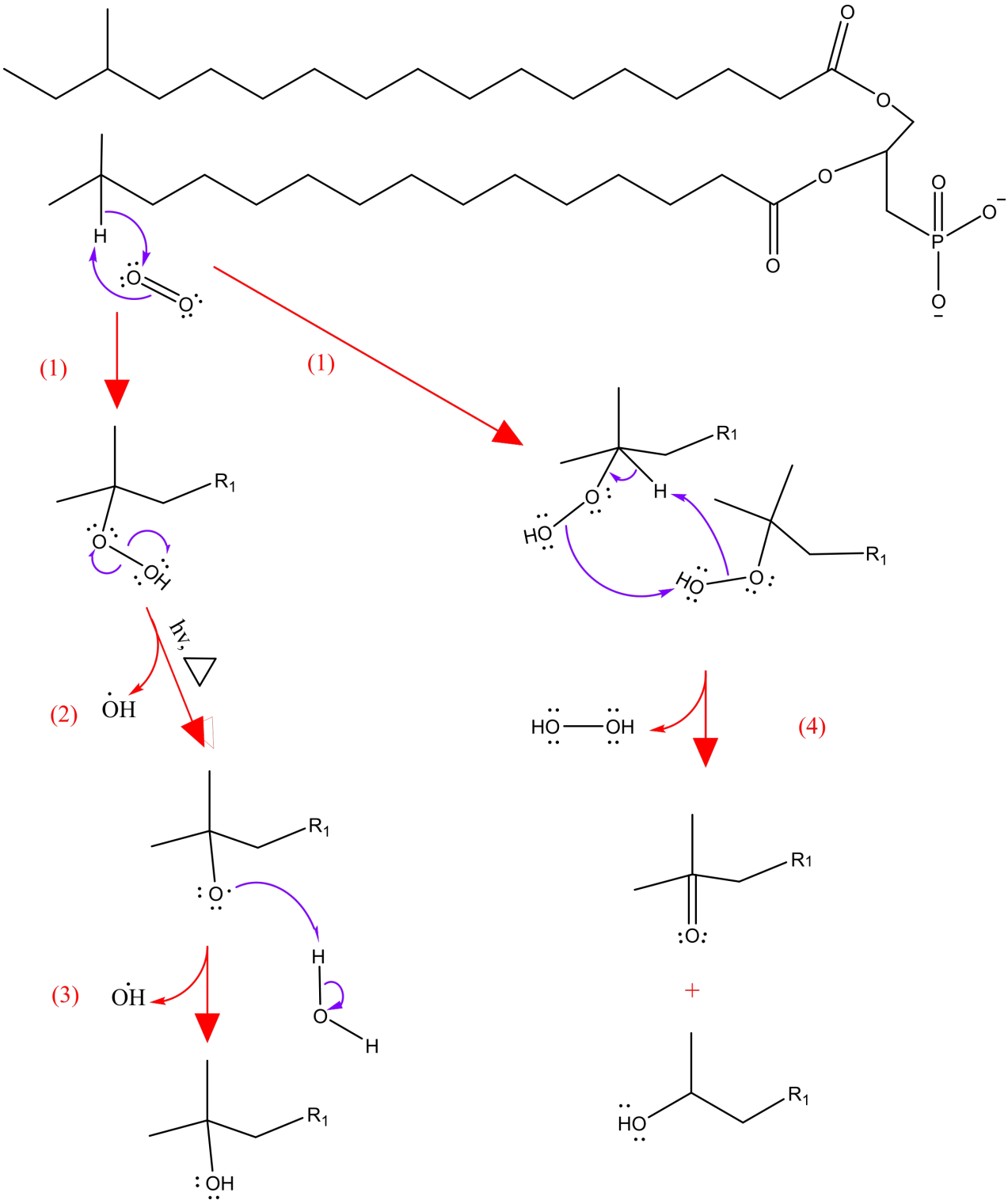

Figure 4.7: The reaction mechanisms of Type II oxidation and subsequent decompositions. **Step (1)** depicts the concerted [458] Schenck reaction. **Step (2)** depicts the homolytic cleavage of the hydroperoxide bond to form $OH^{\bullet}$ and an oxy radical that may enter autoxidation (Type I oxidation) mechanisms. **Step (3)** depicts radical propagation via hydrogen abstraction to form another radical substrate and an alcohol byproduct. **Step (4)** is a concerted Russell reaction [459, 460] between two peroxides that forms a H_2O_2, an α,β-ketone, and an alcohol. The reactions of Steps (2-4) sample the wide range of possible decompositions that follow oxidation mechanisms.

the PS,

$$watt_{ex} = \frac{spec_{ex}}{spec_{em}} * watts_{in}. \tag{4.16}$$

c) The $watt_{ex}$ is then used to calculate the moles of incident photons that strike photosensitizers per timestep

$$\frac{photons_{strike\ PS}}{timestep} = \frac{< h\nu_{ex} >}{h * c} * watts_{ex} * \frac{s}{\Delta t} * reflection * scattering * \frac{1\ mole}{N_A} * \frac{vol_{PS}}{vol_{total}}, \tag{4.17}$$

where $reflection \approx 96\%$ and represents the proportion of incident photons that penetrate an aqueous solution [461]; and $scattering\left(\frac{I_z}{I_0} = e^{-k*z}\right)$ represents the proportion of light $\frac{I_z}{I_0}$ that reaches a specified depth z [462], where k is the attenuation coefficient that is ≈ 0.04 $(\frac{1}{m})$ [463] for clear water. The quotient $\frac{vol_{PS}}{vol_{total}}$ describes the fraction of the solution volume where the PS resides (vol_{total}) that is comprised of the PS per se (vol_{PS}), which is calculated as the product of the quantity of PS molecules and the volume per molecule according to its molecular structure. The average excitation wavelength of the PS ($< h\nu_{excitation} >$) is calculated as the weighted average of the Soret and Q excitation bands, in proportion to their relative contribution in generating $^1\Delta_g$ [464, 465], which assumes that both excitation wavelengths are excited during the simulation. The resultant $\frac{photons_{strike\ PS}}{timestep}$ from eq. (4.17) is then divided by the quantity of photons that enter the system per timestep $\frac{photons_{total}}{timestep}$ to determine which fraction of photons strike a photosensitizer.

4.5.3 Deduction of inactivation via the Hill equation

Inactivation may alternatively be deduced from oxidation through parameter manuipulation of a fitted sigmoidal curve, similar to other models [466]. The Hill-equation [467] is a sigmoidal model that derives from mass-action kinetics, similar to the Michaelis-Menten kinetic model, and thus it was selected the signmoidal model for this alternative framework. A Python program for fitting the Hill-equation was developed – the HillFit module – with a variation of the Hill-equation [468]

$$y = bottom + \frac{(top - bottom) * x^n}{EC50^n + x^n}, \tag{4.18}$$

that introduces an additional *bottom* parameter for more advantageous fitting. The predicted oxidation data was fitted to a hill-equation via HillFit and the parameters were subsequently adjusted in Table 4.3 to optimally meet the training data. The *top* parameter of eq. (4.18) is adjusted asymptotically to a limit that follows an subtly different empirical expression for planktonic $1 - 10^{-\Omega}$ than biofilm $1 - 10^{-0.7-\Omega}$ simulations, where $\Omega = wattage^{\frac{1}{5}} - log10(1 - final_{oxidation\_proportion})$. This limit manifests in the predicted inactivation being $\approx [1, 2] - log$ greater than the predicted oxidation, which implicitly specifies an oxidation thereshold of $\approx [1, 10]\%$. The different parameter adjustments between sessile and planktonic systems may be explained that numerous chemical influences, such as diffusion rates, are not explicitly considered in our kinetic model. The regression plots for the fit of the Beirao et al. training

Bacterial state	Hill parameter	Adjustment
Planktonic	EC50	-76%
	nH	+100%
Biofilm	EC50	-65%
	nH	+120%

Table 4.3: The Hill parameters adjustments that are enacted to create the inactivation plot for both planktonic and biofilm systems.

data is depicted in Figure 4.8. The very precise fitting – $R^2 > 0.996$ – supports that the Hill-equation is an accurate description of our kinetic PDI model, and conversely that our model fundamentally describes a biochemical relationship.

4.5.4 Oxidized membrane region

The region of the bacterial membrane that is oxidized by cross-linked PSs may be a small fraction of the total membrane, provided that the bacterium does not have a tremendous angular momentum. This is not presently captured by our model, but the following logic could incorporate this concept into the model. The oxidized region of a coccus bacterial cell can be determined from the cellular radius and volume

$$radius_{cell} = \sqrt[3]{3 * \frac{volume_{cell}}{4\pi}} \ . \tag{4.19}$$

The membrane volume is calculated

$$volume_{membrane} = \frac{4\pi}{3} * (radius_{cell}^3 - (radius_{cell} - th_{membrane})^3) \tag{4.20}$$

there the thickness of the cytoplasmic membrane $\approx 4nm$. The volume of oxidized membrane is then calculated

$$volume_{oxidized} = volume_{membrane} * \frac{angle_{oxidized}}{360} \ , \tag{4.21}$$

where the $angle_{oxidized}$ describes the angle in degrees from vertical at which the farthest $^1\Delta_g$ reaches the mebrane. The fraction of the membrane volume that is oxidized is then calculated

$$oxidized = \frac{volume_{oxidized}}{volume_{membrane}} \tag{4.22}$$

and applied to augment the effective oxidation proportion

$$oxidation_{proportion,new} = \frac{oxidation_{proportion,old}}{oxidized} \ . \tag{4.23}$$

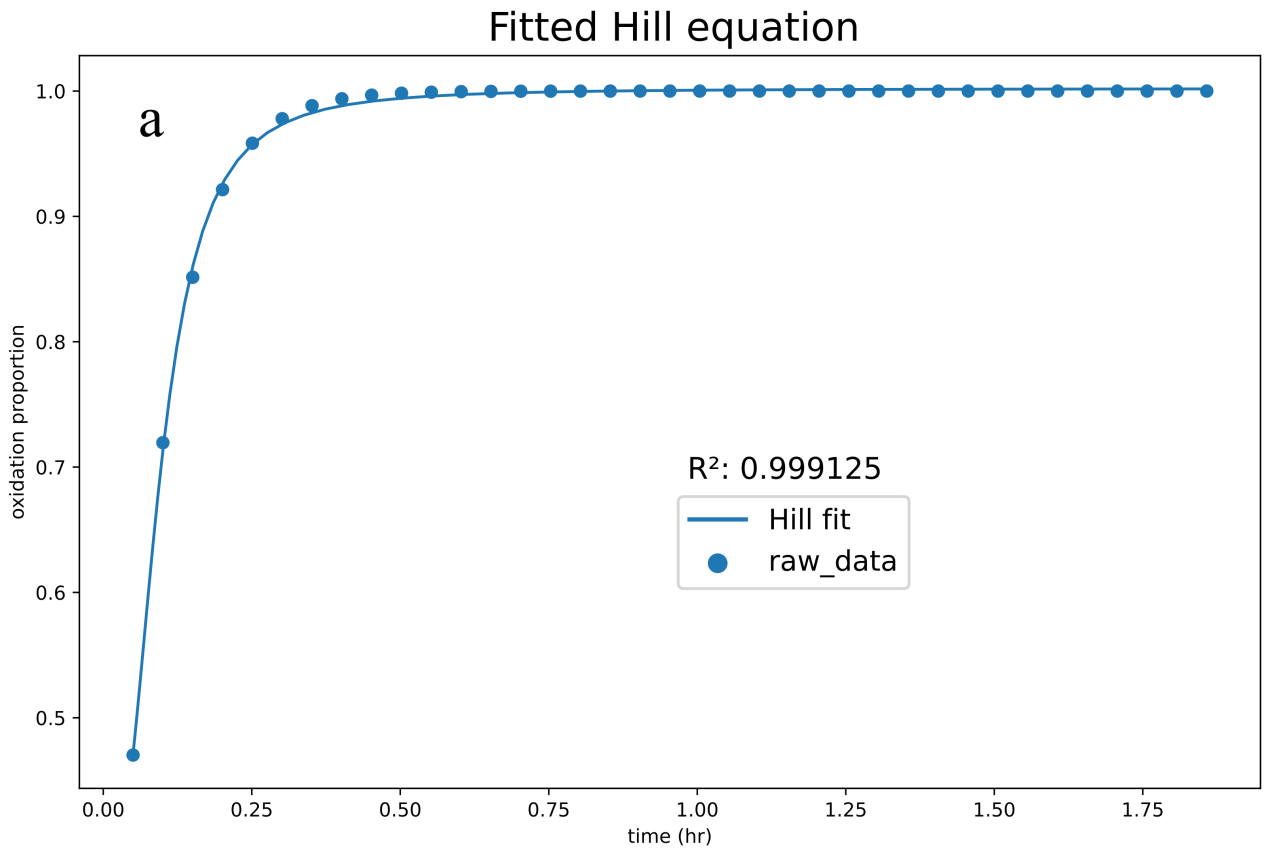

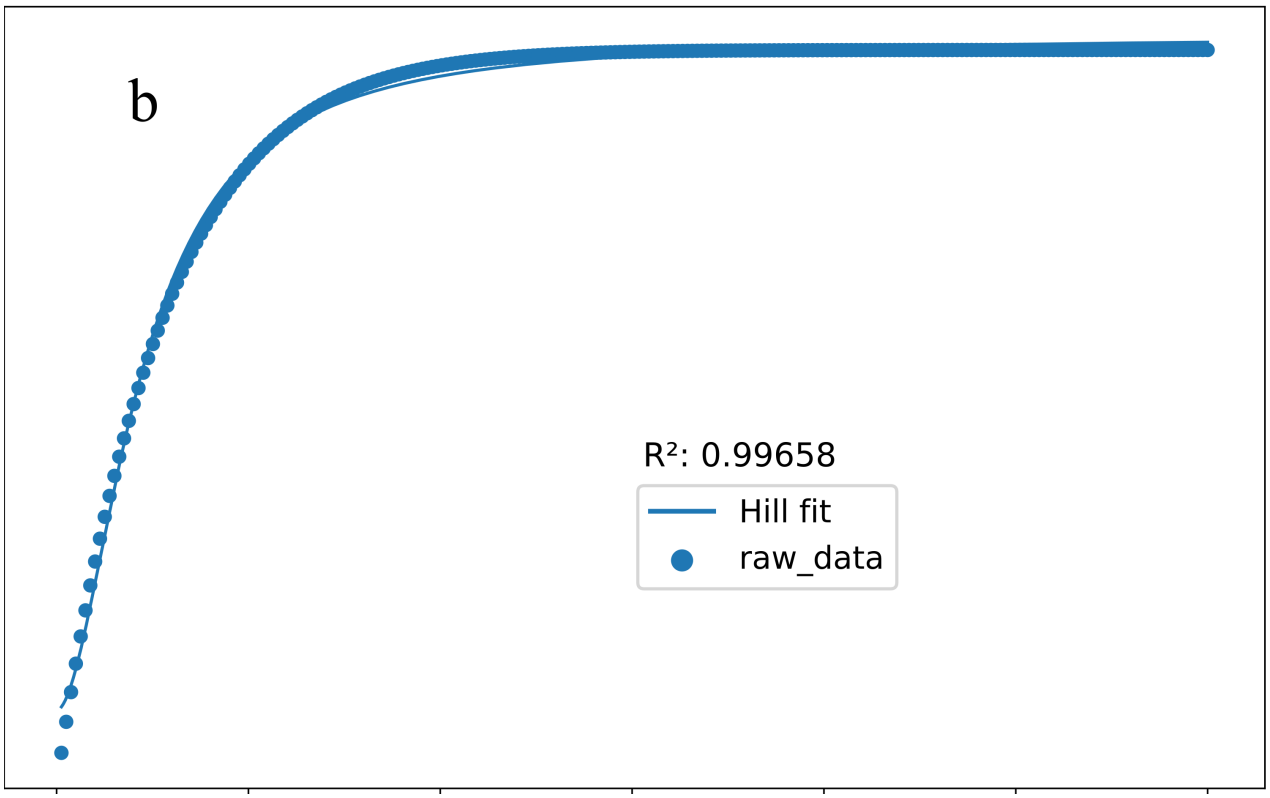

Figure 4.8: The Hill-equation regressions for the oxidation plots of the Beirao et al. training data for a) planktonic and b) sessile states. The high R^2 correlation supports that our chemical model of PDI recreates a sigmoidal biochemical relationship. The greater number of data points in panel b) is the consequence of a far longer simulation time than the simulation of panel a).

4.5.5 Sensitivity analyses

Light source & emission The sensitivity of simulation results to the light source – incandescent, LED, or fluorescent – was explored. The comparison of incandescent and LED light sources, where LED and fluorescent were nearly indistinguishable, is depicted in Figure 4.9. These simulated differences are solely attributed to differences in the proportion of emitted photons that are within the visible spectrum, since PDIpy does not current resolve the intensity of specific emitted wavelengths or consider the inactivation effects of heat from incandescent bulbs. The visible proportion of the emitted wavelengths was determined in Figure 4.10 to have minimally consequence above 20%.

Bacterial CFU/mL The influence of bacterial $\frac{CFU}{mL}$ upon the rate of oxidation in PDIpy was tuned to yield the trend that is depicted in Figure 4.11, where the rate of oxidation is inversely proportional with the $\frac{CFU}{mL}$. This is intuitive, where larger bacterial populations requires more time to eradicate.

Photobleaching constant The influence of photobleaching constant was explored over an 8-log range of values, which is depicted in Figure 4.12. The values below $1E4$ are indistinguishable over time.

4.5.6 Supplementary figures

This section includes supplementary figures for the main text. The natural and synthetic porphyrins that inspire the design of photosensitizers are depicted in Figure 4.13.

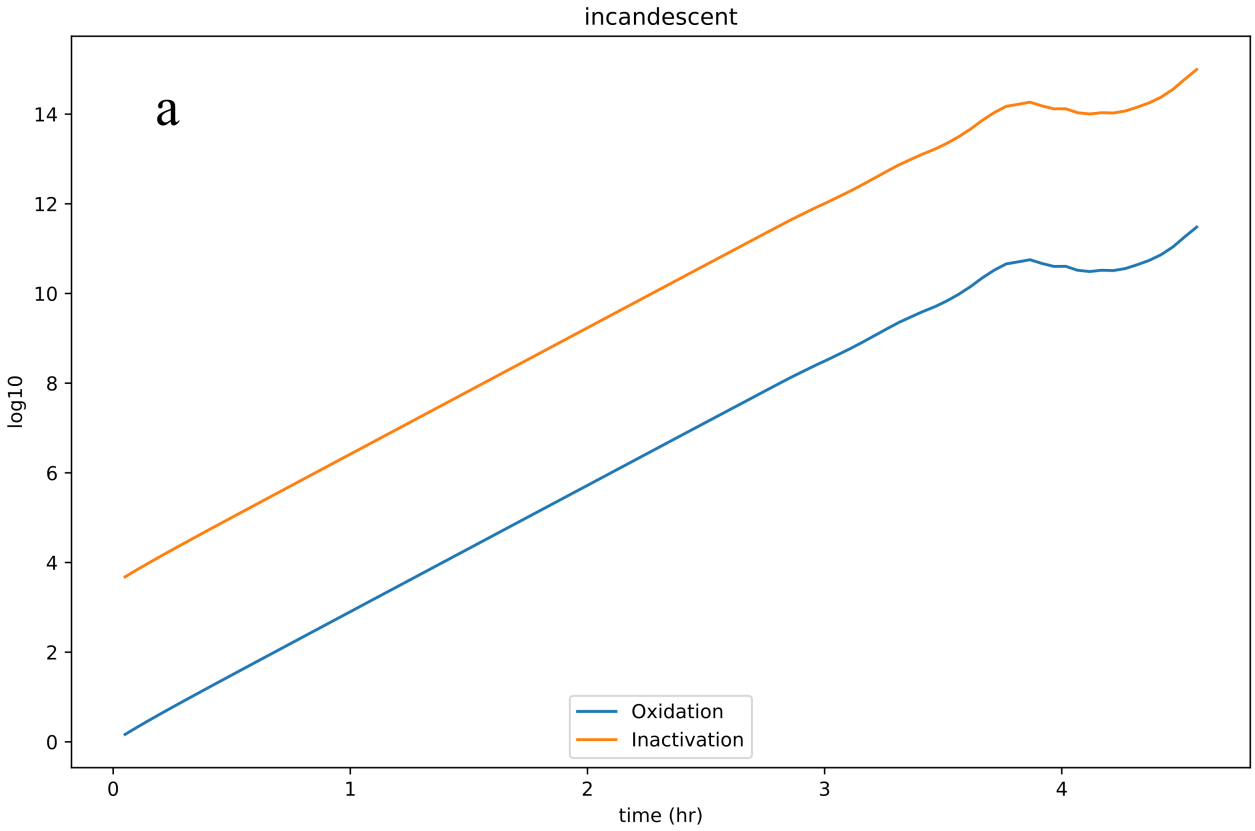

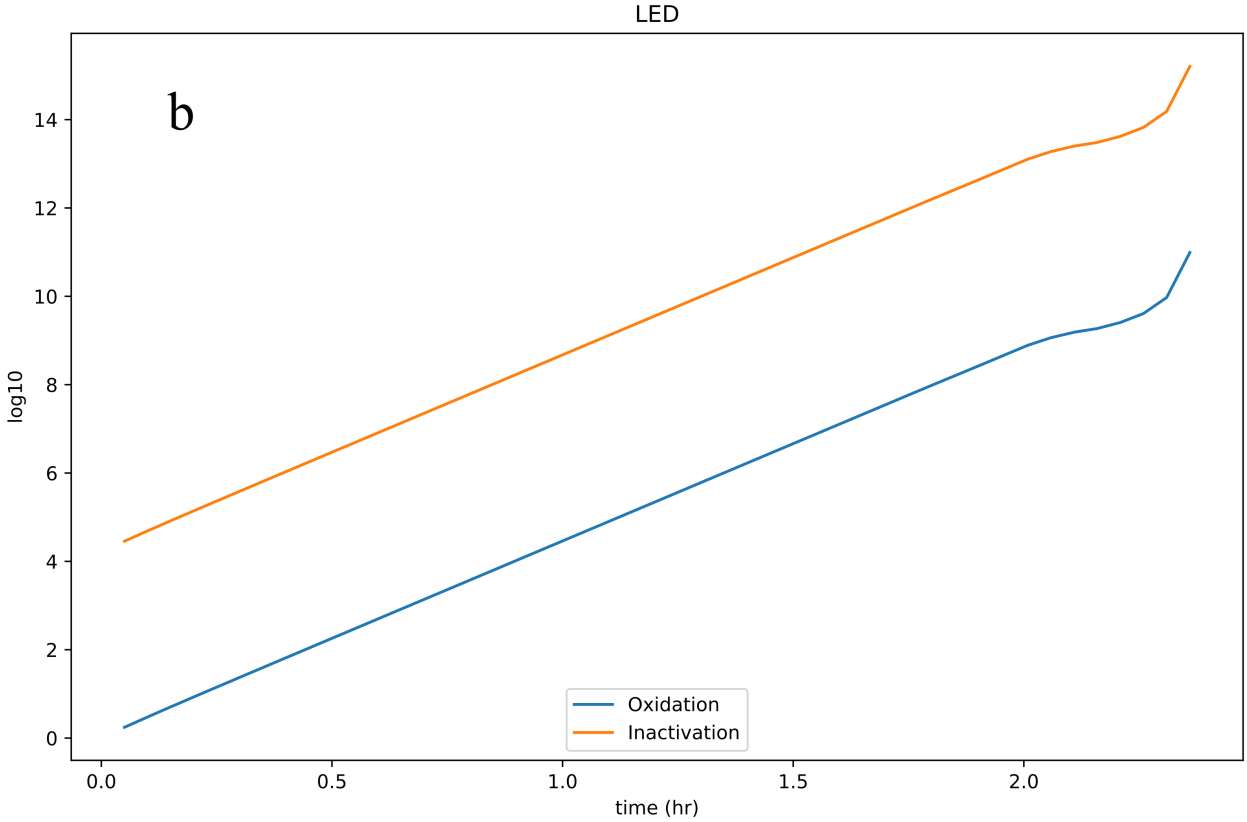

Figure 4.9: A comparison of the same experiment under a) incandescent and b) LED light sources. The discrepancy between the inactivation of the two sources is attributed to the proportion of emission that resides in the visible spectrum.

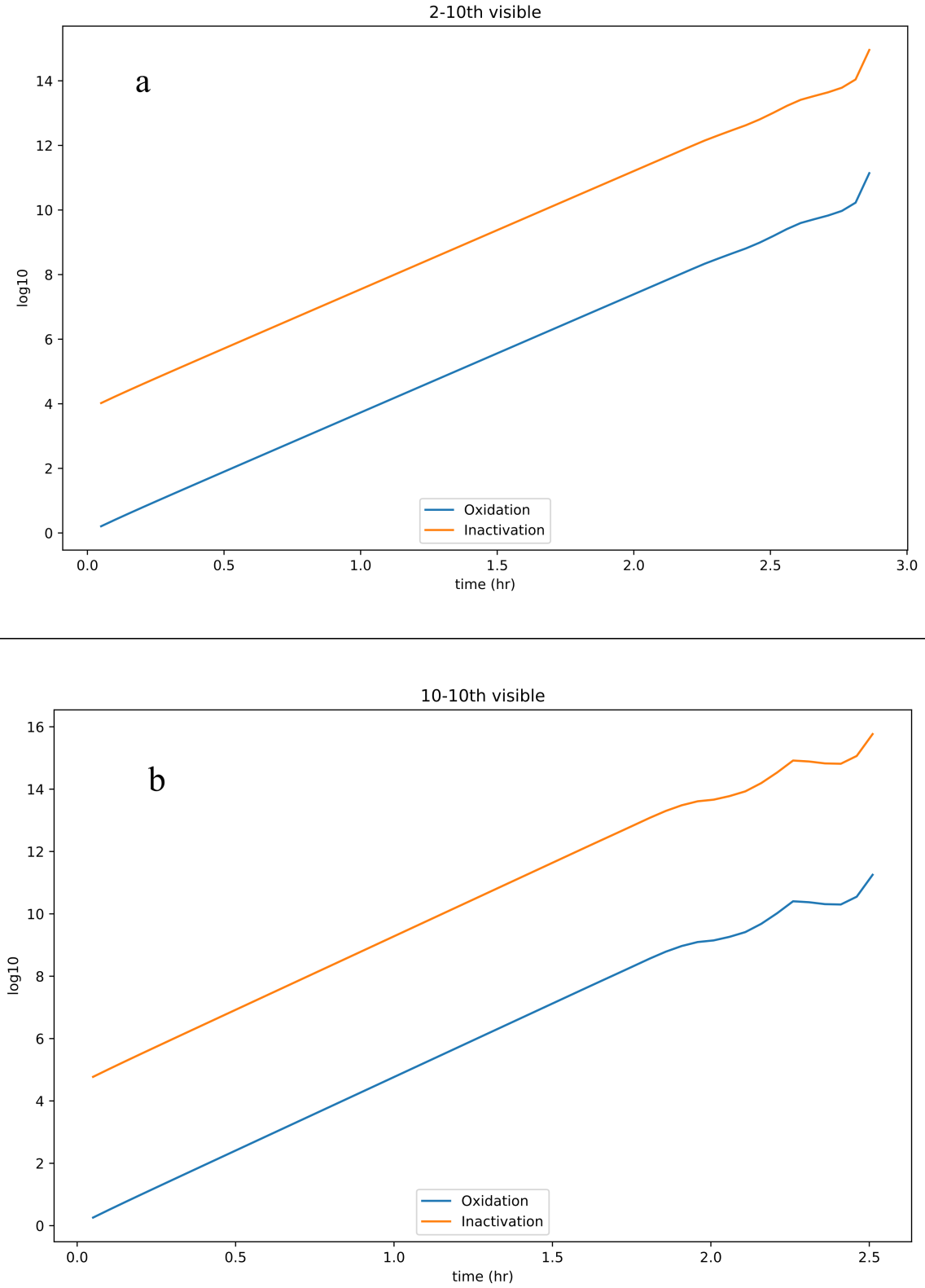

Figure 4.10: A comparison of the same experiment with a light source that possesses a) 20% visible light and b) 100% visible light, where the former value appears – for these simulation conditions – to be the threshold beyond which the proportion of visible light does not substantial effect inactivation rates. This threshold is likely dependent upon the quantity of incident watts; in which case, this threshold is not broadly generaliazable for all simulation conditions.

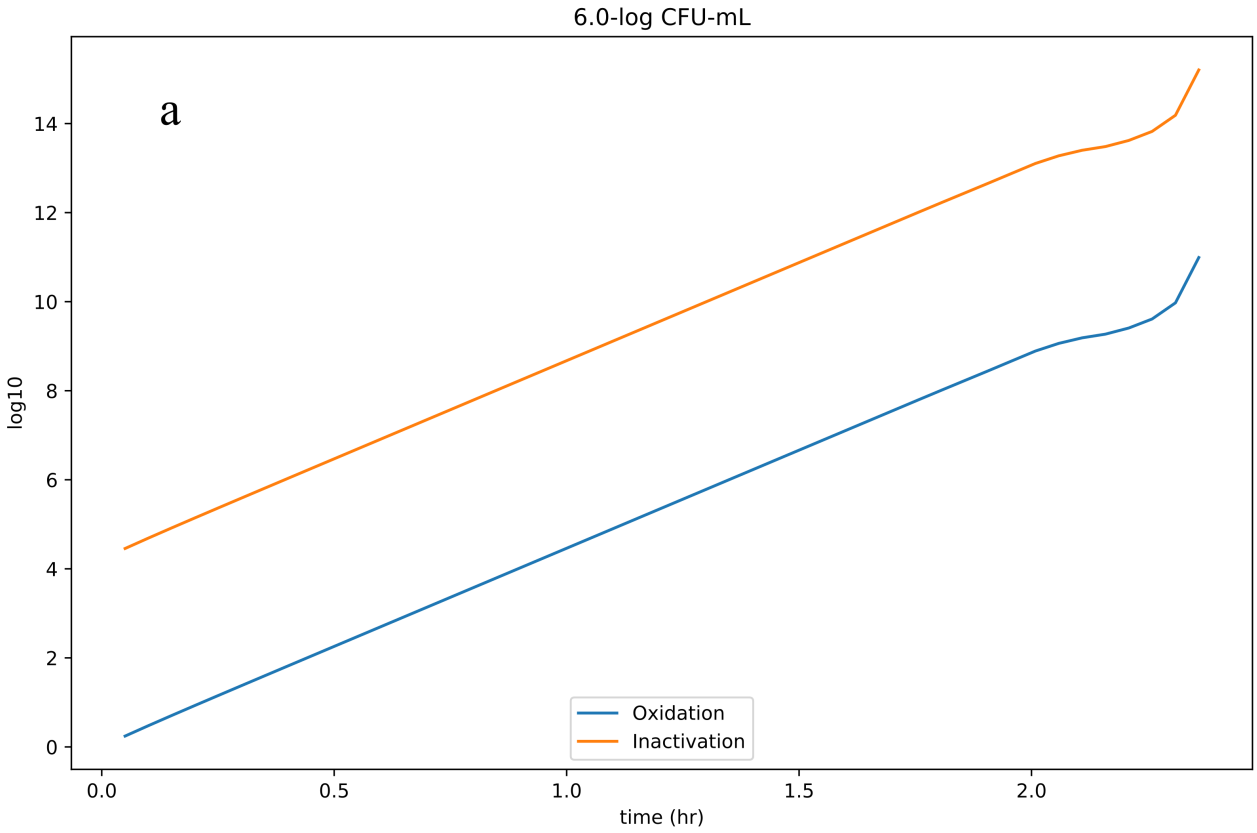

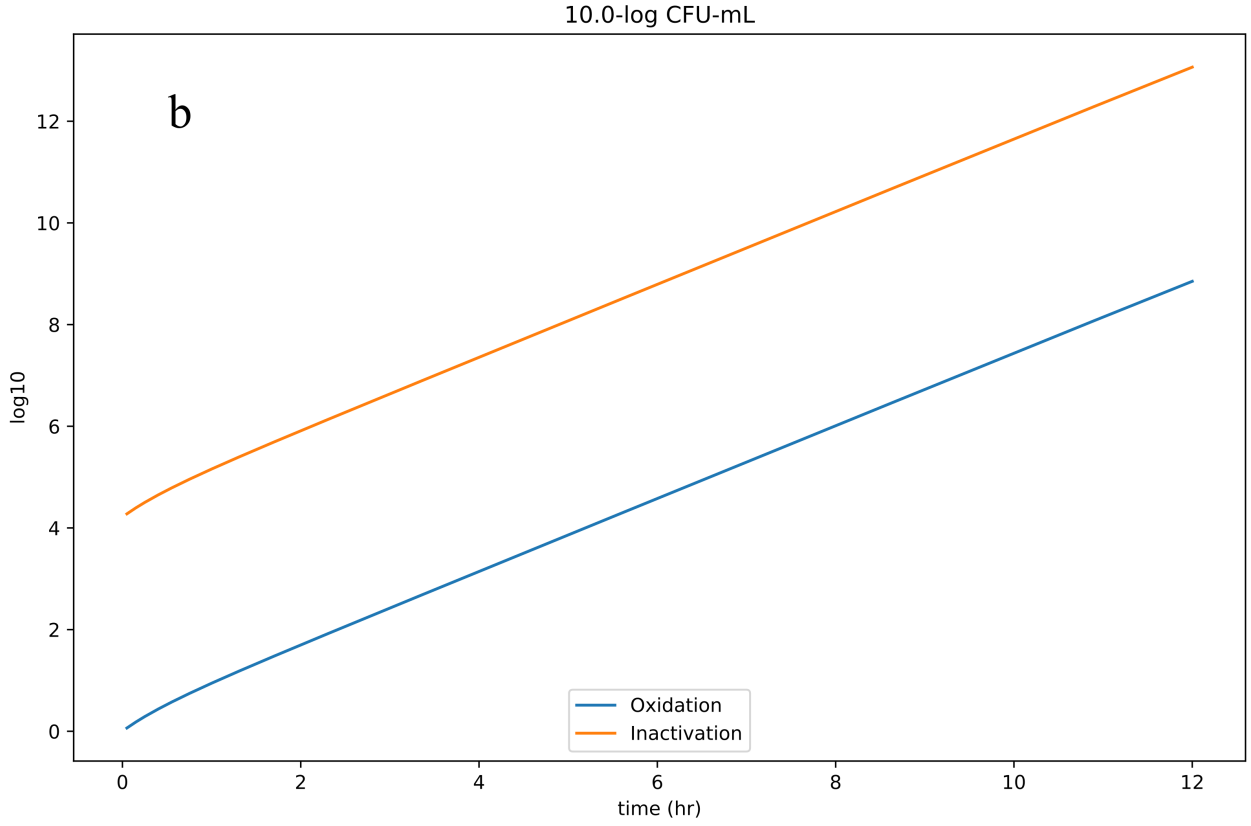

Figure 4.11: A comparison of oxidation and inactivation between a) 1E6 and b) 1E10 $\frac{CFU}{mL}$. The imposed trend is that oxidation and thus inactivation are inversely proportional to the colony size, which is the intuitive result.

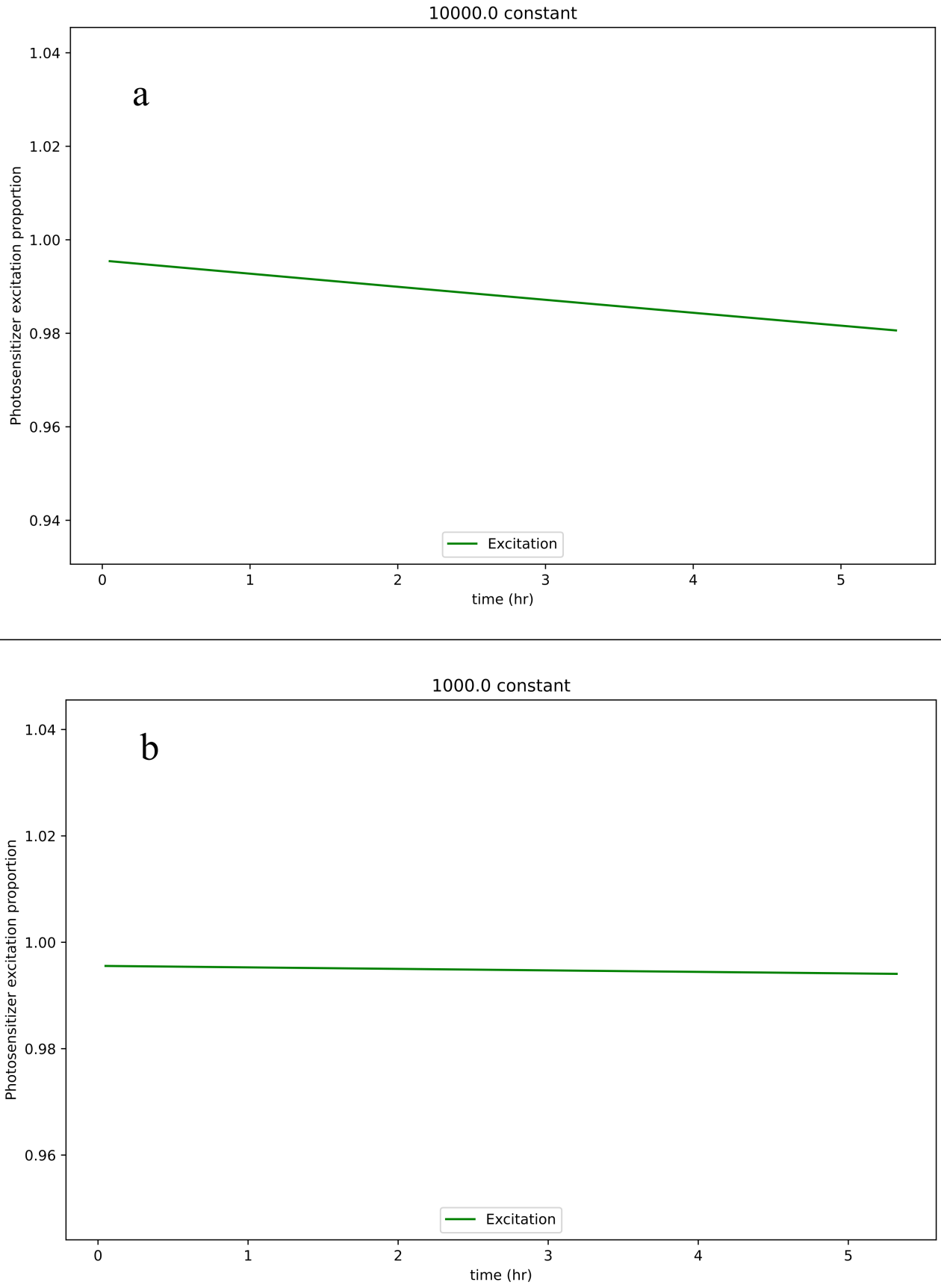

Figure 4.12: A comparison of the excitation proportion with two photobleaching constants. Constant values below 1E4 are approximately indistinguishable.

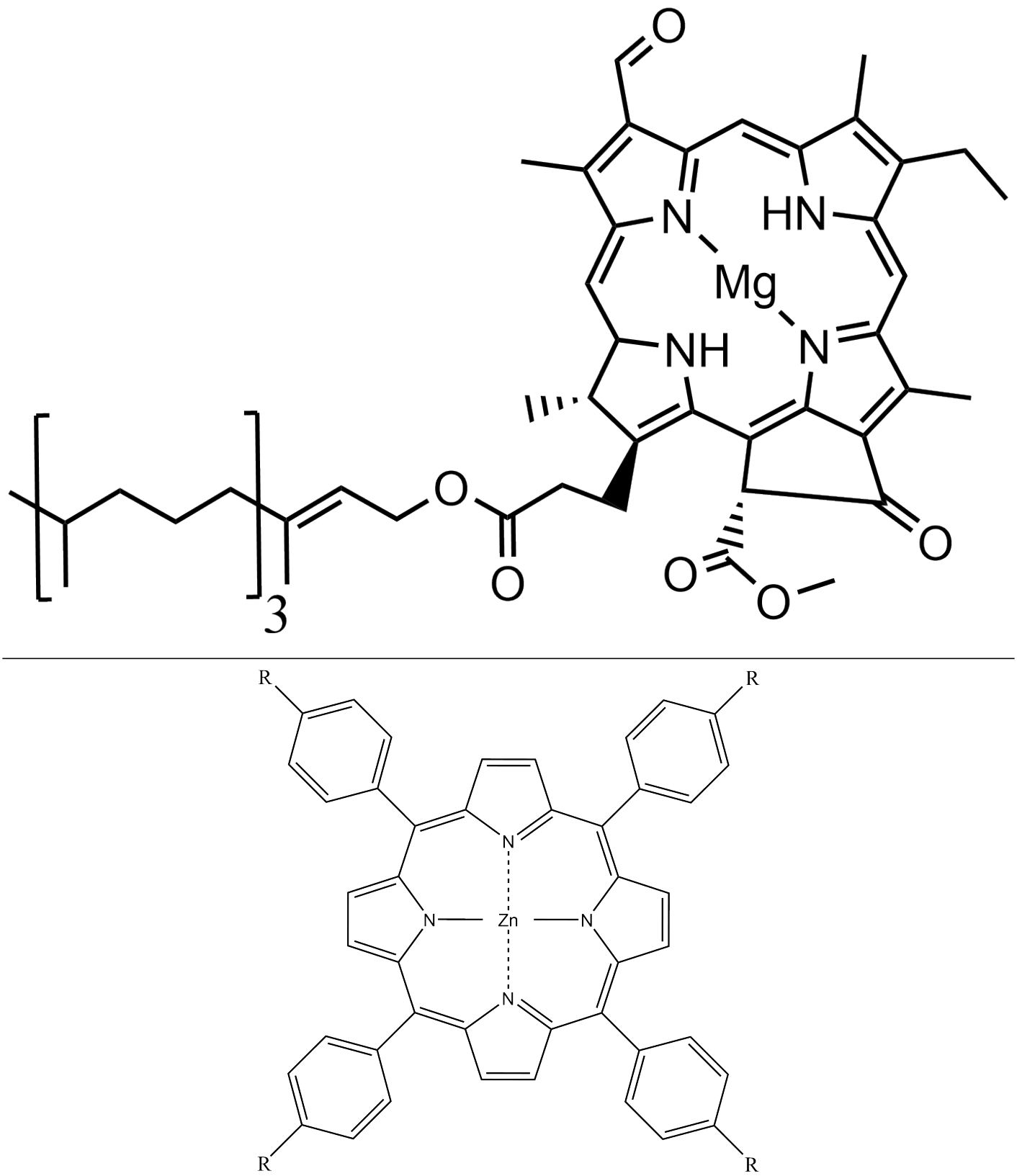

Figure 4.13: The chemical structure of porphyrinoid chlorophyll (top) juxtaposed with the core motif of a synthetic porphyrin analogue (bottom). The "R" groups of the synthetic porphyrin can be substituted with a range of functionality to tailor the PS for the specific PDI system.

Chapter 5

Future work

The Thesis projects can be improved through the following lists, which are organized by their respective chapter and their necessity towards our goal of publishing the work.

5.1 ROSSpy

5.1.1 Necessary

1. **Publish** - refine the manuscript & documentation and submit it for peer-review (*Desalination*).

5.1.2 Auxiliary

1. **Dual domain** - discern how to simulate the dual domain in PHREEQC.
2. **iROSSpy** - execute the PHREEQC batch software in the iROSSpy script to create an operational command-line version of ROSSpy for non-technical users.
3. **evaporation** - investigate why scaling from desalination quantitatively exceeds that from evaporation by 50%, despite controlling for the differences in pore volume of the solutions and the total active area of the desalination module.

5.2 PDIpy

5.2.1 Necessary

1. **Cross-linked PS** - simulate a cross-linked PS, which specifically involves a) encapsulating the diffusion-limited inactivation with planktonic bacteria, and b) the effectively condensed simulation volume with sessile bacteria.

2. **COPASI calibration** - calibrate the inactivation lysis threshold parameter through COPASI. This will improve the transparency and precision of the calibrated value, which is an important fortification before we publish our model.

3. **Experimental guidance** - collaborate with Grace Tieman to use PDIpy in guiding a PDI experiment, and contrast the results of that experiment with the predictions in the paper. This will be the pinnacle of the paper.

4. **Publish** - refine the manuscript & documentation and submit it for peer-review (*BioPhysical Journal*).

5.2.2 Auxiliary

1. **iPDIpy** - connect PDIpy with the GUI framework that has been drafted for non-technical users.

2. **Oxidation region** - implement the augmentation of the oxidation proportion for the region of the bacterial membrane that is exposed to a surface of cross-linked PSs.

3. **Light effects** - embody the contribution of endogenous photosensitizers – and the permeability of PS and thus cytoplasmic oxidation – in inactivation effects, particularly at high light doses.

5.3 WCMpy

5.3.1 Necessary

1. **Codons: tables** - expand the accepted variations of codon translations for other organisms, possibly by using the "codons-usage-table" Python module.

2. **dFBApy: conditions selection** - add the ability to only use the kinetic data that most matches the specified conditions of temperature, pH, or possibly taxonomic similarity for similar organisms for which more data is available.

3. **BiGG_SABIO: multiple entries** - allow the refined kinetics file to provide multiple entries of data for each reaction/enzyme, which will permit the above aspiration for expanding the dFBA function.

4. **BiGG_SABIO: chemical synonyms** - improve the ability to match chemical and enzyme names between the BiGG and SABIO conventions.

5. **WCMpy: cytoplasm chemistry** - amalgamate the suite of packages into an operational cytoplasmic model.

6. **WCMpy: visualization** - visualize geometric growth of a cell over the simulation.

7. **WCMpy: biofilms** - apply a WCMpy model to a biofilm community, within a biofilm framework (e.g. the CA algorithm) and considerations of extra-cellular chemistry.

8. **WCMpy: Publish** - update the manuscript & documentation and submit it for peer-review (*BioPhysical Journal*).

5.3.2 Auxiliary

1. **Codons: protein analysis** - visualize and interpret translated proteins through the "Minotaor" Python module.

2. **Codons: GC %** - calculate the fraction of a genome that consists of Guanine and Cytosine, which is an influential property for biophysical experiments.

3. **Codons: back translation** - determine the potential genetic sequences that beget a known protein sequence, thereby expanding upon the "backtranslate" Python module.

4. **BiGG_SABIO: real-time analysis** - check scraped SABIO-RK reaction data for alignment to the GEM model in real-time, where only matched data will be saved. This will importantly prevent the scraped file from bloating to $\approx 4GB$ for full-scale GEMs, albeit at the expense of slightly longer computational time. An alternative is to acquire a local version of the database and then assemble kinetics files for each organism with orders-of-magnitude greater efficiency.

Bibliography

[1] J. Laghari. "Melting glaciers bring energy uncertainty". In: *Nature* 502 (2013), pp. 617–618. URL: https://www.nature.com/polopoly_fs/1.14031!/menu/main/topColumns/topLeftColumn/pdf/502617a.pdf.

[2] Ghulam Rasul, Qin Dahe, and Q Z Chaudhry. "Global Warming and Melting Glaciers along Southern Slopes of HKH Ranges". In: *Pakistan Journal of Meteorology* 5.9 (2008), pp. 63–76.

[3] Igor A. Shiklomanov. "World fresh water resources". In: *Water in Crisis: A guide to the world's fresh water resources*. Oxford University Press, 1993. Chap. 2, pp. 13–24. DOI: 10.2307/2623756.

[4] James Hansen et al. "Global temperature change". In: *Proceedings of the National Academy of Sciences of the United States of America* 103.39 (2006), pp. 14288–14293. ISSN: 00278424. DOI: 10.1073/pnas.0606291103.

[5] IPCC. *Global Warming of 1.5°C*. 2018. URL: https://report.ipcc.ch/sr15/pdf/sr15_spm_final.pdf%0Ahttp://www.ipcc.ch/report/sr15/.

[6] Chris D. Thomas et al. "Extinction risk from climate change". In: *Nature* 427.6970 (2004), pp. 145–148. ISSN: 00280836. DOI: 10.1038/nature02121.

[7] Dimitrios Pappas and Konstantinos J. Chalvatzis. "Energy and Industrial Growth in India: The Next Emissions Superpower?" In: *Energy Procedia* 105 (2017), pp. 3656–3662. ISSN: 18766102. DOI: 10.1016/j.egypro.2017.03.842. URL: http://dx.doi.org/10.1016/j.egypro.2017.03.842.

[8] Xingrong Zhao, Xi Zhang, and Shuai Shao. "Decoupling CO2 emissions and industrial growth in China over 1993–2013: The role of investment". In: *Energy Economics* 60 (2016), pp. 275–292. ISSN: 01409883. DOI: 10.1016/j.eneco.2016.10.008. URL: http://dx.doi.org/10.1016/j.eneco.2016.10.008.

[9] Axel Möller et al. "Distribution and sources of polyfluoroalkyl substances (PFAS) in the River Rhine watershed". In: *Environmental Pollution* 158.10 (2010), pp. 3243–3250. ISSN: 02697491. DOI: 10.1016/j.envpol.2010.07.019. URL: http://dx.doi.org/10.1016/j.envpol.2010.07.019.

[10] John Bongaarts. "Human population growth and the demographic transition". In: *Philosophical Transactions of the Royal Society B: Biological Sciences* 364.1532 (2009), pp. 2985–2990. ISSN: 14712970. DOI: 10.1098/rstb.2009.0137.

[11] William B. Meyer and B. L. Turner II. "Human population growth and global land-use/cover change". In: *Annual Review of Ecology and Systematics* 23.1 (1992), pp. 39–61. ISSN: 00664162. DOI: 10.1146/annurev.es.23.110192.000351.

[12] Unicef. *Thirsting for a Future: Water and children in a changing climate*. 2017, pp. 1–80. ISBN: 9789280648744. URL: www.unicef.org/wash/waterandclimate.

[13] Arjen Y. Hoekstra et al. "Global monthly water scarcity: Blue water footprints versus blue water availability". In: *PLoS ONE* 7.2 (2012). ISSN: 19326203. DOI: 10.1371/journal.pone.0032688.

[14] Edward Jones et al. "The state of desalination and brine production: A global outlook". In: *Science of the Total Environment* 657 (2018), pp. 1343–1356. ISSN: 18791026. DOI: 10.1016/j.scitotenv.2018.12.076. URL: https://doi.org/10.1016/j.scitotenv.2018.12.076.

[15] *Department of energy announces $100 million energy-water desalination hub to secure and affordable water*. 2018. URL: https://www.energy.gov/articles/department-energy-announces-100-million-energy-water-desalination-hub-provide-secure-and.

[16] R. F. Service. "Desalination Freshens Up". In: *Science* 313.5790 (2006), pp. 1088–1090. ISSN: 0036-8075. DOI: 10.1126/science.313.5790.1088.

[17] Gary Amy et al. "Membrane-based seawater desalination: Present and future prospects". In: *Desalination* 401 (2017), pp. 16–21. ISSN: 00119164. DOI: 10.1016/j.desal.2016.10.002. URL: http://dx.doi.org/10.1016/j.desal.2016.10.002.

[18] M. F.A. Goosen et al. "Fouling of reverse osmosis and ultrafiltration membranes: A critical review". In: *Separation Science and Technology* 39.10 (2004), pp. 2261–2297. ISSN: 01496395. DOI: 10.1081/SS-120039343.

[19] David M. Warsinger et al. "Scaling and fouling in membrane distillation for desalination applications: A review". In: *Desalination* 356 (2015), pp. 294–313. ISSN: 00119164. DOI: 10.1016/j.desal.2014.06.031. URL: http://dx.doi.org/10.1016/j.desal.2014.06.031.

[20] Muhammad Tariq Khan et al. "Source water quality shaping different fouling scenarios in a full-scale desalination plant at the Red Sea". In: *Water Research* 47.2 (2013), pp. 558–568. ISSN: 18792448. DOI: 10.1016/j.watres.2012.10.017.

[21] Fang Tang et al. "Fouling of reverse osmosis membrane for municipal wastewater reclamation: Autopsy results from a full-scale plant". In: *Desalination* 349 (2014), pp. 73–79. ISSN: 00119164. DOI: 10.1016/j.desal.2014.06.018. URL: http://dx.doi.org/10.1016/j.desal.2014.06.018.

[22] Marina Shmulevsky et al. “Analysis of the onset of calcium sulfate scaling on RO membranes”. In: *Journal of Membrane Science* 524.November 2016 (2017), pp. 299–304. ISSN: 18733123. DOI: 10.1016/j.memsci.2016.11.055. URL: http://dx.doi.org/10.1016/j.memsci.2016.11.055.

[23] W. G. Characklis and K. E. Cooksey. “Biofilms and Microbial Fouling”. In: *Advances in Applied Microbiology* 29.C (1983), pp. 93–138. ISSN: 00652164. DOI: 10.1016/S0065-2164(08)70355-1.

[24] Hans-Cur Flemming. *Reverse Osmosis Membrane Biofouling*. 1997. URL: https://scholar.google.com/scholar?as_vis=0&q=reverse+osmosis+membrane+technology+amjad+ed&hl=en&as_sdt=0,47.

[25] H. F. Ridgway and J. Safarik. “Biofouling of Reverse Osmosis Membranes”. In: *Biofouling and Biocorrosion in Industrial Water Systems* (1991), pp. 81–111. DOI: 10.1007/978-3-642-76543-8{_}5.

[26] H. Ivnitsky et al. “Characterization of membrane biofouling in nanofiltration processes of wastewater treatment”. In: *Desalination* 185.1-3 (2005), pp. 255–268. ISSN: 00119164. DOI: 10.1016/j.desal.2005.03.081.

[27] Moshe Herzberg and Menachem Elimelech. “Biofouling of reverse osmosis membranes: Role of biofilm-enhanced osmotic pressure”. In: *Journal of Membrane Science* 295.1-2 (2007), pp. 11–20. ISSN: 03767388. DOI: 10.1016/j.memsci.2007.02.024.

[28] R. P. Schneider et al. “Dynamics of organic carbon and of bacterial populations in a conventional pretreatment train of a reverse osmosis unit experiencing severe biofouling”. In: *Journal of Membrane Science* 266.1-2 (2005), pp. 18–29. ISSN: 03767388. DOI: 10.1016/j.memsci.2005.05.006.

[29] H Flemming et al. “Biofouling - the Achilles heel of membrane processes”. In: *Desalination* 113 (1997), pp. 215–225.

[30] P. A. Cantor and B. J. Mechalas. “Biological degradation of cellulose acetate reverse-osmosis membranes”. In: *Journal of Polymer Science Part C: Polymer Symposia* 28.1 (1969), pp. 225–241. DOI: 10.1002/polc.5070280119.

[31] Andrew P. Murphy et al. “Microbiological damage of cellulose acetate RO membranes”. In: *Journal of Membrane Science* 193.1 (2001), pp. 111–121. ISSN: 03767388. DOI: 10.1016/S0376-7388(01)00506-3.

[32] C. L. Chen et al. “Community structure of microbial biofilms associated with membrane-based water purification processes as revealed using a polyphasic approach”. In: *Applied Microbiology and Biotechnology* 63.4 (2004), pp. 466–473. ISSN: 01757598. DOI: 10.1007/s00253-003-1286-7.

[33] Pablo García-Triñanes, Makrina A. Chairopoulou, and Luiza C. Campos. “Investigating reverse osmosis membrane fouling and scaling by membrane autopsy of a bench scale device”. In: *Environmental Technology (United Kingdom)* 0.0 (2021), pp. 1–14. ISSN: 1479487X. DOI: 10.1080/09593330.2021.1918262. URL: https://doi.org/10.1080/09593330.2021.1918262.

[34] S. R. Suwarno et al. "Biofouling in reverse osmosis processes: The roles of flux, crossflow velocity and concentration polarization in biofilm development". In: *Journal of Membrane Science* 467 (2014), pp. 116–125. ISSN: 18733123. DOI: 10.1016/j.memsci.2014.04.052.

[35] Laurence Strubbe. "Calibration of a Reverse Osmosis Model At Full-Scale". In: (2018).

[36] Dooil Kim et al. "Biocide application for controlling biofouling of SWRO membranes - an overview". In: *Desalination* 238.1-3 (2009), pp. 43–52. ISSN: 00119164. DOI: 10.1016/j.desal.2008.01.034. URL: http://dx.doi.org/10.1016/j.desal.2008.01.034.

[37] Luiz H. Da-Silva-Correa et al. "The application of non-oxidizing biocides to prevent biofouling in reverse osmosis polyamide membrane systems: a review". In: *Journal of Water Supply: Research and Technology-Aqua* 00.0 (2022), pp. 1–32. ISSN: 0003-7214. DOI: 10.2166/aqua.2022.118.

[38] Samantha Eslava Martins et al. "Review: Ecotoxicity of organic and organo-metallic antifouling co-biocides and implications for environmental hazard and risk assessments in aquatic ecosystems". In: *Biofouling* 34.1 (2018), pp. 34–52. ISSN: 10292454. DOI: 10.1080/08927014.2017.1404036. URL: http://doi.org/10.1080/08927014.2017.1404036.

[39] Kevin V. Thomas et al. "Antifouling paint booster biocides in the UK coastal environment and potential risks of biological effects". In: *Marine Pollution Bulletin* 42.8 (2001), pp. 677–688. ISSN: 0025326X. DOI: 10.1016/S0025-326X(00)00216-2.

[40] Heather L. Buckley et al. "Design and Testing of Safer, More Effective Preservatives for Consumer Products". In: *ACS Sustainable Chemistry and Engineering* 5.5 (2017), pp. 4320–4331. ISSN: 21680485. DOI: 10.1021/acssuschemeng.7b00374.

[41] H. Winters et al. "Control of biological fouling in seawater reverse osmosis desalination". In: *Desalination* 47 (1983), pp. 233–238. ISSN: 1098-6596.

[42] Jim O'Neill. *Antimicrobial Resistance: Tackling a crisis for the health and wealth of nations*. Tech. rep. December. 2014.

[43] A. I. Radu et al. "A two-dimensional mechanistic model for scaling in spiral wound membrane systems". In: *Chemical Engineering Journal* 241 (2014), pp. 77–91. ISSN: 13858947. DOI: 10.1016/j.cej.2013.12.021. URL: http://dx.doi.org/10.1016/j.cej.2013.12.021.

[44] A. I. Radu et al. "Modeling the effect of biofilm formation on reverse osmosis performance: Flux, feed channel pressure drop and solute passage". In: *Journal of Membrane Science* 365.1-2 (2010), pp. 1–15. ISSN: 03767388. DOI: 10.1016/j.memsci.2010.07.036. URL: http://dx.doi.org/10.1016/j.memsci.2010.07.036.

[45] Maryam Bagheri, Sayed Amir Marashi, and Mohammad Ali Amoozegar. "A genome-scale metabolic network reconstruction of extremely halophilic bacterium Salinibacter ruber". In: *PLoS ONE* 14.5 (2019), pp. 1–17. ISSN: 19326203. DOI: 10.1371/journal.pone.0216336.

[46] Lilian Malaeb and George M. Ayoub. "Reverse osmosis technology for water treatment: State of the art review". In: *Desalination* 267.1 (2011), pp. 1–8. ISSN: 00119164. DOI: 10.1016/j.desal.2010.09.001. URL: http://dx.doi.org/10.1016/j.desal.2010.09.001.

[47] Hilla Shemer and Raphael Semiat. "Sustainable RO desalination – Energy demand and environmental impact". In: *Desalination* 424.September (2017), pp. 10–16. ISSN: 00119164. DOI: 10.1016/j.desal.2017.09.021. URL: http://dx.doi.org/10.1016/j.desal.2017.09.021.

[48] US-Saudi Business Council. *Water in Saudi Arabia: Desalination, Wastewater, and Privatization.* 2021. URL: https://ussaudi.org/water-in-saudi-arabia-desalination-wastewater-and-privatization/.

[49] Mohamed Karime, S. Bouguecha, and B. Hamrouni. "RO membrane autopsy of Zarzis brackish water desalination plant". In: *Desalination* 220.1-3 (2008), pp. 258–266. ISSN: 00119164. DOI: 10.1016/j.desal.2007.02.040.

[50] Azza Hafez and Samir El-Manharawy. "Economics of seawater RO desalination in the Red Sea region, Egypt. Part 1. A case study". In: *Desalination* 153.1-3 (2003), pp. 335–347. ISSN: 00119164. DOI: 10.1016/S0011-9164(02)01122-0.

[51] Menachem Elimelech and William A. Phillip. "The future of seawater desalination: Energy, technology, and the environment". In: *Science* 333.6043 (2011), pp. 712–717. ISSN: 00368075. DOI: 10.1126/science.1200488.

[52] Raphael Semiat. "Energy issues in desalination processes". In: *Environmental Science and Technology* 42.22 (2008), pp. 8193–8201. ISSN: 0013936X. DOI: 10.1021/es801330u.

[53] Domingo Zarzo and Daniel Prats. "Desalination and energy consumption. What can we expect in the near future?" In: *Desalination* 427.November 2017 (2018), pp. 1–9. ISSN: 00119164. DOI: 10.1016/j.desal.2017.10.046. URL: http://dx.doi.org/10.1016/j.desal.2017.10.046.

[54] Elizabeth M. Van Wagner et al. "Effect of crossflow testing conditions, including feed pH and continuous feed filtration, on commercial reverse osmosis membrane performance". In: *Journal of Membrane Science* 345.1-2 (2009), pp. 97–109. ISSN: 03767388. DOI: 10.1016/j.memsci.2009.08.033.

[55] S. Belfer et al. "Surface modification of commercial composite polyamide reverse osmosis membranes". In: *Journal of Membrane Science* 139.2 (1998), pp. 175–181. ISSN: 03767388. DOI: 10.1016/S0376-7388(97)00248-2.

[56] Yolanda Fernández-torquemada et al. "Dispersion of brine discharge from seawater reverse osmosis desalination plants". In: *Desalination and Water Treatment* 5.1-3 (2012), pp. 137–145.

[57] Howard P Clemens and Woodrow H Jones. "Toxicity of Brine Water from Oil Wells". In: March 2014 (1955), pp. 37–41. DOI: 10.1577/1548-8659(1954)84.

[58] Thomas F Allen and David G Austin. *Apparatus and method for processing oil well brine.* 1989.

[59] David A. Munn and Raymond Stewart. "Effect of Oil Well Brine on Germination and Seedling Growth of Several Crops". In: *The Ohio Journal of Science* 89.4 (1989), pp. 92–94. ISSN: 0030-0950. URL: http://hdl.handle.net/1811/23326.

[60] Joseph C. Allen. *Process for recovering iodine from oil well brine*. 1954. DOI: 10.1145/178951.178972.

[61] Donald M Fenton. *Desalination of brackish water or brine from hydrocarbon wells*. 1992.

[62] T. Jeppesen et al. "Metal recovery from reverse osmosis concentrate". In: *Journal of Cleaner Production* 17.7 (2009), pp. 703–707. ISSN: 09596526. DOI: 10.1016/j.jclepro.2008.11.013. URL: http://dx.doi.org/10.1016/j.jclepro.2008.11.013.

[63] Musthafa O. Mavukkandy et al. "Brine management in desalination industry: From waste to resources generation". In: *Desalination* 472.September (2019), p. 114187. ISSN: 00119164. DOI: 10.1016/j.desal.2019.114187. URL: https://doi.org/10.1016/j.desal.2019.114187.

[64] Meng Ye et al. *Charge-Free Mixing Entropy Battery Enabled by Low-Cost Electrode Materials*. 2019. DOI: 10.1021/acsomega.9b00863.

[65] A. J. Karabelas, A. Karanasiou, and S. T. Mitrouli. "Incipient membrane scaling by calcium sulfate during desalination in narrow spacer-filled channels". In: *Desalination* 345 (2014), pp. 146–157. ISSN: 00119164. DOI: 10.1016/j.desal.2014.04.020. URL: http://dx.doi.org/10.1016/j.desal.2014.04.020.

[66] David M. Warsinger et al. "Inorganic fouling mitigation by salinity cycling in batch reverse osmosis". In: *Water Research* 137 (2018), pp. 384–394. ISSN: 18792448. DOI: 10.1016/j.watres.2018.01.060. URL: https://doi.org/10.1016/j.watres.2018.01.060.

[67] Jeffrey R. McCutcheon and Menachem Elimelech. "Influence of concentrative and dilutive internal concentration polarization on flux behavior in forward osmosis". In: *Journal of Membrane Science* 284.1-2 (2006), pp. 237–247. ISSN: 03767388. DOI: 10.1016/j.memsci.2006.07.049.

[68] Z. V.P. Murthy and Sharad K. Gupta. "Estimation of mass transfer coefficient using a combined nonlinear membrane transport and film theory model". In: *Desalination* 109.1 (1997), pp. 39–49. ISSN: 00119164. DOI: 10.1016/S0011-9164(97)00051-9.

[69] M. F. Gruber et al. "Computational fluid dynamics simulations of flow and concentration polarization in forward osmosis membrane systems". In: *Journal of Membrane Science* 379.1-2 (2011), pp. 488–495. ISSN: 03767388. DOI: 10.1016/j.memsci.2011.06.022. URL: http://dx.doi.org/10.1016/j.memsci.2011.06.022.

[70] Ss Sablani et al. "Concentration polarization in ultrafiltration and reverse osmosis: A critical review". In: *Desalination* 141.3 (2001), pp. 269–289. ISSN: 00119164. DOI: 10.1016/S0011-9164(01)85005-0.

[71] Andrew L. Zydney. "Stagnant film model for concentration polarization in membrane systems". In: *Journal of Membrane Science* 130.1-2 (1997), pp. 275–281. ISSN: 03767388. DOI: 10.1016/S0376-7388(97)00006-9.

[72] Mingheng Li, Thanh Bui, and Steven Chao. "Three-dimensional CFD analysis of hydrodynamics and concentration polarization in an industrial RO feed channel". In: *Desalination* 397 (2016), pp. 194–204. ISSN: 00119164. DOI: 10.1016/j.desal.2016.07.005. URL: http://dx.doi.org/10.1016/j.desal.2016.07.005.

[73] Bastian E. Rapp. "Fluids". In: *Microfluidics: Modeling, Mechanics and Mathematics*. ScienceDirect, 2017. Chap. 9, pp. 273–276. ISBN: 9781139628808. DOI: 10.1017/CBO9781139628808.025.

[74] Zhixin Hu et al. "Real-time monitoring of scale formation in reverse osmosis using electrical impedance spectroscopy". In: *Journal of Membrane Science* 453 (2014), pp. 320–327. ISSN: 18733123. DOI: 10.1016/j.memsci.2013.11.014. URL: http://dx.doi.org/10.1016/j.memsci.2013.11.014.

[75] F. H. Butt, F. Rahman, and U. Baduruthamal. "Identification of scale deposits through membrane autopsy". In: *Desalination* 101.3 (1995), pp. 219–230. ISSN: 00119164. DOI: 10.1016/0011-9164(95)00025-W.

[76] R. Sheikholeslami and H. W.K. Ong. "Kinetics and thermodynamics of calcium carbonate and calcium sulfate at salinities up to 1.5 M". In: *Desalination* 157.1-3 (2003), pp. 217–234. ISSN: 00119164. DOI: 10.1016/S0011-9164(03)00401-6.

[77] Ronald N. Giere. "Is computer simulation changing the face of experimentation?" In: *Philosophical Studies* 143.1 (2009), pp. 59–62. ISSN: 00318116. DOI: 10.1007/s11098-008-9314-1.

[78] J. G. Wijmans and R. W. Baker. "The solution-diffusion model: a review". In: *Journal of Membrane Science* 107 (1995), pp. 1–21. ISSN: 01664115.

[79] Johannes Lenhard. "Computer simulation: The cooperation between experimenting and modeling". In: *Philosophy of Science* 74.2 (2007), pp. 176–194. ISSN: 00318248. DOI: 10.1086/519029.

[80] G. Y. Chai, A. R. Greenberg, and W. B. Krantz. "Ultrasound, gravimetric, and SEM studies of inorganic fouling in spiral-wound membrane modules". In: *Desalination* 208.1-3 (2007), pp. 277–293. ISSN: 00119164. DOI: 10.1016/j.desal.2006.06.018.

[81] *Zero Brine D2 . 1 Modelling a brine regeneration cycle using PHREEQC*. Tech. rep. August. European Union's Horizon 2020 Research, 2018.

[82] Desalitech. *ROSA membrane projection software*. URL: https://www.desalitech.com/rosa_download_lp/.

[83] Kok Pol Chee et al. "Performance Evaluation of Reverse Osmosis Desalination Pilot Plants using ROSA Simulation Software". In: *E3S Web of Conferences* 65 (2018). ISSN: 22671242. DOI: 10.1051/e3sconf/20186505022.

[84] SysCAD. *PHREEQC Reverse Osmosis Unit*. 2020. URL: https://help.syscad.net/index.php/PHREEQC_Reverse_Osmosis_Unit.

[85] Abderrezak Bouchareb, Mehdi Metaiche, and Hakim Lounici. "Experimental versus theoretical study of reverse osmosis pilot scaling: The case of Algerian brackish water desalination". In: *Journal of Water and Land Development* 42.1 (2019), pp. 49–58. ISSN: 20834535. DOI: 10.2478/jwld-2019-0044.

[86] Tianfu Xu et al. *TOUGHREACT User' s Guide : A Simulation Program for Non-isothermal Multiphase Reactive Transport in Variably Saturated Geologic Media , Version 2 .0*. Tech. rep. Lawrence Berkeley National Laboratory, 2012.

[87] C. I. Steefel et al. "Reactive transport codes for subsurface environmental simulation". In: *Computational Geosciences* 19.3 (2015), pp. 445–478. ISSN: 15731499. DOI: 10.1007/s10596-014-9443-x.

[88] Prodip Kundu. *Technical basis for OLI membrane technology*. Tech. rep. May. OLI Systems, 2018.

[89] P. Walker and R. Sheikholeslami. "Assessment of the effect of velocity and residence time in CaSO4 precipitating flow reaction". In: *Chemical Engineering Science* 58.16 (2003), pp. 3807–3816. ISSN: 00092509. DOI: 10.1016/S0009-2509(03)00268-9.

[90] A. J. Karabelas et al. "Prediction of spatial-temporal evolution of membrane scaling in spiral wound desalination modules by an advanced simulator". In: *Desalination* 458.January (2019), pp. 34–44. ISSN: 00119164. DOI: 10.1016/j.desal.2019.01.027. URL: https://doi.org/10.1016/j.desal.2019.01.027.

[91] French Creek Software. *Reverse Osmosis*. URL: https://www.frenchcreeksoftware.com/.

[92] NAWI. *WaterTap*. 2021. URL: https://github.com/watertap-org/watertap.

[93] David L. Parkhurst and Laurin Wissmeier. "PhreeqcRM: A reaction module for transport simulators based on the geochemical model PHREEQC". In: *Advances in Water Resources* 83 (2015), pp. 176–189. ISSN: 03091708. DOI: 10.1016/j.advwatres.2015.06.001. URL: http://dx.doi.org/10.1016/j.advwatres.2015.06.001.

[94] Scott R. Charlton and David L. Parkhurst. "Modules based on the geochemical model PHREEQC for use in scripting and programming languages". In: *Computers and Geosciences* 37.10 (2011), pp. 1653–1663. ISSN: 00983004. DOI: 10.1016/j.cageo.2011.02.005. URL: http://dx.doi.org/10.1016/j.cageo.2011.02.005.

[95] S. T. Mitrouli, M. Kostoglou, and A. J. Karabelas. "Calcium carbonate scaling of desalination membranes: Assessment of scaling parameters from dead-end filtration experiments". In: *Journal of Membrane Science* 510 (2016), pp. 293–305. ISSN: 18733123. DOI: 10.1016/j.memsci.2016.02.061. URL: http://dx.doi.org/10.1016/j.memsci.2016.02.061.

[96] Amos Bein and Alan R. Dutton. "Origin, distribution, and movement of brine in the Permian Basin (U.S.A.): A model for displacement of connate brine". In: *Geological Society of America Bulletin* June (1993), pp. 695–707.

[97] Timothy P. Wilson and David T. Long. "Geochemistry and isotope chemistry of Michigan Basin brines: Devonian formations". In: *Applied Geochemistry* 8.5 (1993), pp. 507–524. ISSN: 08832927. DOI: 10.1016/0883-2927(93)90079-V.

[98] S. Casas et al. "Seawater Reverse Osmosis Brines as a New Salt Source for the Chlor-Alkali Industry: Integration of NaCl Concentration by Electrodialysis". In: *Solvent Extraction and Ion Exchange* 30.4 (2012), pp. 322–332. ISSN: 07366299. DOI: 10.1080/07366299.2012.686849.

[99] Zhongsen Yan et al. "Reverse osmosis brine treatment using direct contact membrane distillation: Effects of feed temperature and velocity". In: *Desalination* 423.May (2017), pp. 149–156. ISSN: 00119164. DOI: 10.1016/j.desal.2017.09.010. URL: http://dx.doi.org/10.1016/j.desal.2017.09.010.

[100] A. J. Karabelas, S. T. Mitrouli, and M. Kostoglou. "Scaling in reverse osmosis desalination plants: A perspective focusing on development of comprehensive simulation tools". In: *Desalination* 474.November 2019 (2020), p. 114193. ISSN: 00119164. DOI: 10.1016/j.desal.2019.114193. URL: https://doi.org/10.1016/j.desal.2019.114193.

[101] Jui Sheng Chen et al. "Assessing the performance of a permeable reactive barrier–aquifer system using a dual-domain solute transport model". In: *Journal of Hydrology* 543 (2016), pp. 849–860. ISSN: 00221694. DOI: 10.1016/j.jhydrol.2016.11.002. URL: http://dx.doi.org/10.1016/j.jhydrol.2016.11.002.

[102] Courtney R. Scruggs et al. "The Dual-Domain Porosity Apparatus: Characterizing Dual Porosity at the Sediment/Water Interface". In: *Groundwater* 57.4 (2019), pp. 640–646. ISSN: 17456584. DOI: 10.1111/gwat.12846.

[103] Janek Greskowiak et al. "A benchmark for multi-rate surface complexation and 1D dual-domain multi-component reactive transport of U(VI)". In: *Computational Geosciences* 19.3 (2015), pp. 585–597. ISSN: 15731499. DOI: 10.1007/s10596-014-9457-4.

[104] John Mieles and Hongbin Zhan. "Analytical solutions of one-dimensional multispecies reactive transport in a permeable reactive barrier-aquifer system". In: *Journal of Contaminant Hydrology* 134-135 (2012), pp. 54–68. ISSN: 01697722. DOI: 10.1016/j.jconhyd.2012.04.002. URL: http://dx.doi.org/10.1016/j.jconhyd.2012.04.002.

[105] Nicolas Moës, Eric Béchet, and Matthieu Tourbier. "Imposing Dirichlet boundary conditions in the extended finite element method". In: *International Journal for Numerical Methods in Engineering* 67.12 (2006), pp. 1641–1669. ISSN: 00295981. DOI: 10.1002/nme.1675.

[106] Y. Bazilevs and T. J.R. Hughes. "Weak imposition of Dirichlet boundary conditions in fluid mechanics". In: *Computers and Fluids* 36.1 (2007), pp. 12–26. ISSN: 00457930. DOI: 10.1016/j.compfluid.2005.07.012.

[107] Moritz Gosses, Wolfgang Nowak, and Thomas Wöhling. "Explicit treatment for Dirichlet, Neumann and Cauchy boundary conditions in POD-based reduction of groundwater models". In: *Advances in Water Resources* 115 (2018), pp. 160–171. ISSN: 03091708. DOI: 10.1016/j.advwatres.2018.03.011. URL: https://doi.org/10.1016/j.advwatres.2018.03.011.

[108] Mingheng Li. "Optimal plant operation of brackish water reverse osmosis (BWRO) desalination". In: *Desalination* 293 (2012), pp. 61–68. ISSN: 00119164. DOI: 10.1016/j.desal.2012.02.024. URL: http://dx.doi.org/10.1016/j.desal.2012.02.024.

[109] G. Schock and A. Miquel. "Mass Transfer and pressure loss in spiral wound modules". In: *Desalination* 64 (1987), pp. 339–352.

[110] H. K. Lonsdale, U. Merten, and R. L. Riley. "Transport properties of cellulose acetate osmotic membranes". In: *Journal of Applied Polymer Science* 9.4 (1965), pp. 1341–1362. ISSN: 10974628. DOI: 10.1002/app.1965.070090413.

[111] M. A. McCaffrey, B. Lazar, and H. D. Holland. "The evaporation path of seawater and the coprecipitation of Br - and K + with halite." In: *Journal of Sedimentary Petrology,* 57.5 (1987), pp. 928–937. ISSN: 1527-1404. DOI: 10.1306/212f8cab-2b24-11d7-8648000102c1865d.

[112] Moti Kartashevsky, Raphael Semiat, and Carlos G. Dosoretz. "Phosphate adsorption on granular ferric hydroxide to increase product water recovery in reverse osmosis-desalination of secondary effluents". In: *Desalination* 364 (2015), pp. 53–61. ISSN: 00119164. DOI: 10.1016/j.desal.2015.02.038. URL: http://dx.doi.org/10.1016/j.desal.2015.02.038.

[113] Franco Evangelista. "A short cut method for the design of RO desalination plants". In: *Ind. Eng. Chem. Process Des. Dev.* 24 (1985), pp. 211–223. ISSN: 15388689.

[114] G. Srivathsan, Eph M. Sparrow, and John M. Gorman. "Reverse osmosis issues relating to pressure drop, mass transfer, turbulence, and unsteadiness". In: *Desalination* 341.1 (2014), pp. 83–86. ISSN: 00119164. DOI: 10.1016/j.desal.2014.02.021. URL: http://dx.doi.org/10.1016/j.desal.2014.02.021.

[115] Jianghang Gu et al. "Modeling of pressure drop in reverse osmosis feed channels using multilayer artificial neural networks". In: *Chemical Engineering Research and Design* 159 (2020), pp. 146–156. ISSN: 02638762. DOI: 10.1016/j.cherd.2020.04.019. URL: https://doi.org/10.1016/j.cherd.2020.04.019.

[116] Naum Fraidenraich et al. "Reverse osmosis desalination: Modeling and experiment". In: *Applied Physics Letters* 94 (2009), p. 124102. ISSN: 00036951. DOI: 10.1063/1.3109795.

[117] Muru S. Dandavati, Mahendra R. Doshi, and William N. Gill. "Hollow fiber reverse osmosis: experiments and analysis of radial flow systems". In: *Chemical Engineering Science* 30.8 (1975), pp. 877–886. ISSN: 00092509. DOI: 10.1016/0009-2509(75)80052-2.

[118] Nickolay Y. Gnedin, Vadim A. Semenov, and Andrey V. Kravtsov. "Enforcing the Courant–Friedrichs–Lew condition in explicitly conservative local time stepping schemes". In: *Journal of Computational Physics* 359 (2018), pp. 93–105. ISSN: 10902716. DOI: 10.1016/j.jcp.2018.01.008. URL: https://doi.org/10.1016/j.jcp.2018.01.008.

[119] Masuduz Zaman et al. "Downstream processing of reverse osmosis brine: Characterisation of potential scaling compounds". In: *Water Research* 80 (2015), pp. 227–234. ISSN: 18792448. DOI: 10.1016/j.watres.2015.05.004. URL: http://dx.doi.org/10.1016/j.watres.2015.05.004.

[120] Mushtaque Ahmed et al. "Brine disposal from reverse osmosis desalination plants in Oman and the United Arab Emirates". In: *Desalination* 133.2 (2001), pp. 135–147. ISSN: 00119164. DOI: 10.1016/S0011-9164(01)80004-7.

[121] Ferid Hajbi, Halim Hammi, and Adel M'Nif. "Reuse of RO desalination plant reject brine". In: *Journal of Phase Equilibria and Diffusion* 31.4 (2010), pp. 341–347. ISSN: 15477037. DOI: 10.1007/s11669-010-9727-3.

[122] Eric Lyster et al. "Coupled 3-D hydrodynamics and mass transfer analysis of mineral scaling-induced flux decline in a laboratory plate-and-frame reverse osmosis membrane module". In: *Journal of Membrane Science* 339.1-2 (2009), pp. 39–48. ISSN: 03767388. DOI: 10.1016/j.memsci.2009.04.024.

[123] Mooseok Lee and Jeonghwan Kim. "Membrane autopsy to investigate CaCO3 scale formation in pilot-scale, submerged membrane bioreactor treating calcium-rich wastewater". In: *Journal of Chemical Technology and Biotechnology* 84.9 (2009), pp. 1397–1404. ISSN: 02682575. DOI: 10.1002/jctb.2195.

[124] Kenneth S Pitzer. "Thermodynamics of electrolytes. I. Theoretical basis and general equations". In: *Journal of Physical Chemistry* 77.2 (1973), pp. 268–277. DOI: 10.1021/j100621a026.

[125] Kenneth S Pitzer and Janice J Kim. "Thermodynamics of Electrolytes . IV . Activity and Osmotic Coefficients for Mixed Electrolytes". In: *Journal of the American Chemical SOciety* 96.5701 (1974), pp. 413–419.

[126] C. A.C. Van de Lisdonk et al. "Prediction of supersaturation and monitoring of scaling in reverse osmosis and nanofiltration membrane systems". In: *Desalination* 138.1-3 (2001), pp. 259–270. ISSN: 00119164. DOI: 10.1016/S0011-9164(01)00272-7.

[127] R. Sheikholeslami. "Assessment of the scaling potential for sparingly soluble salts in RO and NF units". In: *Desalination* 167.1-3 (2004), pp. 247–256. ISSN: 00119164. DOI: 10.1016/j.desal.2004.06.134.

[128] A. W. Mohammad et al. "Prediction of permeate fluxes and rejections of highly concentrated salts in nanofiltration membranes". In: *Journal of Membrane Science* 289.1-2 (2007), pp. 40–50. ISSN: 03767388. DOI: 10.1016/j.memsci.2006.11.035.

[129] Ying Chen et al. "Sources and fluxes of atmospheric trace elements to the Gulf of Aqaba, Red Sea". In: *Journal of Geophysical Research* 113.5 (2008), pp. 1–13. ISSN: 01480227. DOI: 10.1029/2007JD009110.

[130] G. Sarthou and C. Jeandel. "Seasonal variations of iron concentrations in the Ligurian Sea and iron budget in the Western Mediterranean Sea". In: *Marine Chemistry* 74.2-3 (2001), pp. 115–129. ISSN: 03044203. DOI: 10.1016/S0304-4203(00)00119-5.

[131] John D. Hunter. "Matplotlib: A 2D graphics environment". In: *Computing in Science and Engineering* 9.3 (2007), pp. 99–104. ISSN: 15219615. DOI: 10.1109/MCSE.2007.55.

[132] Wes McKinney. *Pandas: a foundational Python library for data analysis and statistics*. Tech. rep. 2011. DOI: 10.1002/mmce.20381.

[133] *FilmTec ™ Membranes: FilmTec ™ BW30-400 high resolution, high surface area brackish water RO element*. Tech. rep. Du Pont, 2020, pp. 1–3.

[134] Federico A. Pacheco et al. "Characterization of isolated polyamide thin films of RO and NF membranes using novel TEM techniques". In: *Journal of Membrane Science* 358.1-2 (2010), pp. 51–59. ISSN: 03767388. DOI: 10.1016/j.memsci.2010.04.032. URL: http://dx.doi.org/10.1016/j.memsci.2010.04.032.

[135] Byeong Heon Jeong et al. "Interfacial polymerization of thin film nanocomposites: A new concept for reverse osmosis membranes". In: *Journal of Membrane Science* 294.1-2 (2007), pp. 1–7. ISSN: 03767388. DOI: 10.1016/j.memsci.2007.02.025.

[136] Shyam S. Sablani et al. "Influence of spacer thickness on permeate flux in spiral-wound seawater reverse osmosis systems". In: *Desalination* 146.1-3 (2002), pp. 225–230. ISSN: 00119164. DOI: 10.1016/S0011-9164(02)00477-0.

[137] Lars Göran Danielsson. "Cadmium, cobalt, copper, iron, lead, nickel and zinc in Indian Ocean water". In: *Marine Chemistry* 8.3 (1980), pp. 199–215. ISSN: 03044203. DOI: 10.1016/0304-4203(80)90010-9.

[138] V. Nisha and H. Achyuthan. "Geochemical evaluation of sea surface sediments along the continental shelf, south east coast of India". In: *Indian Journal of Geo-Marine Sciences* 43.2 (2014), pp. 241–251. ISSN: 03795136.

[139] V. Stephen-Pichaimani et al. "Enrichment of trace metals in surface sediments from the northern part of Point Calimere, SE coast of India". In: *Environmental Geology* 55.8 (2008), pp. 1811–1819. ISSN: 09430105. DOI: 10.1007/s00254-007-1132-9.

[140] K. Selvaraj, V. Ram Mohan, and Piotr Szefer. "Evaluation of metal contamination in coastal sediments of the Bay of Bengal, India: Geochemical and statistical approaches". In: *Marine Pollution Bulletin* 49.3 (2004), pp. 174–185. ISSN: 0025326X. DOI: 10.1016/j.marpolbul.2004.02.006.

[141] N. Thangadurai et al. "Pre-tsunami chemistry of sediments along the inner continental shelf off Ennore, Chennai, southeast coast of India". In: *Indian Journal of Marine Sciences* 34.3 (2005), pp. 274–278. ISSN: 03795136.

[142] S. M. Parvez Al-Usmani, T. G. Jagtap, and D. N. Patil. "Trace metals in water, sediment and bivalves of a tropical estuary, west coast of India". In: *Marine Pollution Bulletin* 99.1-2 (2015), pp. 328–331. ISSN: 18793363. DOI: 10.1016/j.marpolbul.2015.07.036. URL: http://dx.doi.org/10.1016/j.marpolbul.2015.07.036.

[143] Christopher L. Sabine et al. "Inorganic carbon in the Indian Ocean: Distribution and dissolution processes". In: *Global Biogeochemical Cycles* 16.4 (2002), pp. 15–1. ISSN: 0886-6236. DOI: 10.1029/2002gb001869.

[144] Satinder Pal Singh, Sunil Kumar Singh, and Ravi Bhushan. "Internal cycling of dissolved barium in water column of the Bay of Bengal". In: *Marine Chemistry* 154 (2013), pp. 12–23. ISSN: 03044203. DOI: 10.1016/j.marchem.2013.04.013. URL: http://dx.doi.org/10.1016/j.marchem.2013.04.013.

[145] Michael L. Bender and Christine Gagner. "Dissolved copper, nickel, and cadmium in the Sargasso Sea". In: *Journal of Marine Research* 34.3 (1976), pp. 327–339.

[146] Patricia Stoffyn-Egli and Fred T. Mackenzie. "Mass balance of dissolved lithium in the oceans". In: *Geochimica et Cosmochimica Acta* 48.4 (1984), pp. 859–872. ISSN: 00167037. DOI: 10.1016/0016-7037(84)90107-8.

[147] S. E. Calvert, T. F. Pedersen, and R. C. Thunell. "Geochemistry of the surface sediments of the Sulu and South China Seas". In: *Marine Geology* 114.3-4 (1993), pp. 207–231. ISSN: 00253227. DOI: 10.1016/0025-3227(93)90029-U.

[148] Liang Saw Wen, Kuo Tung Jiann, and Peter H. Santschi. "Physicochemical speciation of bioactive trace metals (Cd, Cu, Fe, Ni) in the oligotrophic South China Sea". In: *Marine Chemistry* 101.1-2 (2006), pp. 104–129. ISSN: 03044203. DOI: 10.1016/j.marchem.2006.01.005.

[149] Chuanjun Du et al. "Dynamics of dissolved inorganic carbon in the South China Sea: A modeling study". In: *Progress in Oceanography* 186.May (2020), p. 102367. ISSN: 00796611. DOI: 10.1016/j.pocean.2020.102367. URL: https://doi.org/10.1016/j.pocean.2020.102367.

[150] Chen Tung Arthur Chen et al. "Nutrient budgets for the South China sea basin". In: *Marine Chemistry* 75.4 (2001), pp. 281–300. ISSN: 03044203. DOI: 10.1016/S0304-4203(01)00041-X.

[151] Yuzuru Nakaguchi et al. "Dissolved selenium species in the Sulu Sea, the South China Sea and the Celebes Sea". In: *Geochemical Journal* 38.6 (2004), pp. 571–580. ISSN: 00167002. DOI: 10.2343/geochemj.38.571.

[152] R. Chester and F. G. Voutsinou. "The initial assessment of trace metal pollution in coastal sediments". In: *Marine Pollution Bulletin* 12.3 (1981), pp. 84–91. ISSN: 0025326X. DOI: 10.1016/0025-326X(81)90198-3.

[153] Fanny Voutsinou-Taliadouri and John Satsmadjis. "Distribution of heavy metals in sediments of the Patraikos gulf (Greece)". In: *Marine Pollution Bulletin* 14.1 (1983), pp. 33–35. ISSN: 0025326X. DOI: 10.1016/0025-326X(83)90094-2.

[154] Fanny Voutsinou-Taliadouri et al. "Dissolved trace elements in south Aegean seawater". In: *Marine Pollution Bulletin* 34.10 (1997), pp. 840–843. ISSN: 0025326X. DOI: 10.1016/S0025-326X(97)00070-2.

[155] Kazuo Fukushima, Toshiro Saino, and Yukio Kodama. "Trace metal contamination in Tokyo Bay, Japan". In: *Science of the Total Environment, The* 125.C (1992), pp. 373–389. ISSN: 00489697. DOI: 10.1016/0048-9697(92)90402-E.

[156] G. P. Hershelman et al. "Metals in marine sediments near a large California municipal outfall". In: *Marine Pollution Bulletin* 12.4 (1981), pp. 131–134. ISSN: 0025326X. DOI: 10.1016/0025-326X(81)90442-2.

[157] Samuel N. Luoma and D. J.H. Phillips. "Distribution, variability, and impacts of trace elements in San Francisco Bay". In: *Marine Pollution Bulletin* 19.9 (1988), pp. 413–425. ISSN: 0025326X. DOI: 10.1016/0025-326X(88)90396-7.

[158] Dondra V. Biller and Kenneth W. Bruland. "Sources and distributions of Mn, Fe, Co, Ni, Cu, Zn, and Cd relative to macronutrients along the central California coast during the spring and summer upwelling season". In: *Marine Chemistry* 155 (2013), pp. 50–70. ISSN: 03044203. DOI: 10.1016/j.marchem.2013.06.003. URL: http://dx.doi.org/10.1016/j.marchem.2013.06.003.

[159] D. H. Loring. "Geochemistry of Zinc, Copper and Lead in the Sediments of the Estuary and Gulf of St. Lawrence." In: *Can J Earth Sci* 15.5 (1978), pp. 757–772. DOI: 10.1139/e78-082.

[160] D. H. Loring. "Geochemistry of cobalt, nickel, chromium, and vanadium in the sediments of the estuary and open gulf of St. Lawrence". In: *Can J. Earth Sci.1* 16 (1979), pp. 1196–1209.

[161] P. A. Yeats and J. M. Bewers. "Potential Anthropogenic Influences on Trace Metal Distributions in the North Atlantic". In: *Canadian Journal of Fisheries and Aquatic Sciences* 40.s2 (1983), pp. 124–131. ISSN: 0706-652X. DOI: 10.1139/f83-318.

[162] M. H. Bothner, M. Buchholtz Ten Brink, and F. T. Manheim. "Metal concentrations in surface sediments of Boston Harbor - Changes with time". In: *Marine Environmental Research* 45.2 (1998), pp. 127–155. ISSN: 01411136. DOI: 10.1016/S0141-1136(97)00027-5.

[163] J. A. Campbell and D. H. Loring. "Baseline levels of heavy metals in the waters and sediments of Baffin Bay". In: *Marine Pollution Bulletin* 11.9 (1980), pp. 257–261. ISSN: 0025326x. DOI: 10.1016/0025-326X(80)90314-8.

[164] Camille Gaulier et al. "Trace metal speciation in North Sea coastal waters". In: *Science of the Total Environment* 692 (2019), pp. 701–712. ISSN: 18791026. DOI: 10.1016/j.scitotenv.2019.07.314. URL: https://doi.org/10.1016/j.scitotenv.2019.07.314.

[165] P. J. Statham and J. D. Burton. "Dissolved manganese in the North Atlantic Ocean, 0-35°N". In: *Earth and Planetary Science Letters* 79.1-2 (1986), pp. 55–65. ISSN: 0012821X. DOI: 10.1016/0012-821X(86)90040-3.

[166] Khairul N. Mohamed et al. "Dissolved iron(III) speciation in the high latitude North Atlantic Ocean". In: *Deep-Sea Research Part I: Oceanographic Research Papers* 58.11 (2011), pp. 1049–1059. ISSN: 09670637. DOI: 10.1016/j.dsr.2011.08.011. URL: http://dx.doi.org/10.1016/j.dsr.2011.08.011.

[167] C. K. Guay and K. Kenison Falkner. "A survey of dissolved barium in the estuaries of major Arctic rivers and adjacent seas". In: *Continental Shelf Research* 18.8 (1998), pp. 859–882. ISSN: 02784343. DOI: 10.1016/S0278-4343(98)00023-5.

[168] P. Szefer et al. "Distribution of selected metals in sediment cores of puck bay, Baltic Sea". In: *Marine Pollution Bulletin* 30.9 (1995), pp. 615–618. ISSN: 0025326X. DOI: 10.1016/0025-326X(95)00079-3.

[169] Klaus Kremling and Harald Petersen. "The distribution of Mn, Fe, Zn, Cd and Cu in Baltic seawater; a study on the basis of one anchor station". In: *Marine Chemistry* 6.2 (1978), pp. 155–170. ISSN: 03044203. DOI: 10.1016/0304-4203(78)90025-7.

[170] Iwao Tanita et al. "Surface and middle layer enrichment of dissolved copper in the western subarctic North Pacific". In: *Mer* 53.1-2 (2015), pp. 1–18. ISSN: 05031540.

[171] Nari Sim and Kristin J. Orians. "Annual variability of dissolved manganese in Northeast Pacific along Line-P: 2010–2013". In: *Marine Chemistry* 216.January (2019), p. 103702. ISSN: 03044203. DOI: 10.1016/j.marchem.2019.103702. URL: https://doi.org/10.1016/j.marchem.2019.103702.

[172] E. Boyle and J. M. Edmond. "Copper in surface waters south of New Zealand". In: *Nature* 253 (1975), pp. 107–109. ISSN: 0287-0223. DOI: 10.19004/pjssz.51.0{_}75{_}3.

[173] E. A. Boyle, F. Sclater, and J. M. Edmond. "On the marine geochemistry of cadmium". In: *Nature* 263 (1976), pp. 42–44. DOI: 10.19592/j.cnki.scje.2017.03.002.

[174] Dia Sotto Alibo and Yoshiyuki Nozaki. "Rare earth elements in seawater: Particle association, shale-normalization, and Ce oxidation". In: *Geochimica et Cosmochimica Acta* 63.3-4 (1999), pp. 363–372. ISSN: 00167037. DOI: 10.1016/S0016-7037(98)00279-8.

[175] G. Klinkhammer, H. Elderfield, and A. Hudson. "Rare earth elements in seawater near hydrothermal vents". In: *Nature* 305.5931 (1983), pp. 185–188. ISSN: 00280836. DOI: 10.1038/305185a0.

[176] Ester Garcia-Solsona et al. "Rare earth elements and Nd isotopes as tracers of modern ocean circulation in the central Mediterranean Sea". In: *Progress in Oceanography* 185.May 2019 (2020), p. 102340. ISSN: 00796611. DOI: 10.1016/j.pocean.2020.102340. URL: https://doi.org/10.1016/j.pocean.2020.102340.

[177] A. Longinelli and H. Craig. "Oxygen-18 Variations in sulfate ions in sea water and saline lakes". In: *Science* 156.3771 (1967), pp. 56–59.

[178] R. Michael Llyod. "Oxygen-18 Composition of Oceanic Sulfate". In: *Science* 156.3779 (1967), pp. 1228–1231. ISSN: 0036-8075. DOI: 10.1126/science.156.3779.1228.

[179] F. Culkin and R. A. Cox. "Sodium, potassium, magnesium, calcium and strontium in sea water". In: *Deep-Sea Research and Oceanographic Abstracts* 13.5 (1966), pp. 789–804. ISSN: 00117471. DOI: 10.1016/0011-7471(76)90905-0.

[180] B S Krumgalz. "Calcium distribution in the world ocean waters". In: *Oceanologica Acta* 5.1 (1982), pp. 121–128.

[181] Y. K. Kharaka et al. "Geochemistry of metal-rich brines from central Mississippi Salt Dome basin, U.S.A." In: *Applied Geochemistry* 2.5-6 (1987), pp. 543–561. ISSN: 08832927. DOI: 10.1016/0883-2927(87)90008-4.

[182] Aqion. *Activity Coefficients (Activity Models)*. 2016. URL: https://www.aqion.de/site/101.

[183] Cecill W. Davies. "The extent of dissolution of salts in water_Part VIII. An equation for the mean ionic acitivity coefficient of an electrolyte in water, and a revision of the dissociation constants of some sulphates". In: *The Royal Society of Chemistry* 0.1938 (1938), pp. 2093–2098. DOI: https://doi.org/10.1039/JR9380002093.

[184] Nayana G. Bhat and S. Balaji. "Whole-Cell Modeling and Simulation: A Brief Survey". In: *New Generation Computing* 38.1 (2020), pp. 259–281. ISSN: 18827055. DOI: 10.1007/s00354-019-00066-y. URL: https://doi.org/10.1007/s00354-019-00066-y.

[185] Masaru Tomita. "Whole-cell simulation: A grand challenge of the 21st century". In: *Trends in Biotechnology* 19.6 (2001), pp. 205–210. ISSN: 01677799. DOI: 10.1016/S0167-7799(01)01636-5.

[186] Bernhard Palsson. "The challenges of in silico biology". In: *Nature Biotechnology* 18.November (2000), pp. 1147–1150.

[187] Michael Feig and Yuji Sugita. "Whole-cell models and simulations in molecular detail". In: *Annual Review of Cell and Developmental Biology* 35 (2019), pp. 191–211. ISSN: 15308995. DOI: 10.1146/annurev-cellbio-100617-062542.

[188] Aarash Bordbar et al. *Personalized Whole-Cell Kinetic Models of Metabolism for Discovery in Genomics and Pharmacodynamics*. 2015. DOI: 10.1016/j.cels.2015.10.003.

[189] Joseph Loscalzo and Albert Laszlo Barabasi. "Systems biology and the future of medicine". In: *Wiley Interdisciplinary Reviews: Systems Biology and Medicine* 3.6 (2011), pp. 619–627. ISSN: 19395094. DOI: 10.1002/wsbm.144.

[190] Oliver Purcell et al. "Towards a whole-cell modeling approach for synthetic biology". In: *Chaos* 23.2 (2013). ISSN: 10541500. DOI: 10.1063/1.4811182.

[191] Christina L. Lewis, Caelli C. Craig, and Andre G. Senecal. "Mass and density measurements of live and dead gram-negative and gram-positive bacterial populations". In: *Applied and Environmental Microbiology* 80.12 (2014), pp. 3622–3631. ISSN: 10985336. DOI: 10.1128/AEM.00117-14.

[192] Stewart A. Adcock and J. Andrew McCammon. "Molecular dynamics: Survey of methods for simulating the activity of proteins". In: *Chemical Reviews* 106.5 (2006), pp. 1589–1615. ISSN: 00092665. DOI: 10.1021/cr040426m.

[193] Egbert Egberts, Siewert Jan Marrink, and Herman J.C. Berendsen. "Molecular dynamics simulation of a phospholipid membrane". In: *European Biophysics Journal* 22.6 (1994), pp. 423–436. ISSN: 01757571. DOI: 10.1007/BF00180163.

[194] Howard E. Alper, Donna Bassolino, and Terry R. Stouch. "Computer simulation of a phospholipid monolayer-water system: The influence of long range forces on water structure and dynamics". In: *The Journal of Chemical Physics* 98.12 (1993), pp. 9798–9807. ISSN: 00219606. DOI: 10.1063/1.464358.

[195] Howard E. Alper, Donna Bassolino-Klimas, and Terry R. Stouch. "The limiting behavior of water hydrating a phospholipid monolayer: A computer simulation study". In: *The Journal of Chemical Physics* 99.7 (1993), pp. 5547–5559. ISSN: 00219606. DOI: 10.1063/1.465947.

[196] Juan R. Perilla et al. "Molecular dynamics simulations of large macromolecular complexes". In: *Current Opinion in Structural Biology* 31 (2015), pp. 64–74. ISSN: 1879033X. DOI: 10.1016/j.sbi.2015.03.007. URL: http://dx.doi.org/10.1016/j.sbi.2015.03.007.

[197] Michael Feig et al. "Complete atomistic model of a bacterial cytoplasm for integrating physics, biochemistry, and systems biology". In: *Journal of Molecular Graphics and Modelling* 58 (2015), pp. 1–9. ISSN: 18734243. DOI: 10.1016/j.jmgm.2015.02.004. URL: http://dx.doi.org/10.1016/j.jmgm.2015.02.004.

[198] Jonathan R. Karr, Koichi Takahashi, and Akira Funahashi. "The principles of whole-cell modeling". In: *Current Opinion in Microbiology* 27 (2015), pp. 18–24. ISSN: 18790364. DOI: 10.1016/j.mib.2015.06.004. URL: http://dx.doi.org/10.1016/j.mib.2015.06.004.

[199] C. J. PERRET. "A New Kinetic Model of a Growing Bacterial Population". In: *Journal of General Microbiology* 22.3 (1960), pp. 589–617. ISSN: 0022-1287. DOI: 10.1099/00221287-22-3-589.

[200] Keehyun Han and Octave Levenspiel. "Extended monod kinetics for substrate, product, and cell inhibition". In: *Biotechnology and Bioengineering* 32.4 (1988), pp. 430–447. ISSN: 10970290. DOI: 10.1002/bit.260320404.

[201] Francis S. Collins, Michael Morgan, and Aristides Patrinos. "The Human Genome Project: Lessons from large-scale biology". In: *Science* 300.5617 (2003), pp. 286–290. ISSN: 00368075. DOI: 10.1126/science.1084564.

[202] Markus W. Covert et al. "Metabolic modeling of microbial strains in silico". In: *Trends in Biochemical Sciences* 26.3 (2001), pp. 179–186. ISSN: 09680004. DOI: 10.1016/S0968-0004(00)01754-0.

[203] A. Varma and B. O. Palsson. "Stoichiometric flux balance models quantitatively predict growth and metabolic by-product secretion in wild-type Escherichia coli W3110". In: *Applied and Environmental Microbiology* 60.10 (1994), pp. 3724–3731. ISSN: 00992240. DOI: 10.1128/aem.60.10.3724-3731.1994.

[204] J. S. Edwards and B. O. Palsson. "The Escherichia coli MG1655 in silico metabolic genotype: Its definition, characteristics, and capabilities". In: *Proceedings of the National Academy of Sciences of the United States of America* 97.10 (2000), pp. 5528–5533. ISSN: 00278424. DOI: 10.1073/pnas.97.10.5528.

[205] Jeremy S. Edwards, Rafael U. Ibarra, and Bernhard O. Palsson. "In silico predictions of Escherichia coli metabolic capabilities are consistent with experimental data". In: *Nature Biotechnology* 19.2 (2001), pp. 125–130. ISSN: 10870156. DOI: 10.1038/84379.

[206] Angela M. Gibson, N. Bratchell, and T. A. Roberts. "Predicting microbial growth: growth responses of salmonellae in a laboratory medium as affected by pH, sodium chloride and storage temperature". In: *International Journal of Food Microbiology* 6.2 (1988), pp. 155–178. ISSN: 01681605. DOI: 10.1016/0168-1605(88)90051-7.

[207] Jessica Sook Yuin Ho, Zeyu Zhu, and Ivan Marazzi. "Unconventional viral gene expression mechanisms as therapeutic targets". In: *Nature* 593.7859 (2021), pp. 362–371. ISSN: 14764687. DOI: 10.1038/s41586-021-03511-5. URL: http://dx.doi.org/10.1038/s41586-021-03511-5.

[208] Jeffrey D. Orth, Ines Thiele, and Bernhard O. Palsson. "What is flux balance analysis?" In: *Nature Biotechnology* 28.3 (2010), pp. 245–248. ISSN: 10870156. DOI: 10.1038/nbt.1614.

[209] Jong Min Lee, Erwin P. Gianchandani, and Jason A. Papin. "Flux balance analysis in the era of metabolomics". In: *Briefings in Bioinformatics* 7.2 (2006), pp. 140–150. ISSN: 14675463. DOI: 10.1093/bib/bbl007.

[210] Deepak Nagrath et al. "Soft constraints-based multiobjective framework for flux balance analysis". In: *Metabolic Engineering* 12.5 (2010), pp. 429–445. ISSN: 10967176. DOI: 10.1016/j.ymben.2010.05.003.

[211] Erwin P. Gianchandani, Arvind K. Chavali, and Jason A. Papin. "The application of flux balance analysis in systems biology". In: *Wiley Interdisciplinary Reviews: Systems Biology and Medicine* 2.3 (2010), pp. 372–382. ISSN: 19395094. DOI: 10.1002/wsbm.60.

[212] Steinn Gudmundsson and Ines Thiele. "Computationally efficient flux variability analysis". In: *BMC Bioinformatics* 11.2 (2010), pp. 2–4. ISSN: 14712105. DOI: 10.1186/1471-2105-11-489.

[213] Marcos Dantus, Mark J. Rosker, and Ahmed H. Zewail. "Real-time femtosecond probing of "transition states" in chemical reactions". In: *The Journal of Chemical Physics* 87.4 (1987), pp. 2395–2397. ISSN: 00219606. DOI: 10.1063/1.453122.

[214] Markus W. Covert et al. "Integrating metabolic, transcriptional regulatory and signal transduction models in Escherichia coli". In: *Bioinformatics* 24.18 (2008), pp. 2044–2050. ISSN: 13674803. DOI: 10.1093/bioinformatics/btn352.

[215] Sabine Peres et al. "How important is thermodynamics for identifying elementary flux modes?" In: *PLoS ONE* 12.2 (2017), pp. 1–20. ISSN: 19326203. DOI: 10.1371/journal.pone.0171440.

[216] Kenneth J. Kauffman, Purusharth Prakash, and Jeremy S. Edwards. "Advances in flux balance analysis". In: *Current Opinion in Biotechnology* 14.5 (2003), pp. 491–496. ISSN: 09581669. DOI: 10.1016/j.copbio.2003.08.001.

[217] R. M.T. Fleming et al. "Integrated stoichiometric, thermodynamic and kinetic modelling of steady state metabolism". In: *Journal of Theoretical Biology* 264.3 (2010), pp. 683–692. ISSN: 10958541. DOI: 10.1016/j.jtbi.2010.02.044. URL: http://dx.doi.org/10.1016/j.jtbi.2010.02.044.

[218] Stefanía Magnúsdóttir et al. "Generation of genome-scale metabolic reconstructions for 773 members of the human gut microbiota". In: *Nature Biotechnology* 35.1 (2017), pp. 81–89. ISSN: 15461696. DOI: 10.1038/nbt.3703.

[219] Christopher S. Henry, Linda J. Broadbelt, and Vassily Hatzimanikatis. "Thermodynamics-based metabolic flux analysis". In: *Biophysical Journal* 92.5 (2007), pp. 1792–1805. ISSN: 00063495. DOI: 10.1529/biophysj.106.093138.

[220] Nathan D. Price, Jennifer L. Reed, and Bernhard Ø Palsson. "Genome-scale models of microbial cells: evaluating the consequences of constraints". In: *Nature Reviews Microbiology* 2 (2004), pp. 886–897.

[221] Markus W. Covert, Christophe H. Schilling, and Bernhard Palsson. "Regulation of gene expression in flux balance models of metabolism". In: *Journal of Theoretical Biology* 213.1 (2001), pp. 73–88. ISSN: 00225193. DOI: 10.1006/jtbi.2001.2405.

[222] Daniel Machado et al. "Exploring the gap between dynamic and constraint-based models of metabolism". In: *Metabolic Engineering* 14.2 (2012), pp. 112–119. ISSN: 10967176. DOI: 10.1016/j.ymben.2012.01.003.

[223] Simone Pernice et al. "Integrating Petri Nets and Flux Balance Methods in Computational Biology Models: A Methodological and Computational Practice". In: *Fundamenta Informaticae* 171.1-4 (2019), pp. 367–392. ISSN: 01692968. DOI: 10.3233/FI-2020-1888.

[224] Radhakrishnan Mahadevan, Jeremy S. Edwards, and Francis J. Doyle. "Dynamic Flux Balance Analysis of diauxic growth in Escherichia coli". In: *Biophysical Journal* 83.3 (2002), pp. 1331–1340. ISSN: 00063495. DOI: 10.1016/S0006-3495(02)73903-9. URL: http://dx.doi.org/10.1016/S0006-3495(02)73903-9.

[225] R. Mahadevan and C. H. Schilling. "The effects of alternate optimal solutions in constraint-based genome-scale metabolic models". In: *Metabolic Engineering* 5.4 (2003), pp. 264–276. ISSN: 10967176. DOI: 10.1016/j.ymben.2003.09.002.

[226] Shomeek Chowdhury and Stephen S. Fong. "Leveraging genome-scale metabolic models for human health applications". In: *Current Opinion in Biotechnology* 66 (2020), pp. 267–276. ISSN: 18790429. DOI: 10.1016/j.copbio.2020.08.017. URL: https://doi.org/10.1016/j.copbio.2020.08.017.

[227] Ali R. Zomorrodi and Costas D. Maranas. "OptCom: A multi-level optimization framework for the metabolic modeling and analysis of microbial communities". In: *PLoS Computational Biology* 8.2 (2012). ISSN: 1553734X. DOI: 10.1371/journal.pcbi.1002363.

[228] Ruchir A. Khandelwal et al. "Community Flux Balance Analysis for Microbial Consortia at Balanced Growth". In: *PLoS ONE* 8.5 (2013). ISSN: 19326203. DOI: 10.1371/journal.pone.0064567.

[229] Saeed Shoaie et al. "Quantifying Diet-Induced Metabolic Changes of the Human Gut Microbiome". In: *Cell Metabolism* 22.2 (2015), pp. 320–331. ISSN: 19327420. DOI: 10.1016/j.cmet.2015.07.001.

[230] Manish Kumar et al. "Modelling approaches for studying the microbiome". In: *Nature Microbiology* 4.8 (2019), pp. 1253–1267. ISSN: 20585276. DOI: 10.1038/s41564-019-0491-9. URL: http://dx.doi.org/10.1038/s41564-019-0491-9.

[231] Patrick F. Suthers and Costas D. Maranas. "Challenges of cultivated meat production and applications of genome-scale metabolic modeling". In: *AIChE Journal* 66.6 (2020). ISSN: 15475905. DOI: 10.1002/aic.16235.

[232] Jörg Schwender. "Metabolic flux analysis as a tool in metabolic engineering of plants". In: *Current Opinion in Biotechnology* 19.2 (2008), pp. 131–137. ISSN: 09581669. DOI: 10.1016/j.copbio.2008.02.006.

[233] Doug K. Allen, Igor G.L. Libourel, and Yair Shachar-Hill. "Metabolic flux analysis in plants: Coping with complexity". In: *Plant, Cell and Environment* 32.9 (2009), pp. 1241–1257. ISSN: 01407791. DOI: 10.1111/j.1365-3040.2009.01992.x.

[234] Ingo Potrykus. "Golden Rice and Beyond International Society for Plant Molecular Biology 2000 Kumho Science International Award". In: *Society* 125.March (2001), pp. 1157–1161.

[235] Guangwen Tang et al. "Golden rice is an effective source of vitamin A". In: *American Journal of Clinical Nutrition* 89.6 (2009), pp. 1776–1783. ISSN: 00029165. DOI: 10.3945/ajcn.2008.27119.

[236] Nhung Pham et al. "Genome-scale metabolic modeling underscores the potential of Cutaneotrichosporon oleaginosus ATCC 20509 as a cell factory for biofuel production". In: *Biotechnology for Biofuels* 14.1 (2021), pp. 1–17. ISSN: 17546834. DOI: 10.1186/s13068-020-01838-1. URL: https://doi.org/10.1186/s13068-020-01838-1.

[237] Rebecca L Rubinstein et al. "ORT : A workflow linking genome-scale meta- bolic models with reactivace transport codes". In: *bioRXiv* (2021).

[238] Ilya A. Vakser and Eric J. Deeds. "Computational approaches to macromolecular interactions in the cell". In: *Current Opinion in Structural Biology* 55 (2019), pp. 59–65. ISSN: 1879033X. DOI: 10.1016/j.sbi.2019.03.012. URL: https://doi.org/10.1016/j.sbi.2019.03.012.

[239] Jonathan R. Karr et al. "WholeCellKB: Model organism databases for comprehensive whole-cell models". In: *Nucleic Acids Research* 41.D1 (2012), pp. 787–792. ISSN: 03051048. DOI: 10.1093/nar/gks1108.

[240] Michael Otto. "Staphylococcal Biofilms". In: *Microbiology Spectrum* 6.4 (2018). ISSN: 2165-0497. DOI: 10.1128/microbiolspec.gpp3-0023-2018.

[241] Marco G. Mazza. "The physics of biofilms - An introduction". In: *Journal of Physics D: Applied Physics* 49.20 (2016). ISSN: 13616463. DOI: 10.1088/0022-3727/49/20/203001.

[242] David Lebeaux, Jean-Marc Ghigo, and Christophe Beloin. "Biofilm-Related Infections: Bridging the Gap between Clinical Management and Fundamental Aspects of Recalcitrance toward Antibiotics". In: *Microbiology and Molecular Biology Reviews* 78.3 (2014), pp. 510–543. ISSN: 1092-2172. DOI: 10.1128/mmbr.00013-14.

[243] Daniel G. Metcalf and Philip G. Bowler. "Biofilm delays wound healing: A review of the evidence". In: *Burns and Trauma* 1.1 (2013), pp. 5–12. ISSN: 23213876. DOI: 10.4103/2321-3868.113329.

[244] Muhsin Jamal et al. "Bacterial biofilm and associated infections". In: *Journal of the Chinese Medical Association* 81.1 (2018), pp. 7–11. ISSN: 17287731. DOI: 10.1016/j.jcma.2017.07.012. URL: https://doi.org/10.1016/j.jcma.2017.07.012.

[245] Monil Singhai et al. "A study on device-related infections with special reference to biofilm production and antibiotic resistance". In: *Journal of Global Infectious Diseases* 4.4 (2012), pp. 193–198. ISSN: 0974777X. DOI: 10.4103/0974-777X.103896.

[246] Tom Coenye, Elke Peeters, and Hans J. Nelis. "Biofilm formation by Propionibacterium acnes is associated with increased resistance to antimicrobial agents and increased production of putative virulence factors". In: *Research in Microbiology* 158.4 (2007), pp. 386–392. ISSN: 09232508. DOI: 10.1016/j.resmic.2007.02.001.

[247] Rossella Baldan et al. "Adaptation of Pseudomonas aeruginosa in cystic fibrosis airways influences virulence of Staphylococcus aureus in vitro and murine models of co-infection". In: *PLoS ONE* 9.3 (2014). ISSN: 19326203. DOI: 10.1371/journal.pone.0089614.

[248] Andrea Kropec et al. "Poly-N-Acetylglucosamine production in Staphylococcus aureus is essential for virulence in murine models of systemic infection". In: *Infection and Immunity* 73.10 (2005), pp. 6868–6876. DOI: 10.1128/IAI.73.10.6868.

[249] C. Potera. "Forging a link between biofilms and disease". In: *Science* 283.5409 (1999), pp. 1837–1839. ISSN: 00368075. DOI: 10.1126/science.283.5409.1837.

[250] Matthew M. Ramsey and Marvin Whiteley. "Pseudomonas aeruginosa attachment and biofilm development in dynamic environments". In: *Molecular Microbiology* 53.4 (2004), pp. 1075–1087. ISSN: 0950382X. DOI: 10.1111/j.1365-2958.2004.04181.x.

[251] Philip S. Stewart. "Biophysics of biofilm infection". In: *Pathogens and Disease* 70.3 (2014), pp. 212–218. ISSN: 2049632X. DOI: 10.1111/2049-632X.12118.

[252] Moshe Herzberg and Menachem Elimelech. "Physiology and genetic traits of reverse osmosis membrane biofilms: A case study with Pseudomonas aeruginosa". In: *ISME Journal* 2.2 (2008), pp. 180–194. ISSN: 17517362. DOI: 10.1038/ismej.2007.108.

[253] Asif Matin et al. "Biofouling in reverse osmosis membranes for seawater desalination: Phenomena and prevention". In: *Desalination* 281.1 (2011), pp. 1–16. ISSN: 00119164. DOI: 10.1016/j.desal.2011.06.063.

[254] M. P. Schultz et al. "Economic impact of biofouling on a naval surface ship". In: *Biofouling* 27.1 (2011), pp. 87–98. ISSN: 08927014. DOI: 10.1080/08927014.2010.542809.

[255] *Chapter 1: The Effects Of fouling*. Tech. rep. US Naval Institute, 1952, pp. 3–19.

[256] S. E. Coetser and T. E. Cloete. "Biofouling and biocorrosion in industrial water systems". In: *Critical Reviews in Microbiology* 31.4 (2005), pp. 213–232. DOI: 10.1080/10408410500304074.

[257] Maureen E. Callow and James A. Callow. "Marine biofouling: A sticky problem". In: *Biologist* 49.1 (2002), pp. 10–14. ISSN: 00063347.

[258] K. Lewis. "Riddle of biofilm resistance". In: *Antimicrobial Agents and Chemotherapy* 45.4 (2001), pp. 999–1007. ISSN: 00664804. DOI: 10.1128/AAC.45.4.999-1007.2001.

[259] Cristiane Aparecida Pereira et al. "Susceptibility of Candida albicans, Staphylococcus aureus, and Streptococcus mutans biofilms to photodynamic inactivation: An in vitro study". In: *Lasers in Medical Science* 26.3 (2011), pp. 341–348. ISSN: 02688921. DOI: 10.1007/s10103-010-0852-3.

[260] P. A. Suci et al. "Investigation of ciprofloxacin penetration into Pseudomonas aeruginosa biofilms". In: *Antimicrobial Agents and Chemotherapy* 38.9 (1994), pp. 2125–2133. ISSN: 00664804. DOI: 10.1128/AAC.38.9.2125.

[261] B. D. Hoyle, J. Alcantara, and J. W. Costerton. "Pseudomonas aeruginosa biofilm as a diffusion barrier to piperacillin". In: *Antimicrobial Agents and Chemotherapy* 36.9 (1992), pp. 2054–2056. ISSN: 00664804. DOI: 10.1128/AAC.36.9.2054.

[262] M. W. LeChevallier, C. D. Cawthon, and R. G. Lee. "Inactivation of biofilm bacteria". In: *Applied and Environmental Microbiology* 54.10 (1988), pp. 2492–2499. ISSN: 00992240. DOI: 10.1128/aem.54.10.2492-2499.1988.

[263] W. M. Dunne, E. O. Mason, and S. L. Kaplan. "Diffusion of rifampin and vancomycin through a Staphylococcus epidermidis biofilm". In: *Antimicrobial Agents and Chemotherapy* 37.12 (1993), pp. 2522–2526. ISSN: 00664804. DOI: 10.1128/AAC.37.12.2522.

[264] D. De Beer, R. Srinivasan, and P. S. Stewart. "Direct measurement of chlorine penetration into biofilms during disinfection". In: *Applied and Environmental Microbiology* 60.12 (1994), pp. 4339–4344. ISSN: 00992240. DOI: 10.1128/aem.60.12.4339-4344.1994.

[265] Thien Fah C. Mah and George A. O'Toole. "Mechanisms of biofilm resistance to antimicrobial agents". In: *Trends in Microbiology* 9.1 (2001), pp. 34–39. ISSN: 0966842X. DOI: 10.1016/S0966-842X(00)01913-2.

[266] K. Sauer et al. "Characterization of nutrient-induced dispersion in Pseudomonas aeruginosa PAO1 biofilm". In: *Journal of Bacteriology* 186.21 (2004), pp. 7312–7326. ISSN: 00219193. DOI: 10.1128/JB.186.21.7312-7326.2004.

[267] Prashanth Suntharalingam and Dennis G. Cvitkovitch. "Quorum sensing in streptococcal biofilm formation". In: *Trends in Microbiology* 13.1 (2005), pp. 3–6. ISSN: 0966842X. DOI: 10.1016/j.tim.2004.11.009.

[268] Qi Wang and Tianyu Zhang. "Review of mathematical models for biofilms". In: *Solid State Communications* 150.21-22 (2010), pp. 1009–1022. ISSN: 00381098. DOI: 10.1016/j.ssc.2010.01.021. URL: http://dx.doi.org/10.1016/j.ssc.2010.01.021.

[269] Z Lewandowski. "4.15 Biofilms in Water and Wastewater Treatment". In: (2011).

[270] O. Wanner and W. Gujer. "A multispecies biofilm model". In: *Biotechnology and Bioengineering* 28.3 (1986), pp. 314–328. ISSN: 10970290. DOI: 10.1002/bit.260280304.

[271] S. K. Tiwari and K. L. Bowers. "Modeling biofilm growth for porous media applications". In: *Mathematical and Computer Modelling* 33.1-3 (2001), pp. 299–319. ISSN: 08957177. DOI: 10.1016/S0895-7177(00)00246-6.

[272] Sunil Kumar Tiwari. "Biofilm growth in a homogeneous porous medium". PhD thesis. Montana State University, 1997.

[273] Makram T. Suidan, Bruce E. Rittmann, and Ulrich K. Traegner. "Criteria establishing biofilm-kinetic types". In: *Water Research* 21.4 (1987), pp. 491–498. ISSN: 00431354. DOI: 10.1016/0043-1354(87)90198-9.

[274] Byung R. Kim and Makram T. Suidan. "Approximate algebraic solution for a biofilm model with the Monod kinetics expression". In: *Water Research* 23.12 (1989), pp. 1491–1498.

[275] César I. Torres et al. "Kinetic experiments for evaluating the nernst-monod model for anode-respiring bacteria (ARB) in a biofilm anode". In: *Environmental Science and Technology* 42.17 (2008), pp. 6593–6597. ISSN: 0013936X. DOI: 10.1021/es800970w.

[276] O. Wanner and W. Gujer. "Competition in biofilms". In: *Water Science and Technology* 17 (1984), pp. 27–44. ISSN: 02731223. DOI: 10.2166/wst.1994.0769.

[277] Vincent Gadani et al. "A new method to solve a non-steady-state multispecies biofilm model". In: *Bulletin of Mathematical Biology* 55.6 (1993), pp. 1039–1061. ISSN: 00928240. DOI: 10.1007/BF02460699.

[278] Jan Ulrich Kreft, Ginger Booth, and Julian W.T. Wimpenny. "BacSim, a simulator for individual-based modelling of bacterial colony growth". In: *Microbiology* 144.12 (1998), pp. 3275–3287. ISSN: 13500872. DOI: 10.1099/00221287-144-12-3275.

[279] Joao B. Xavier et al. "Biofilm-control strategies based on enzymic disruption of the extracellular polymeric substance matrix - A modelling study". In: *Microbiology* 151.12 (2005), pp. 3817–3832. ISSN: 13500872. DOI: 10.1099/mic.0.28165-0.

[280] Hidde De Jong et al. "Mathematical modelling of microbes: Metabolism, gene expression and growth". In: *Journal of the Royal Society Interface* 14.136 (2017). ISSN: 17425662. DOI: 10.1098/rsif.2017.0502.

[281] Pallab Barai, Aloke Kumar, and Partha P. Mukherjee. "Modeling of Mesoscale Variability in Biofilm Shear Behavior". In: *PLOS ONE* 11.11 (Nov. 2016). Ed. by Robert Nerenberg, e0165593. ISSN: 1932-6203. DOI: 10.1371/journal.pone.0165593. URL: https://dx.plos.org/10.1371/journal.pone.0165593.

[282] Chrysi S. Laspidou and Bruce E. Rittmann. "Evaluating trends in biofilm density using the UMCCA model". In: *Water Research* 38.14-15 (2004), pp. 3362–3372. ISSN: 00431354. DOI: 10.1016/j.watres.2004.04.051.

[283] C. S. Laspidou et al. "Material modeling of biofilm mechanical properties". In: *Mathematical Biosciences* 251.1 (2014), pp. 11–15. ISSN: 18793134. DOI: 10.1016/j.mbs.2014.02.007. URL: http://dx.doi.org/10.1016/j.mbs.2014.02.007.

[284] C. S. Laspidou, B. E. Rittmann, and S. A. Karamanos. "Finite element modeling to expand the UMCCA model to describe biofilm mechanical behavior". In: *Water Science and Technology* 52.7 (2005), pp. 161–166. ISSN: 02731223. DOI: 10.2166/wst.2005.0196.

[285] C. S. Laspidou, A. Kungolos, and P. Samaras. "Cellular-automata and individual-based approaches for the modeling of biofilm structures: Pros and cons". In: *Desalination* 250.1 (2010), pp. 390–394. ISSN: 00119164. DOI: 10.1016/j.desal.2009.09.062. URL: http://dx.doi.org/10.1016/j.desal.2009.09.062.

[286] Amal K. Das. "A non-Fickian diffusion equation". In: *Journal of Applied Physics* 1355.January 1991 (1991).

[287] Mallory R. Frederick et al. "A mathematical model of quorum sensing regulated EPS production in biofilm communities". In: *Theoretical Biology and Medical Modelling* 8.1 (2011), pp. 1–29. ISSN: 17424682. DOI: 10.1186/1742-4682-8-8.

[288] W. G. Characklis. "Microbial fouling : a process analysis." In: (1981), pp. 251–291.

[289] Christopher M. Waters and Bonnie L. Bassler. "QUORUM SENSING: Cell-to-Cell Communication in Bacteria". In: *Annual Review of Cell and Developmental Biology* 21.1 (2005), pp. 319–346. ISSN: 1081-0706. DOI: 10.1146/annurev.cellbio.21.012704.131001.

[290] Melissa B. Miller and Bonnie L. Bassler. "Quorem sensing in bacteria". In: *Annual Review of Microbiology* 55 (2001), pp. 165–199. ISSN: 87551039. DOI: 10.1002/dc.21368.

[291] Zbigniw Lewandowski, Gabriele Walser, and William G. Characklis. "Reaction kinetics in biofilms". In: *Biotechnology and Bioengineering* 38.8 (1991), pp. 877–882. ISSN: 10970290. DOI: 10.1002/bit.260380809.

[292] EGF Codons. *The software suite of the Edinburgh Genome Foundry*. 2021. URL: https://edinburgh-genome-foundry.github.io/.

[293] William Gilpin. "PyPDB: A Python API for the Protein Data Bank". In: *Bioinformatics* 32.1 (2016), pp. 159–160. ISSN: 14602059. DOI: 10.1093/bioinformatics/btv543.

[294] Statista. *Market share held by the leading computer (desktop/tablet/console) operating systems worldwide from January 2012 to December 2021*. URL: https://www.statista.com/statistics/268237/global-market-share-held-by-operating-systems-since-2009/.

[295] Ulrike Wittig et al. "SABIO-RK - Database for biochemical reaction kinetics". In: *Nucleic Acids Research* 40.D1 (2012), pp. 790–796. ISSN: 03051048. DOI: 10.1093/nar/gkr1046.

[296] Antje Chang et al. "BRENDA, the ELIXIR core data resource in 2021: New developments and updates". In: *Nucleic Acids Research* 49.D1 (2021), pp. D498–D508. ISSN: 13624962. DOI: 10.1093/nar/gkaa1025.

[297] *TIOBE index for February 2022*. URL: https://www.tiobe.com/tiobe-index/.

[298] Gunnar Sigurdsson et al. "A systems biology approach to drug targets in pseudomonas aeruginosa biofilm". In: *PLoS ONE* 7.4 (2012), pp. 1–9. ISSN: 19326203. DOI: 10.1371/journal.pone.0034337.

[299] Martina Maritan et al. "Building Structural Models of a Whole Mycoplasma Cell". In: *Journal of Molecular Biology* 434.2 (2022), p. 167351. ISSN: 10898638. DOI: 10.1016/j.jmb.2021.167351. URL: https://doi.org/10.1016/j.jmb.2021.167351.

[300] Arthur P. Goldberg et al. "Emerging whole-cell modeling principles and methods". In: *Current Opinion in Biotechnology* 51 (2018), pp. 97–102. ISSN: 18790429. DOI: 10.1016/j.copbio.2017.12.013.

[301] Denis Shepelin et al. "Benchmarking kinetic models of Escherichia coli metabolism". In: *bioRxiv* (2020). DOI: 10.1101/2020.01.16.908921.

[302] Zachary A. King et al. "BiGG Models: A platform for integrating, standardizing and sharing genome-scale models". In: *Nucleic Acids Research* 44.D1 (2016), pp. D515–D522. ISSN: 13624962. DOI: 10.1093/nar/gkv1049.

[303] Seppe vanden Broucke and Bart Baesens. *Practical Web Scraping for Data Science*. APress, 2018. ISBN: 9781484235829. DOI: 10.1007/978-1-4842-3582-9.

[304] S Nyamathulla et al. "A Review on Selenium Web Driver with Python". In: *Annals of the Romanian Society for Cell Biology* 25.4 (2021), pp. 16760–16768.

[305] Jan Schellenberger et al. "Quantitative prediction of cellular metabolism with constraint-based models: The COBRA Toolbox v2.0". In: *Nature Protocols* 6.9 (2011), pp. 1290–1307. ISSN: 17542189. DOI: 10.1038/nprot.2011.308.

[306] Colton J. Lloyd et al. "COBRAme: A computational framework for genome-scale models of metabolism and gene expression". In: *PLoS Computational Biology* 14.7 (2018), pp. 1–14. ISSN: 15537358. DOI: 10.1371/journal.pcbi.1006302.

[307] M. Loferer-Krößbacher, J. Klima, and R. Psenner. "Determination of bacterial cell dry mass by transmission electron microscopy and densitometric image analysis". In: *Applied and Environmental Microbiology* 64.2 (1998), pp. 688–694. ISSN: 00992240. DOI: 10.1128/aem.64.2.688-694.1998.

[308] David J. Lipman and William R. Pearson. "Rapid and Sensitive Protein Similarity Searches". In: *Science* 227.4693 (1985), pp. 1435–1441. DOI: https://doi.org/10.1126/science.2983426.

[309] Ken Thompson. "Programming Techniques: Regular expression search algorithm". In: *Communications of the ACM* 11.6 (1968), pp. 419–422. ISSN: 15577317. DOI: 10.1145/363347.363387.

[310] Mark Johnson et al. "NCBI BLAST: a better web interface." In: *Nucleic acids research* 36.Web Server issue (2008), pp. 5–9. ISSN: 13624962. DOI: 10.1093/nar/gkn201.

[311] Morgan N. Price and Adam P. Arkin. "Curated BLAST for Genomes". In: *mSystems* 4.2 (2019). ISSN: 2379-5077. DOI: 10.1128/msystems.00072-19.

[312] Peter J.A. Cock et al. "Biopython: Freely available Python tools for computational molecular biology and bioinformatics". In: *Bioinformatics* 25.11 (2009), pp. 1422–1423. ISSN: 13674803. DOI: 10.1093/bioinformatics/btp163.

[313] P. P. Dennis et al. "Varying rate of RNA chain elongation during rrn transcription in Escherichia coli". In: *Journal of Bacteriology* 191.11 (2009), pp. 3740–3746. ISSN: 00219193. DOI: 10.1128/JB.00128-09.

[314] U. Vogel and K. F. Jensen. "Effects of the antiterminator boxA on transcription elongation kinetics and ppGpp inhibition of transcription elongation in Escherichia coli". In: *Journal of Biological Chemistry* 270.31 (1995), pp. 18335–18340. ISSN: 00219258. DOI: 10.1074/jbc.270.31.18335.

[315] R. Young and H. Bremer. "Polypeptide chain elongation rate in Escherichia coli B/r as a function of growth rate". In: *Biochemical Journal* 160.2 (1976), pp. 185–194. ISSN: 02646021. DOI: 10.1042/bj1600185.

[316] John W. Tobias et al. "The N-end rule in bacteria". In: *Science* 254.5036 (1991), pp. 1374–1377. ISSN: 00368075. DOI: 10.1126/science.1962196.

[317] *Lysogeny broth*. URL: https://en.wikipedia.org/wiki/Lysogeny_broth.

[318] Pierre Jollès, Charles Alais, and Jacqueline jollès. "Amino acid composition of κ-casein and terminal amino acids of κ- and para-κ-casein". In: *Archives of Biochemistry and Biophysics* 98.1 (1962), pp. 56–57. ISSN: 10960384. DOI: 10.1016/0003-9861(62)90144-3.

[319] *Yeast extract spread*. URL: https://nutritiondata.self.com/facts/vegetables-and-vegetable-products/7691/2.

[320] W. D. Donachie. "Relationship between cell size and time of initiation of DNA replication". In: *Nature* 219.5158 (1968), pp. 1077–1079. ISSN: 00280836. DOI: 10.1038/2191077a0.

[321] Yanguang Cong, Sijin Yang, and Xiancai Rao. "Vancomycin resistant Staphylococcus aureus infections: A review of case updating and clinical features". In: *Journal of Advanced Research* 21 (2020), pp. 169–176. ISSN: 20901232. DOI: 10.1016/j.jare.2019.10.005. URL: https://doi.org/10.1016/j.jare.2019.10.005.

[322] W. Haas, K.K. Mitchell, and K.A. Musser. *Staphylococcus aureus strain VMRSA-WC082 chromosome, complete genome*. 2022. URL: https://www.ncbi.nlm.nih.gov/nuccore/NZ_CP092550.1?report=genbank.

[323] V. Enouf, D. Briand, and S. van der Werf. *Middle East respiratory syndrome coronavirus isolate FRA/UAE, complete genome*. 2013. URL: https://www.ncbi.nlm.nih.gov/nucleotide/KF745068.1?report=genbank&log$=nuclalign&blast_rank=1&RID=10Z3UP8E016.

[324] Yosef D. Roth et al. "Datanator: An integrated database of molecular data for quantitatively modeling cellular behavior". In: *Nucleic Acids Research* 49.D1 (2021), pp. D516–D522. ISSN: 13624962. DOI: 10.1093/nar/gkaa1008.

[325] Samuel M.D. Seaver et al. "The ModelSEED Biochemistry Database for the integration of metabolic annotations and the reconstruction, comparison and analysis of metabolic models for plants, fungi and microbes". In: *Nucleic Acids Research* 49.D1 (2021), pp. D575–D588. ISSN: 13624962. DOI: 10.1093/nar/gkaa746.

[326] Richard Feynman, Michael A. Gottlieb, and Rudolf Pfdiffer. *Chapter 43: Diffusion*. 1963. URL: https://www.feynmanlectures.caltech.edu/I_43.html.

[327] Sarah L. Baines et al. "Convergent adaptation in the dominant global hospital clone ST239 of methicillin-resistant Staphylococcus aureus". In: *mBio* 6.2 (2015). ISSN: 21507511. DOI: 10.1128/mBio.00080-15.

[328] Jae Hoon Song et al. "Spread of methicillin-resistant Staphylococcus aureus between the community and the hospitals in Asian countries: An ANSORP study". In: *Journal of Antimicrobial Chemotherapy* 66.5 (2011), pp. 1061–1069. ISSN: 03057453. DOI: 10.1093/jac/dkr024.

[329] Michael A. Borg et al. "Prevalence of methicillin-resistant Staphylococcus aureus (MRSA) in invasive isolates from southern and eastern Mediterranean countries". In: *Journal of Antimicrobial Chemotherapy* 60.6 (2007), pp. 1310–1315. ISSN: 14602091. DOI: 10.1093/jac/dkm365.

[330] Rima A. Moghnieh et al. "Epidemiology of common resistant bacterial pathogens in the countries of the Arab League". In: *The Lancet Infectious Diseases* 18.12 (2018), e379–e394. ISSN: 14744457. DOI: 10.1016/S1473-3099(18)30414-6. URL: http://dx.doi.org/10.1016/S1473-3099(18)30414-6.

[331] Thomas P. Van Boeckel et al. "Reducing antimicrobial use in food animals". In: *Science* 357.6358 (2017), pp. 1350–1352. ISSN: 10959203. DOI: 10.1126/science.aao1495.

[332] Paul Eggleton. "The state of the world". In: *Annual Reviews of Environment and Resources* 45 (2020), pp. 61–82. ISSN: 10276084. DOI: 10.2979/vic.2005.48.1.124.

[333] B. J. Hartman and A. Tomasz. "Low-affinity penicillin-binding protein associated with β-lactam resistance in Staphylococcus aureus". In: *Journal of Bacteriology* 158.2 (1984), pp. 513–516. ISSN: 00219193. DOI: 10.1128/jb.158.2.513-516.1984.

[334] Michael R. Hamblin and Tayyaba Hasan. "Photodynamic therapy: A new antimicrobial approach to infectious disease?" In: *Photochemical and Photobiological Sciences* 3.5 (2004), pp. 436–450. ISSN: 14749092. DOI: 10.1039/b311900a.

[335] Krista Rule Wigginton et al. "Oxidation of virus proteins during UV254 and singlet oxygen mediated inactivation". In: *Environmental Science and Technology* 44.14 (2010), pp. 5437–5443. ISSN: 15205851. DOI: 10.1021/es100435a.

[336] Natalya Sh Lebedeva et al. "The application of porphyrins and their analogues for inactivation of viruses". In: *Molecules* 25.19 (2020). ISSN: 14203049. DOI: 10.3390/molecules25194368.

[337] Karim Ergaieg et al. "Involvement of both Type I and Type II mechanisms in Gram-positive and Gram-negative bacteria photosensitization by a meso-substituted cationic porphyrin". In: *Solar Energy* 82.12 (2008), pp. 1107–1117. ISSN: 0038092X. DOI: 10.1016/j.solener.2008.05.008.

[338] Michael P. Allen. "Introduction to molecular dynamics simulations". In: *Computational soft matter: From synthetic polymers to proteins*. Ed. by Norbert Attig et al. Vol. 23. John von Neumann Institute for Computing, 2004, pp. 1–28. ISBN: 9780128169544. DOI: 10.1016/B978-0-12-816954-4.00001-2.

[339] Richard Henze et al. "Multi-scale stochastic organization-oriented coarse-graining exemplified on the human mitotic checkpoint". In: *Scientific Reports* 9.1 (2019), pp. 1–17. ISSN: 20452322. DOI: 10.1038/s41598-019-40648-w. URL: http://dx.doi.org/10.1038/s41598-019-40648-w.

[340] Muhammad H. Zaman et al. "Computational model for cell migration in three-dimensional matrices". In: *Biophysical Journal* 89.2 (2005), pp. 1389–1397. ISSN: 00063495. DOI: 10.1529/biophysj.105.060723. URL: http://dx.doi.org/10.1529/biophysj.105.060723.

[341] Daniel T. Gillespie. "Stochastic Simulation of Chemical Kinetics". In: *Annual Review of Physical Chemistry* 58.1 (2007), pp. 35–55. ISSN: 0066-426X. DOI: 10.1146/annurev.physchem.58.032806.104637.

[342] Richard G. Zepp, Bruce C. Faust, and Hoigné Jürg. "Hydroxyl Radical Formation in Aqueous Reactions (pH 3-8) of Iron(II) with Hydrogen Peroxide: The Photo-Fenton Reaction". In: *Environmental Science and Technology* 26.2 (1992), pp. 313–319. ISSN: 15205851. DOI: 10.1021/es00026a011.

[343] W. H. Koppenol. "The Haber-Weiss cycle - 70 years later". In: *Redox Report* 6.4 (2001), pp. 229–234. ISSN: 13510002. DOI: 10.1179/135100001101536373.

[344] Eunok Choe and David B. Min. "Mechanisms and factors for edible oil oxidation". In: *Comprehensive Reviews in Food Science and Food Safety* 5.4 (2006), pp. 169–186. ISSN: 15414337. DOI: 10.1111/j.1541-4337.2006.00009.x.

[345] E. N. Frankel. "Lipid oxidation". In: *Prog. Lipid Res.* 19 (1980), pp. 1–22. DOI: 10.1201/9781420046359-c7.

[346] Anabela Tavares et al. "Antimicrobial photodynamic therapy: Study of bacterial recovery viability and potential development of resistance after treatment". In: *Marine Drugs* 8.1 (2010), pp. 91–105. ISSN: 16603397. DOI: 10.3390/md8010091.

[347] Federico M. Lauro et al. "Photoinactivation of bacterial strains involved in periodontal diseases sensitized by porphycene–polylysine conjugates". In: *Photochemical and Photobiological Sciences* 1.7 (2002), pp. 468–470. ISSN: 14749092. DOI: 10.1039/b200977c.

[348] Lisa A. Pedigo et al. "Absence of bacterial resistance following repeat exposure to photodynamic therapy". In: *Proceedings of SPIE* 7380.July 2009 (2009), 73803H. ISSN: 0277-786X. DOI: 10.1117/12.822834.

[349] Roghayeh Ghorbanzadeh et al. "Modulation of virulence in Enterococcus faecalis cells surviving antimicrobial photodynamic inactivation with reduced graphene oxide-curcumin: An ex vivo biofilm model". In: *Photodiagnosis and Photodynamic Therapy* 29.December 2019 (2020), p. 101643. ISSN: 18731597. DOI: 10.1016/j.pdpdt.2019.101643. URL: https://doi.org/10.1016/j.pdpdt.2019.101643.

[350] Sandra Beirão et al. "Photodynamic inactivation of bacterial and yeast biofilms with a cationic porphyrin". In: *Photochemistry and Photobiology* 90.6 (2014), pp. 1387–1396. ISSN: 17511097. DOI: 10.1111/php.12331.

[351] J. Moan. "The photochemical yield of singlet oxygen". In: 39.4 (1984), pp. 445–449.

[352] Johan Moan. "On the diffusion length of singlet oxygen in cells and tissues". In: *Journal of Photochemistry and Photobiology B: Biology* 6 (1990), pp. 343–347.

[353] Michael A.J. Rodgers and Paul T. Snowden. "Lifetime of O2(1Δg) in Liquid Water As Determined by Time-Resolved Infrared Luminescence Measurements". In: *Journal of the American Chemical Society* 104.20 (1982), pp. 5541–5543. ISSN: 15205126. DOI: 10.1021/ja00384a070.

[354] Carsten Lange et al. *Comparison of cellular death pathways after mTHPC-mediated photodynamic therapy (PDT) in five human cancer cell lines*. Vol. 11. 5. 2019. DOI: 10.3390/cancers11050702.

[355] Tamar Kohn et al. "Association with natural organic matter enhances the sunlight-mediated inactivation of MS2 coliphage by singlet oxygen". In: *Environmental Science and Technology* 41.13 (2007), pp. 4626–4632. ISSN: 0013936X. DOI: 10.1021/es070295h.

[356] Simón Mostafa and Fernando L. Rosario-Ortiz. "Singlet oxygen formation from wastewater organic matter". In: *Environmental Science and Technology* 47.15 (2013), pp. 8179–8186. ISSN: 0013936X. DOI: 10.1021/es401814s.

[357] M. Emilia Jiménez-Hernández et al. "Solar water disinfection by singlet oxygen photogenerated with polymer-supported Ru(II) sensitizers". In: *Solar Energy* 80.10 (2006), pp. 1382–1387. ISSN: 0038092X. DOI: 10.1016/j.solener.2005.04.027.

[358] Colin P. McCoy et al. "Photodynamic antimicrobial polymers for infection control". In: *PLoS ONE* 9.9 (2014), pp. 1–11. ISSN: 19326203. DOI: 10.1371/journal.pone.0108500.

[359] Sung Ho Kim et al. "Design of TiO2 nanoparticle self-assembled aromatic polyamide thin-film-composite (TFC) membrane as an approach to solve biofouling problem". In: *Journal of Membrane Science* 211.1 (2003), pp. 157–165. ISSN: 03767388. DOI: 10.1016/S0376-7388(02)00418-0.

[360] Zivile Luksiene et al. "Novel approach to effective and uniform inactivation of gram-positive Listeria monocytogenes and gram-negative Salmonella enterica by photosensitization". In: *Food Technology and Biotechnology* 51.3 (2013), pp. 338–344. ISSN: 13309862.

[361] Alex Fiori Silva et al. "Photodynamic inactivation as an emergent strategy against foodborne pathogenic bacteria in planktonic and sessile states". In: *Critical Reviews in Microbiology* 44.6 (2018), pp. 667–684. ISSN: 15497828. DOI: 10.1080/1040841X.2018.1491528. URL: https://doi.org/10.1080/1040841X.2018.1491528.

[362] Xi Zhi Niu et al. "Roles of singlet oxygen and dissolved organic matter in self-sensitized photooxidation of antibiotic norfloxacin under sunlight irradiation". In: *Water Research* 106 (2016), pp. 214–222. ISSN: 18792448. DOI: 10.1016/j.watres.2016.10.002.

[363] Maria C. DeRosa and Robert J. Crutchley. "Photosensitized singlet oxygen and its applications". In: *Coordination Chemistry Reviews* 233-234 (2002), pp. 351–371. ISSN: 00108545. DOI: 10.1016/S0010-8545(02)00034-6.

[364] Fausto G. Fumi and Robert G. Parr. "Electronic states of diatomic molecules: The Oxygen molecule". In: *The Journal of Chemical Physics* 21.10 (1953), pp. 1864–1868. ISSN: 00296341. DOI: 10.1007/BF02827770.

[365] J. Katriel. "A study of the interpretation of Hund's rule". In: *Theoretica Chimica Acta* 23.4 (1972), pp. 309–315. ISSN: 00405744. DOI: 10.1007/BF00526436.

[366] Steffen Jockusch et al. "Singlet molecular oxygen by direct excitation". In: *Photochemical and Photobiological Sciences* 7.2 (2008), pp. 235–239. ISSN: 14749092. DOI: 10.1039/b714286b.

[367] I. S. Bowen. "Forbidden lines". In: *Reviews of Modern Physics* 8.2 (1936), pp. 55–78.

[368] David Kessel and Eliana Rossi. "Determinants of Porphyrin-Sensitized Photooxidation Characterized By Fluorescence and Absorption Spectra". In: *Photochemistry and Photobiology* 35.1 (1982), pp. 37–41. ISSN: 17511097. DOI: 10.1111/j.1751-1097.1982.tb03808.x.

[369] Eion G. Mcrae and Michael Kasha. "Enhancement of phosphorescence ability upon aggregation of dye molecules [6]". In: *The Journal of Chemical Physics* 28.4 (1958), pp. 721–722. ISSN: 00219606. DOI: 10.1063/1.1744225.

[370] Michael Prein and Waldemar Adam. "The Schenck Ene Reaction: Diastereoselective Oxyfunctionalization with Singlet Oxygen in Synthetic Applications". In: *Angewandte Chemie (International Edition in English)* 35.5 (1996), pp. 477–494. ISSN: 05700833. DOI: 10.1002/anie.199604771.

[371] Waldemar Adam et al. *Diastereoselective singlet oxygen ene reaction (Schenck reaction) and diastereoselective epoxidations of heteroatom-substituted acyclic chiral olefins: A mechanistic comparison*. 1996. DOI: 10.1021/ja9530230.

[372] Christopher S. Foote, S. Wexler, and Wataru Ando. "Chemistry of singlet oxygen III. Product selectivity". In: *Tetrahedron Letters* 6.46 (1965), pp. 4111–4118. ISSN: 00404039. DOI: 10.1016/S0040-4039(01)99574-7.

[373] J L Bolland. "Kinetics of olefin oxidation". In: *Quarterly Reviews, Chemical Society* 3 (1949), pp. 1–21.

[374] Ernest Harold Farmer and Alvapillai Sundralingam. "The course of autoxidation reactions in polyisoprenes and allied compounds. Part IV. The peroxidation of Rubber". In: *Journal of the American Chemical Society* (1943), pp. 125–133.

[375] Ganna Gryn'ova, Jennifer L. Hodgson, and Michelle L. Coote. "Revising the mechanism of polymer autooxidation". In: *Organic and Biomolecular Chemistry* 9.2 (2011), pp. 480–490. ISSN: 14770520. DOI: 10.1039/c0ob00596g.

[376] G. Litwinienko, A. Daniluk, and T. Kasprzycka-Guttman. "Differential scanning calorimetry study on the oxidation of C12-C18 saturated fatty acids and their esters". In: *JAOCS, Journal of the American Oil Chemists' Society* 76.6 (1999), pp. 655–657. ISSN: 0003021X. DOI: 10.1007/s11746-999-0156-6.

[377] A. G. O'Donnell et al. "Numerical analysis of fatty acid profiles in the identification of staphylococci". In: *Journal of General Microbiology* 131.8 (1985), pp. 2023–2033. ISSN: 00221287. DOI: 10.1099/00221287-131-8-2023.

[378] A. A. Krasnovsky, A. S. Kozlov, and Ya V. Roumbal. "Photochemical investigation of the IR absorption bands of molecular oxygen in organic and aqueous environment". In: *Photochemical and Photobiological Sciences* 11.6 (2012), pp. 988–997. ISSN: 14749092. DOI: 10.1039/c2pp05350k.

[379] Charles Long and David R Kearns. "Selection rules for the intermolecular enhancement of spin forbidden transitions in molecular oxygen". In: *The Journal of Chemical Physics* 59.10 (2003), pp. 5729–5736.

[380] Youngmin You. "Chemical tools for the generation and detection of singlet oxygen". In: *Organic and Biomolecular Chemistry* 16.22 (2018), pp. 4044–4060. ISSN: 14770520. DOI: 10.1039/c8ob00504d.

[381] Oliver Schalk et al. "Near-infrared excitation of the Q band in free base and zinc tetratolylporphyrins". In: *Journal of Physical Chemistry A* 112.8 (2008), pp. 1719–1729. ISSN: 10895639. DOI: 10.1021/jp075907z.

[382] Rumiana Bakalova et al. "Quantum dots as photosensitizers?" In: *Nature Biotechnology* 22.11 (2004), pp. 1360–1361. ISSN: 10870156. DOI: 10.1038/nbt1104-1360.

[383] Raymond Bonnett and Gabriel Martinez. "ChemInform Abstract: Photobleaching of Sensitisers Used in Photodynamic Therapy". In: *ChemInform* 33.11 (2010), no–no. DOI: 10.1002/chin.200211234.

[384] P. K.W. Wasser and J. -H Fuhrhop. "The Photooxygenation of Metalloporphyrins and Metallochlorins". In: *Annals of the New York Academy of Sciences* 206.1 (1973), pp. 533–548. ISSN: 17496632. DOI: 10.1111/j.1749-6632.1973.tb43235.x.

[385] Nicolay N Kruk et al. "Photophysics of the cationic 5,10,15,20-tetrakis(4-N-methylpyridyl) porphyrin bound to DNA, [poly(dA-dT)]_2 and [poly(dG-dC)]_2: Interaction With Molecular Oxygen Studied By Porphyrin Triplet-Triplet Absorption and Singlet Oxygen Luminescence". In: *Journal of Photochemistry and Photobiology B: Biology* 42 (1998), pp. 181–190.

[386] Martin Kullmann et al. "Ultrafast exciton dynamics after Soret- or Q-band excitation of a directly β,β-linked bisporphyrin". In: *Physical Chemistry Chemical Physics* 14.22 (2012), pp. 8038–8050. ISSN: 14639076. DOI: 10.1039/c2cp23608g.

[387] Albert Van Der Wal et al. "Determination of the total charge in the cell walls of Gram-positive bacteria". In: *Colloids and Surfaces B: Biointerfaces* 9.1-2 (1997), pp. 81–100. ISSN: 09277765. DOI: 10.1016/S0927-7765(96)01340-9.

[388] J. S. Dickson and M. Koohmaraie. "Cell surface charge characteristics and their relationship to bacterial attachment to meat surfaces". In: *Applied and Environmental Microbiology* 55.4 (1989), pp. 832–836. ISSN: 00992240. DOI: 10.1128/aem.55.4.832-836.1989.

[389] Saskia a G Lambrechts et al. "Photodynamic therapy for S. aureus infected burn wounds in mice". In: *Photochemical and Photobiological Sciences* 4 (2005), pp. 503–509.

[390] Cristiane Campos Costa Quishida et al. "Photodynamic inactivation of a multispecies biofilm using curcumin and LED light". In: *Lasers in Medical Science* 31.5 (2016), pp. 997–1009. ISSN: 1435604X. DOI: 10.1007/s10103-016-1942-7. URL: http://dx.doi.org/10.1007/s10103-016-1942-7.

[391] Cyril Ringot et al. "Porphyrin-grafted cellulose fabric: New photobactericidal material obtained by "Click-Chemistry" reaction". In: *Materials Letters* 63.21 (2009), pp. 1889–1891. ISSN: 0167577X. DOI: 10.1016/j.matlet.2009.06.009. URL: http://dx.doi.org/10.1016/j.matlet.2009.06.009.

[392] Bharadwaja S.T. Peddinti et al. "Photodynamic Polymers as Comprehensive Anti-Infective Materials: Staying Ahead of a Growing Global Threat". In: *ACS Applied Materials and Interfaces* 10.31 (2018), pp. 25955–25959. ISSN: 19448252. DOI: 10.1021/acsami.8b09139.

[393] Bart Gottenbos et al. "Antimicrobial effects of positively charged surfaces on adhering Gram-positive and Gram-negative bacteria". In: *Journal of Antimicrobial Chemotherapy* 48.1 (2001), pp. 7–13. ISSN: 03057453. DOI: 10.1093/jac/48.1.7.

[394] K. G. Specht and M. A.J. Rodgers. "Depolarization of Mouse Myeloma Cell Membranes During Photodynamic Action". In: *Photochemistry and Photobiology* 51.3 (1990), pp. 319–324. ISSN: 17511097. DOI: 10.1111/j.1751-1097.1990.tb01717.x.

[395] Benjamin Ehrenberg et al. "Electric depolarization of photosensitized cells: lipid vs. protein alterations". In: *BBA - Biomembranes* 1151.2 (1993), pp. 257–264. ISSN: 00052736. DOI: 10.1016/0005-2736(93)90110-L.

[396] Tim Maisch et al. "Antibacterial photodynamic therapy in dermatology". In: *Photochemical and Photobiological Sciences* 3.10 (2004), pp. 907–917. ISSN: 14749092. DOI: 10.1039/b407622b.

[397] Khageswar Sahu et al. "Atomic force microscopic study on morphological alterations induced by photodynamic action of Toluidine Blue O in Staphylococcus aureus and Escherichia coli". In: *Journal of Photochemistry and Photobiology B: Biology* 96.1 (2009), pp. 9–16. ISSN: 10111344. DOI: 10.1016/j.jphotobiol.2009.03.008.

[398] G. Bertoloni et al. "Role of Specific Cellular Targets in the Hematoporphyrin-Sensitized Photoinactivation of Microbial Cells". In: *Photochemistry and Photobiology* 46.5 (1987), pp. 695–698. ISSN: 17511097. DOI: 10.1111/j.1751-1097.1987.tb04834.x.

[399] Michèle Merchat et al. "Meso-substituted cationic porphyrins as efficient photosensitizers of gram-positive and gram-negative bacteria". In: *Journal of Photochemistry and Photobiology B: Biology* 32.3 (1996), pp. 153–157. ISSN: 10111344. DOI: 10.1016/1011-1344(95)07147-4.

[400] B Bagchi and Sreeradha Basu. "Role of dye molecules remaining outside the cell during photodynamic inactivation of Escherichia coli in the presence of acriflavine". In: *Photochemistry and Photobiology* 29 (1979), pp. 403–405.

[401] F. Prat, C. C. Hou, and C. S. Foote. "Determination of the quenching rate constants of singlet oxygen by derivatized nucleosides in nonaqueous solution [9]". In: *Journal of the American Chemical Society* 119.21 (1997), pp. 5051–5052. ISSN: 00027863. DOI: 10.1021/ja963537e.

[402] Thomas P.A. Devasagayam et al. "Formation of 8-Hydroxy(deoxy)guanosine and Generation of Strand Breaks at Guanine Residues in DNA by Singlet Oxygen". In: *Biochemistry* 30.25 (1991), pp. 6283–6289. ISSN: 15204995. DOI: 10.1021/bi00239a029.

[403] Cristiane Aparecida Pereira et al. “Photodynamic inactivation of Streptococcus mutans and Streptococcus sanguinis biofilms in vitro”. In: *Lasers in Medical Science* 28.3 (2013), pp. 859–864. ISSN: 02688921. DOI: 10.1007/s10103-012-1175-3.

[404] Fanny Ramel et al. “Chemical quenching of singlet oxygen by carotenoids in plants”. In: *Plant Physiology* 158.3 (2012), pp. 1267–1278. ISSN: 00320889. DOI: 10.1104/pp.111.182394.

[405] Wilbert Mtangi et al. “Control of Electrons’ Spin Eliminates Hydrogen Peroxide Formation during Water Splitting”. In: *Journal of the American Chemical Society* 139.7 (2017), pp. 2794–2798. ISSN: 15205126. DOI: 10.1021/jacs.6b12971.

[406] Vincent Carré et al. “Fungicidal properties of meso-arylglycosylporphyrins : Influence of sugar substituents on photoinduced damage in the yeast Saccharomyces cerevisiae”. In: *Journal of Photochemistry and Photobiology B: Biology* 48.1 (1999), pp. 57–62. ISSN: 10111344. DOI: 10.1016/S1011-1344(99)00009-3.

[407] M. A. Pereira et al. “Influence of external bacterial structures on the efficiency of photodynamic inactivation by a cationic porphyrin”. In: *Photochemical and Photobiological Sciences* 13.4 (2014), pp. 680–690. ISSN: 14749092. DOI: 10.1039/c3pp50408e.

[408] Helena Ashkenazi, Yeshayahu Nitzan, and Dezso Gál. “Photodynamic Effects of Antioxidant Substituted Porphyrin Photosensitizers on Gram-positive and -negative Bacteria¶”. In: *Photochemistry and Photobiology* 77.2 (2003), p. 186. ISSN: 0031-8655. DOI: 10.1562/0031-8655.

[409] Johan Moan and Arnt I. Vistnes. “Porphyrin Photosensitization of Proteins in Cell Membranes As Studied By Spin-Labelling and By Quantification of Dtnb-Reactive Sh-Groups”. In: *Photochemistry and Photobiology* 44.1 (1986), pp. 15–19. ISSN: 17511097. DOI: 10.1111/j.1751-1097.1986.tb03558.x.

[410] Yeshayahu Nitzan et al. “Inactivation of Gram-Negative Bacteria By Photosensitized Porphyrins”. In: *Photochemistry and Photobiology* 55.1 (1992), pp. 89–96. ISSN: 17511097. DOI: 10.1111/j.1751-1097.1992.tb04213.x.

[411] Edgardo Durantini. “Photodynamic inactivation of bacteria”. In: *Current Bioactive Compounds* 2.2 (2006), pp. 127–142. ISSN: 15734072. DOI: 10.2174/157340706777435158.

[412] Mali Salmon-Divon, Yeshayahu Nitzan, and Zvi Malik. “Mechanistic aspects of Escherichia coli photodynamic inactivation by cationic tetra-meso(N-methylpyridyl)porphine”. In: *Photochemical and Photobiological Sciences* 3.5 (2004), pp. 423–429. ISSN: 14749092. DOI: 10.1039/b315627n.

[413] Giulio Bertoloni et al. “Photosensitizing activity of hematoporphyrin on Staphylococcus aureus cells”. In: *Biochimica et Biophysica Acta - General Subjects* 1475.2 (2000), pp. 169–174. ISSN: 03044165. DOI: 10.1016/S0304-4165(00)00071-4.

[414] Raymond Bonnett et al. "Photobleaching of 5,10,15,20-tetrakis(m-hydroxyphenyl)porphyrin (m-THPP) and the corresponding chlorin (m-THPC) and bacteriochlorin (m-THPBC). A comparative study". In: *Journal of Photochemistry and Photobiology B: Biology* 53.1-3 (1999), pp. 136–143. ISSN: 10111344. DOI: 10.1016/S1011-1344(99)00139-6.

[415] Giulio Jori et al. "Photodynamic therapy in the treatment of microbial infections: Basic principles and perspective applications". In: *Lasers in Surgery and Medicine* 38.5 (2006), pp. 468–481. ISSN: 01968092. DOI: 10.1002/lsm.20361.

[416] Faten Gad et al. "Targeted photodynamic therapy of established soft-tissue infections in mice". In: *Photochemical and Photobiological Sciences* 3.5 (2004), pp. 451–458. ISSN: 14749092. DOI: 10.1039/b311901g.

[417] Yuewu Zhao et al. "Porphyrin-based metal-organic frameworks: Protonation induced Q band absorption". In: *Nanoscale* 11.25 (2019), pp. 12250–12258. ISSN: 20403372. DOI: 10.1039/c9nr02463h.

[418] Arie Orenstein et al. "The use of porphyrins for eradication of Staphylococcus aureus in burn wound infections". In: *FEMS Immunology and Medical Microbiology* 19.4 (1997), pp. 307–314. ISSN: 09288244. DOI: 10.1016/S0928-8244(97)00097-7.

[419] M. Merchat et al. "Studies on the mechanism of bacteria photosensitization by meso-substituted cationic porphyrins". In: *Journal of Photochemistry and Photobiology B: Biology* 35.3 (1996), pp. 149–157. ISSN: 10111344. DOI: 10.1016/S1011-1344(96)07321-6.

[420] Xuebin Huang et al. "Porphyrin-dithienothiophene π-conjugated copolymers: Synthesis and their applications in field-effect transistors and solar cells". In: *Macromolecules* 41.19 (2008), pp. 6895–6902. ISSN: 00249297. DOI: 10.1021/ma801407u.

[421] Jiří Mosinger and Zdeněk Mička. "Quantum yields of singlet oxygen of metal complexes of meso-tetrakis (sulphonatophenyl) porphine". In: *Journal of Photochemistry and Photobiology A: Chemistry* 107.1-3 (1997), pp. 77–82. ISSN: 10106030. DOI: 10.1016/S1010-6030(96)04613-8.

[422] Kimihiko Hirao. "Theoretical study of the Q and B bands of free-base, magnesium, and zinc porphyrins, and their derivatives". In: *Journal of Physical Chemistry A* 103.12 (1999), pp. 1894–1904. ISSN: 10895639. DOI: 10.1021/jp984807d.

[423] Wenting Wu et al. "BODIPY-based photosensitizers with intense visible light harvesting ability and high 1O2 quantum yield in aqueous solution". In: *RSC Advances* 4.93 (2014), pp. 51349–51352. ISSN: 20462069. DOI: 10.1039/c4ra08654f.

[424] Jorge N. Chacon, James McLearie, and Roy S. Sinclair. "Singlet Oxygen Yields and Radical Contributions in the Dye-Sensitised Photo-oxidation in methanol of esters of polyunsaturated fatty acids _oleic, linoleic, linolenic, and arachidonic)". In: *Photochemistry and photobiology* 47.5 (1988), pp. 647–765.

[425] Patrick Jäger et al. "Q and Soret Band Photoexcitation of Isolated Palladium Porphyrin Tetraanions Leads to Delayed Emission of Nonthermal Electrons over Microsecond Time Scales". In: *Journal of Physical Chemistry Letters* 7.7 (2016), pp. 1167–1172. ISSN: 19487185. DOI: 10.1021/acs.jpclett.6b00407.

[426] Jerzy Karolczak et al. "Photophysical studies of porphyrins and metalloporphyrins: Accurate measurements of fluorescence spectra and fluorescence quantum yields for Soret band excitation of zinc tetraphenylporphyrin". In: *Journal of Physical Chemistry A* 108.21 (2004), pp. 4570–4575. ISSN: 10895639. DOI: 10.1021/jp049898v.

[427] Sean Mathai, Trevor A. Smith, and Kenneth P. Ghiggino. "Singlet oxygen quantum yields of potential porphyrin-based photosensitisers for photodynamic therapy". In: *Photochemical and Photobiological Sciences* 6.9 (2007), pp. 995–1002. ISSN: 14749092. DOI: 10.1039/b705853e.

[428] Caetano P. Sabino et al. "Inactivation kinetics and lethal dose analysis of antimicrobial blue light and photodynamic therapy". In: *Photodiagnosis and Photodynamic Therapy* 28.May (2019), pp. 186–191. ISSN: 18731597. DOI: 10.1016/j.pdpdt.2019.08.022. URL: https://doi.org/10.1016/j.pdpdt.2019.08.022.

[429] I. Buchovec, Z. Vaitonis, and Z. Luksiene. "Novel approach to control Salmonella enterica by modern biophotonic technology: Photosensitization". In: *Journal of Applied Microbiology* 106.3 (2009), pp. 748–754. ISSN: 13645072. DOI: 10.1111/j.1365-2672.2008.03993.x.

[430] D. Dementavicius et al. "Application of mathematical models for bacterial inactivation curves using Hypericin-based photosensitization". In: *Journal of Applied Microbiology* 120.6 (2016), pp. 1492–1500. ISSN: 13652672. DOI: 10.1111/jam.13127.

[431] Kristina Aponiene et al. "Reduction of microbial contamination of fruits and vegetables by hypericin-based photosensitization: Comparison with other emerging antimicrobial treatments". In: *Journal of Food Engineering* 144 (2015), pp. 29–35. ISSN: 02608774. DOI: 10.1016/j.jfoodeng.2014.07.012. URL: http://dx.doi.org/10.1016/j.jfoodeng.2014.07.012.

[432] Z. Vaitonis and Ž Lukšiene. "Led-based light sources for decontamination of food: Modelling photosensitization-based inactivation of pathogenic bacteria". In: *Lithuanian Journal of Physics* 50.1 (2010), pp. 141–145. ISSN: 16488504. DOI: 10.3952/lithjphys.50102.

[433] Michal Brasel, Michal Pieranski, and Mariusz Grinholc. "An extended logistic model of photodynamic inactivation for various levels of irradiance using the example of Streptococcus agalactiae". In: *Scientific Reports* 10.1 (2020), pp. 1–17. ISSN: 20452322. DOI: 10.1038/s41598-020-71033-7. URL: https://doi.org/10.1038/s41598-020-71033-7.

[434] L. Brancaleon and H. Moseley. "Laser and non-laser light sources for photodynamic therapy". In: *Lasers in Medical Science* 17.3 (2002), pp. 173–186. ISSN: 02688921. DOI: 10.1007/s101030200027.

[435] Adriele R. Santos et al. "Application of response surface methodology to evaluate photodynamic inactivation mediated by Eosin Y and 530 nm LED AGAINST staphylococcus aureus". In: *Antibiotics* 9.3 (2020), pp. 2–11. ISSN: 20796382. DOI: 10.3390/antibiotics9030125.

[436] Mikael Andersson et al. "Photoinduced electron transfer reactions in a porphyrin-viologen complex: Observation of S2 to S1 relaxation and electron transfer from the S2 state". In: *Journal of Physical Chemistry B* 103.16 (1999), pp. 3258–3262. ISSN: 15206106. DOI: 10.1021/jp9829795.

[437] G. G. Gurzadyan, T. H. Tran-Thi, and T. Gustavsson. "Time-resolved fluorescence spectroscopy of high-lying electronic states of Zn-tetraphenylporphyrin". In: *Journal of Chemical Physics* 108.2 (1998), pp. 385–388. ISSN: 00219606. DOI: 10.1063/1.475398.

[438] Seiji Akimoto et al. "Ultrafast excitation transfer and relaxation in linear and crossed-linear arrays of porphyrins". In: *Pure and Applied Chemistry* 71.11 (1999), pp. 2107–2115. ISSN: 00334545. DOI: 10.1351/pac199971112107.

[439] Adriana Passarella Gerola et al. "Chemical determination of singlet oxygen from photosensitizers illuminated with LED: New calculation methodology considering the influence of photobleaching". In: *Journal of Photochemistry and Photobiology A: Chemistry* 232 (2012), pp. 14–21. ISSN: 10106030. DOI: 10.1016/j.jphotochem.2012.01.018. URL: http://dx.doi.org/10.1016/j.jphotochem.2012.01.018.

[440] Thomas S. Mang et al. "Photobleaching of Porphyrins Used in Photodynamic Therapy and Implications for Therapy". In: *Photochemistry and Photobiology* 45.4 (1987), pp. 501–506. ISSN: 17511097. DOI: 10.1111/j.1751-1097.1987.tb05409.x.

[441] Jonathan S. Dysart, Gurmit Singh, and Michael S. Patterson. "Calculation of Singlet Oxygen Dose from Photosensitizer Fluorescence and Photobleaching During mTHPC Photodynamic Therapy of MLL Cells¶". In: *Photochemistry and Photobiology* 81.1 (2005), p. 196. ISSN: 0031-8655. DOI: 10.1562/2004-07-23-ra-244.1.

[442] Hendrik Küpper et al. "Kinetics and efficiency of excitation energy transfer from chlorophylls, their heavy metal-substituted derivatives, and pheophytins to singlet oxygen". In: *Biochimica et Biophysica Acta - General Subjects* 1572.1 (2002), pp. 107–113. ISSN: 03044165. DOI: 10.1016/S0304-4165(02)00284-2.

[443] John D. Spikes. "Quantum Yields and Kinetics of the Photobleaching of Hematoporphyrin, Photofrin Ii, Tetra(4-Sulfonatophenyl)-Porphine and Uroporphyrin". In: *Photochemistry and Photobiology* 55.6 (1992), pp. 797–808. ISSN: 17511097. DOI: 10.1111/j.1751-1097.1984.tb08388.x.

[444] Alisdair N. Macpherson et al. "Direct detection of singlet oxygen from isolated Photosystem II reaction centres". In: *BBA - Bioenergetics* 1143.3 (1993), pp. 301–309. ISSN: 00052728. DOI: 10.1016/0005-2728(93)90201-P.

[445] Tim Maisch et al. “The role of singlet oxygen and oxygen concentration in photodynamic inactivation of bacteria”. In: *Proceedings of the National Academy of Sciences of the United States of America* 104.17 (2007), pp. 7223–7228. ISSN: 00278424. DOI: 10.1073/pnas.0611328104.

[446] Jürgen Baier et al. “Time-resolved investigations of singlet oxygen luminescence in water, in phosphatidylcholine, and in aqueous suspensions of phosphatidylcholine or HT29 cells”. In: *Journal of Physical Chemistry B* 109.7 (2005), pp. 3041–3046. ISSN: 15206106. DOI: 10.1021/jp0455531.

[447] Naoki Watabe et al. “Oxidation decomposition of unsaturated fatty acids by singlet oxygen in phospholipid bilayer membranes.” In: *Journal of oleo science* 56.2 (2007), pp. 73–80. ISSN: 13473352. DOI: 10.5650/jos.56.73.

[448] Kazuo Mukai et al. “Kinetic study of the quenching reaction of singlet oxygen by eight vegetable oils in solution”. In: *Journal of Oleo Science* 68.1 (2019), pp. 21–31. ISSN: 13473352. DOI: 10.5650/jos.ess18179.

[449] Hans Curt Flemming and Jost Wingender. “The biofilm matrix”. In: *Nature Reviews Microbiology* 8.9 (2010), pp. 623–633. ISSN: 17401526. DOI: 10.1038/nrmicro2415.

[450] Sarah M Keating et al. “ SBML Level 3: an extensible format for the exchange and reuse of biological models ”. In: *Molecular Systems Biology* 16.8 (2020), pp. 1–21. ISSN: 1744-4292. DOI: 10.15252/msb.20199110.

[451] Kiri Choi et al. “Tellurium: An extensible python-based modeling environment for systems and synthetic biology”. In: *BioSystems* 171.March (2018), pp. 74–79. ISSN: 18728324. DOI: 10.1016/j.biosystems.2018.07.006. URL: https://doi.org/10.1016/j.biosystems.2018.07.006.

[452] Dagmar Waltemath et al. “Reproducible computational biology experiments with SED-ML - The Simulation Experiment Description Markup Language”. In: *BMC Systems Biology* 5 (2011). ISSN: 17520509. DOI: 10.1186/1752-0509-5-198.

[453] Frank T. Bergmann et al. “COMBINE archive and OMEX format: One file to share all information to reproduce a modeling project”. In: *BMC Bioinformatics* 15.1 (2014), pp. 1–9. ISSN: 14712105. DOI: 10.1186/s12859-014-0369-z.

[454] Frank T. Bergmann et al. “COPASI and its applications in biotechnology”. In: *Journal of Biotechnology* 261.February (2017), pp. 215–220. ISSN: 18734863. DOI: 10.1016/j.jbiotec.2017.06.1200. URL: http://dx.doi.org/10.1016/j.jbiotec.2017.06.1200.

[455] Jennifer Lippincott-schwartz, Nihal Altan-bonnet, and George H Patterson. “Photobleaching techniques”. In: 741.September (2003), pp. 735–741. URL: www.nature.com/focus/cellbioimaging.

[456] Faming Jin, Johannes Leitich, and Clemens von Sonntag. “Photolysis ($\lambda = 254$ nm) of phenylalanine in aqueous solution”. In: *Journal of Photochemistry and Photobiology, A: Chemistry* 85.1-2 (1995), pp. 101–109. ISSN: 10106030. DOI: 10.1016/1010-6030(94)03895-2.

[457] Y. Itoh et al. "Photodynamic therapy of acne vulgaris with topical δ-aminolaevulinic acid and incoherent light in Japanese patients". In: *British Journal of Dermatology* 144.3 (2001), pp. 575–579. ISSN: 00070963. DOI: 10.1046/j.1365-2133.2001.04086.x.

[458] Christopher S. Foote. "Photosensitized Oxygenations and the Role of Singlet Oxygen". In: *Accounts of Chemical Research* 1.4 (1968), pp. 104–110. ISSN: 15204898. DOI: 10.1021/ar50004a002.

[459] Glen A. Russell. "Deuterium-isotope Effects in the Autoxidation of Aralkyl Hydrocarbons. Mechanism of the Interaction of Peroxy Radicals". In: *Journal of the American Chemical Society* 79.14 (1957), pp. 3871–3877. ISSN: 15205126. DOI: 10.1021/ja01571a068.

[460] J. A. Howard and K. U. Ingold. "The Self-Reaction of sec-Butylperoxy Radicals. Confirmation of the Russell Mechanism". In: *Journal of the American Chemical Society* 90.4 (1968), pp. 1056–1058. ISSN: 15205126. DOI: 10.1021/ja01006a037.

[461] Ethan Gross, Benjamin Ehrenberg, and Fred M. Johnson. "Singlet Oxygen Generation By Porphyrins and the kinetics of 9,10-dimethylanthracene photosensitization in liposomes". In: *Photochemistry and Photobiology* 57.5 (1993), pp. 808–813.

[462] Owen Jr. Robert W. "The effect of photocarrier generating light on light scattering in the Sea". In: *Journal of the Oceanographical Society of Japan* 29 (1973), pp. 171–184. ISSN: 15635112. DOI: 10.1080/00150198708014494.

[463] Carl J. Lorenzen. "Extinction of light in the ocean by phytoplankton". In: *ICES Journal of Marine Science* 34.2 (1972), pp. 262–267. ISSN: 10959289. DOI: 10.1093/icesjms/34.2.262.

[464] Yeshayahu Nitzan and Helena Ashkenazi. "Photoinactivation of Acinetobacter baumannii and Escherichia coli B by a cationic hydrophilic porphyrin at various light wavelengths". In: *Current Microbiology* 42.6 (2001), pp. 408–414. ISSN: 03438651. DOI: 10.1007/s002840010238.

[465] Katharina Hoenes et al. "Photoinactivation Sensitivity of Staphylococcus carnosus to Visible-light Irradiation as a Function of Wavelength". In: *Photochemistry and Photobiology* 96.1 (2020), pp. 156–169. ISSN: 17511097. DOI: 10.1111/php.13168.

[466] R. Xiong et al. "A mathematical model for bacterial inactivation". In: *International Journal of Food Microbiology* 46.1 (1999), pp. 45–55. ISSN: 01681605. DOI: 10.1016/S0168-1605(98)00172-X.

[467] Rudolf Gesztelyi et al. "The Hill equation and the origin of quantitative pharmacology". In: *Archive for History of Exact Sciences* 66.4 (2012), pp. 427–438. ISSN: 00039519. DOI: 10.1007/s00407-012-0098-5.

[468] Kentaro Inoue et al. "Oscillation dynamics underlie functional switching of NF-κB for B-cell activation". In: *npj Systems Biology and Applications* 2.July (2016). ISSN: 20567189. DOI: 10.1038/npjsba.2016.24. URL: http://dx.doi.org/10.1038/npjsba.2016.24.